

**Fundamental
Magnetohydrodynamic Processes
of Solar Flares:
Formation of Flare-productive Regions
and Evolution of Flare Loops**



Shinsuke Takasao
Department of Astronomy
Kyoto University

A thesis submitted for the degree of
Doctor of Philosophy

March 2016

Acknowledgements

First, I would like to thank my supervisor, Prof. Kazunari Shibata. He is the person who first invited me to the study of the solar and astrophysical plasma physics. The discussion with him greatly improved my understanding of fundamental processes in solar and astrophysical plasmas, and also opened the door to new research areas.

I would like to thank Dr. Hiroaki Isobe. His comments and questions during seminars always got to the points, and greatly helped me improve my studies. I also wish to thank Dr. Ayumi Asai for supporting my observational studies.

I would like to thank Dr. Andrew S. Hiller. When he was in our group, he continuously provided guidance and advice about my researches and English, which helped me establish the foundation of my researches. It would have been difficult to have advanced my researches summarized in this thesis without his support.

I would like to thank my collaborators Dr. Yuhong Fan and Dr. Mark C. M. Cheung. Their fruitful comments on my work often made my vague ideas concrete.

I would like to thank all the members of Kwasan and Hida Observatories and the Department of Astronomy. Special mention goes to Dr. Tetsu Anan, Dr. Kenta Matsuoka, Dr. Jin Matsumoto, Dr. Hiroko Watanabe, Mr. Naoki Nakamura, Mr. Satoshi Takeshige, Mr. Masanori Sano, Mr. Takenori Suda, Mr. Shota Mizuno, Mr. Asuka Ishii and Ms. Mami Obase for their kind encouragement and support. I learned a lot about numerical techniques from Mr. N. Nakamura.

Finally, I would like to thank my family for their kind and continuous support.

Abstract

Solar flares are the most explosive phenomenon in the solar system. The energy source is magnetic energy stored in the corona above sunspot regions. The sunspot regions or active regions are formed as a result of magnetic flux emergence from the interior of the Sun into the solar atmosphere. Solar flares release magnetic energy supplied by flux emergence via magnetic reconnection. In this thesis, flux emergence process and magnetic reconnection process are studied by means of numerical simulations and observations.

It has been known for decades that certain photospheric magnetic configurations of active regions are responsible for the high flare activity. The so-called δ -spot regions are known to be among the most flare-productive active regions. Many attempts have been done for understanding their origins. However, the formation mechanism has been puzzling, which makes understanding of the origin of their high flare activity difficult. In this thesis, we will propose a new formation mechanism on the basis of a three-dimensional magnetohydrodynamics (3D MHD) simulation. The numerical simulation revealed that a highly-twisted magnetic flux bundle can spontaneously result in a complex quadrupole magnetic structure at the photosphere which is favorable for eruption. This study clarifies the impact of the subsurface structure of a flux tube on the flare activity.

Magnetic reconnection drives super-sonic plasma flows, and therefore can produce various kinds of waves and shock waves. Shocks in and above the post-flare loops are believed to be important for both the non-thermal particle acceleration and the evolution of the thermal structure. However, because of the complexity of the flow structure in the flare regions, the shock formation has not been well understood. To advance our understanding, we performed high-resolution 2D MHD simulations of a solar flare. As a result, many new shocks were discovered. Furthermore, it is found that even the very small above-the-loop-top region is full of shocks and waves. This thesis will show the formation process of newly found shocks in detail.

On the basis of the 2D MHD simulation, we developed a 1D new post-flare loop model, which we defined as the pseudo-2D MHD model. This model enables us to study the evolution of the post-flare loops in a wide parameter space without expensive computational cost or neglecting important physics associated with magnetic reconnection.

Observations have revealed the oscillatory nature of solar flares. Quasi-periodic pulsations seen in the lightcurves in a wide wavelength range is a common feature. Recent imaging observations also found various kinds of waves generated by flares, implying that these waves are related to quasi-periodic pulsations. Since MHD waves can be used as a powerful tool to diagnose the local coronal plasma condition, many studies have tried to understand the oscillatory features in and around the post-flare loops. However, in spite of many attempts, we have less knowledge about the excitation of waves. This thesis will provide a detailed picture of the excitation of waves by the reconnection outflow. As a result of 2D MHD simulations of a flare, we discovered the local oscillation of the flare loop-top and the generation of coronal waves from such oscillating flare loop-top.

Contents

Contents	iv
List of Figures	v
List of Tables	vi
1 General Introduction	1
1.1 What is a Solar Flare	1
1.2 Phenomenological and Theoretical Modeling of Solar Flare	3
1.3 What is an Active Region	12
1.4 Basic Concepts of Active Region Formation	15
1.5 Phenomenological and Theoretical Modeling of Active Region Formation	16
1.6 Outstanding Problems	23
2 Formation of Flare-Productive Active Regions	25
2.1 Introduction	25
2.2 Kink Instability of a Twisted Flux Tube Confined in Unmagnetized Plasma	27
2.3 Numerical Setup	29
2.3.1 Basic Equations	29
2.3.2 Initial and Boundary Conditions	30
2.4 Numerical Results	33
2.4.1 Evolution of Flux Tube in the Solar Interior	33
2.4.2 Formation of Complex Quadrupole Structure at Photospheric Level	37
2.4.3 Evolution of Coronal Magnetic Field	39
2.4.4 Magnetic and Flow Structures in and near Middle Pair	47
2.5 Discussion	53

3	MHD Shocks in and above Flare Loops: Two-dimensional Simulation and a Simplified Model	58
3.1	Introduction	58
3.2	2D MHD Model of a Solar Flare	60
3.2.1	Assumptions and Basic Equations	60
3.2.2	Initial and Boundary Conditions	61
3.3	Numerical Results of 2D MHD Model	63
3.3.1	Overview of Evolution	63
3.3.2	Dynamics and Energetics along a Specific Field Line	72
3.4	Pseudo-2D MHD Model of a Flare Loop	75
3.4.1	Physical Processes Considered	75
3.4.2	Assumptions and Basic Equations	77
3.5	Numerical Results of Pseudo-2D MHD Model	82
3.5.1	Dynamics and Energetics	82
3.5.2	Dependence on Parameters	86
3.6	Summary and Discussion	87
4	Above-the-loop-top Oscillation and Quasi-periodic Coronal Wave Generation in Solar Flares	91
4.1	Background	91
4.2	Numerical Model	92
4.3	Numerical Results	93
4.3.1	Evolution of Flare Loops and Emission of Coronal Waves	93
4.3.2	Multiple Termination Shocks and New Picture of Flare Loops	95
4.3.3	Above-the-loop-top Oscillation	97
4.3.4	Dependence on Magnetic Field Strength	103
4.4	Discussion	105
5	Concluding Remarks	108
A	Some notes of Solar Flare Simulations	111
A.1	Spitzer Conductivity	111
A.2	Numerical Method of Heat Conduction in 2D MHD Model	114
A.3	Analytical Approach to the Riemann Problem: Possible Solutions	115
A.4	Scaling of Fast-mode Mach Number of Reconnection Outflow Jet	120
	References	123

List of Figures

1.1	A schematic representation of the light curves of different electromagnetic waves from a solar flare [Kane, 1974].	2
1.2	Schematic diagram of the temporal evolution of an eruptive flare by Hirayama [1974].	5
1.3	Development of the models for flare loops. (a) Comparison of Kopp and Pneuman [1976] model, Cargill and Priest [1982] model, Forbes and Priest [1983] model, and Forbes and Malherbe [1986] model (from Priest and Forbes [2002]). (b) Result of a direct 2D MHD model that includes the effects of reconnection, heat conduction, and evaporation, and a schematic illustration of the simulation results [Yokoyama and Shibata, 1998].	7
1.4	Temporal evolution of the LDE flare with a cusp-shaped loop structure (see also Tsuneta [1996]; Tsuneta et al. [1992]).	8
1.5	Hard X-ray (top row) and soft X-ray (bottom row) images of the 13 January 1992 flare that occurred near the west solar limb (from Masuda et al. [1994]).	9
1.6	Close-up images of the reconnection site in six different wavelengths (171, 193, 211, 335, 94, and 131 Å) of AIA at the time when the current sheet, the plasma blob, and the hot flare loops are observed. White solid lines indicate the solar limb (from Takasao et al. [2012]).	11
1.7	Light curves of the flare on 1998 May 8 at 01:57 UT recorded with Nobeyama Radioheliograph in 17 GHz (thick curve) and with Yohkoh/HXT in the L (13-23 keV, thin solid curve) and M1 (23-33 keV, dotted curve) channels (from Nakariakov and Melnikov [2009]. The original data is from Inglis et al. [2008]).	12

1.8	A full disk magnetogram image obtained by SOHO/MDI (Left) and a full disk soft X-ray image by Yohkoh/SXT (Right) on May 21, 2000. The magnetogram shows the line-of-sight magnetic flux density on the photosphere. White and black colors indicate a positive and negative polarities, respectively.	13
1.9	<i>Yohkoh</i> images of the solar X-ray corona on 1992 March 1992 at 19:51UT, 21:36UT, and 1:05UT (left to right) on 1992 March 28. The arrow in the leftmost image points out the reverse-S feature (“sigmoid”) that the signals the onset of a flare event. In the middle, the arrow shows the beginnings of the transformation into a loop arcade. In the final image, the loop arcade is fully developed and very bright. The two black curves drawn on the image show the shape of the late-phase loops. From Rust and Kumar [1996]	14
1.10	Schematic diagram of the different modes of the magnetic buoyancy instabilities of a horizontal flux sheet [Matsumoto et al., 1993].	17
1.11	A model of flux emergence by Zwaan [1985]	18
1.12	2D MHD simulation of the Parker instability of a flux sheet embedded in the photosphere [Shibata et al., 1989a].	18
1.13	An example of the emergence of twisted flux tubes (Left) and a schematic illustration of the active region (Right) (from Ishii et al. [1998]).	19
1.14	The Mount Wilson classification (top row: continuum images, bottom row: magnetogram). α -type: A sunspot group dominated by a single unipolar spot. β -type: A sunspot group that has a pair of sunspots of opposite magnetic polarity, but with a simple and distinct spatial division between the polarities. δ -type: a sunspot group in which sunspot umbrae of opposite magnetic polarities are pressed together in a common penumbra. The images are taken by HMI/SDO.	20
1.15	Statistical investigations of the relation between the magnetic structure of active regions and flare activity. (a) Peak flare intensities in $W m^{-2}$ for each sunspot group as a function of peak area in disk fraction, with each magnetic class plotted separately (from Sammis et al. [2000]). (b) Flare index versus maximum umbral area on a logarithmic scale (from Takizawa and Kitai [2015]).	22

2.1	Initial setup of the simulation. (a) Schematic diagram of the model atmosphere and initial flux tube. (b) Vertical distributions of the density ρ (solid), pressure p (dotted), temperature T (dashed), and magnetic field strength B (dashed dotted line) in the initial condition. See Table 2.1 for the normalization units.	32
2.2	The rise of the flux tube in the solar interior. The yellow lines denote the selected magnetic field lines, and the blue surfaces indicate the isosurface where $B = 2B_0$	35
2.3	Temporal evolution of the ratio of the magnetic field strength B to the square root of the density $\rho^{1/2}$. The ratio is measured along the z -axis crossing the point $(x, y) = (0, 0)$. The dashed line denotes the initial profile. The solid lines with different colors indicate the profiles at different times. The time interval between successive plots is 30τ . . .	36
2.4	Temporal evolution of the photospheric (Left) and chromospheric (Bottom) line-of-sight magnetic fields B_z . The heights of the photospheric and chromospheric planes are $80H_{p0}$ and $96H_{p0}$, respectively. $H_{p0}=170 \text{ km s}^{-1}$, and $\tau=25 \text{ s}$	38
2.5	Temporal evolution of the direction and distance from the centroid of the positive polarity region to the centroid of the negative polarity region. The centroids are defined by Equation 2.16. $H_{p0}=170 \text{ km s}^{-1}$, and $\tau=25 \text{ s}$. . .	39
2.6	Time evolution of the photospheric ($z = 80H_{p0}$) line-of-sight magnetic field B_z (Left) and the vertical velocity component v_z measured at the center $(x, y) = (0, 0)$ (Right). In the right panels, the horizontal dashed lines denote the $v_z = 0$, and the vertical dotted lines indicate the photospheric height. Note that the sinking motion is seen when the middle pair is formed.	40
2.7	Formation of the middle pair. (a) Temporal evolution of the 3D magnetic field (solid lines) and magnetogram B_z . The last two panels shows the magnetic structure below the photosphere and the dip of emerged magnetic fields at the time $t = 340\tau$. (b) Profiles of the vertical forces measured at the center $(x, y) = (0, 0)$. The total force (solid), pressure gradient force (dotted), gravitational force (dashed), and Lorentz force (dashed-dotted) are shown. Note that the sign of the total vertical force is negative near the photosphere, meaning that the downward gravitational force is the most dominant force.	41

2.8	(a-c): Time sequence of the magnetic field distribution on the y - z plane at $x = 0$. The arrows denote the direction of the magnetic field projected onto this plane (note that the size of the arrows does not represent the magnetic field strength). (d): The density distribution with velocity vectors on this plane. A high-density region is formed between the two arcades. (e): A schematic diagram to describe the submergence process. Plasma is accumulated in the middle of this region, and the heavy portion of the emerged fields submerges.	43
2.9	3D Magnetic structure and photospheric and chromospheric line-of-sight magnetic fields B_z at the time 392τ . The yellow and blue field lines denote field lines passing by the current sheet between the two arcades. The white field lines denote field lines enveloping the two arcades. The purple and white field lines denote field lines created by reconnection between the blue and yellow magnetic loops. (a-c): Bird's eye view. (d): Top view. (e): A schematic diagram of the merging field lines. (f): A schematic diagram of the magnetic field structure shown in the panel (d). Note that the purple reconnected field lines are almost parallel to the neutral line at the middle.	44
2.10	(a) Snapshots of the z -component of the vorticity ω_z at the photospheric level. White and black contours denote positive ($3B_0, 4B_0$) and negative ($-4B_0, -3B_0$) B_z , respectively. Note that the main polarities show counterclockwise motion. (b) Temporal evolution of the averaged ω_z over the area where $ B_z $ is above 75% of the peak $ B_z $	45
2.11	Temporal evolution of the vector magnetogram of the photosphere and middle chromosphere. Arrows show the horizontal magnetic field vectors. The horizontal magnetic field becomes more parallel to the polarity inversion line (PIL) at those heights as time progresses. Note that the horizontal magnetic field strength is small on the PIL. See also Figure 2.10 as for magnetic shear development).	46
2.12	Magnetogram (B_z) with horizontal velocity vectors (Top) and with Lorentz force vectors (Bottom) at time $t = 362\tau$. In the bottom panel, red and blue arrows show the Lorentz force in positive and negative polarities, respectively. The velocity and Lorentz force are normalized by C_{s0} and B_0^2/H_{p0} , respectively.	48

2.13	Profiles of the total pressure p_{tot} (solid), gas pressure p (dotted), magnetic pressure p_m (dashed), and dynamic pressure p_v (dashed-dotted) across the polarity inversion line of the middle pair. The profiles are measured along the slit shown in the B_z maps. The velocity component parallel to the slit is used to calculate p_v	49
2.14	Development of the horizontal magnetic field just near the polarity inversion line of the middle pair. (a) Snapshots of 3D magnetic field lines with magnetogram. (b) Enlarged images of the magnetogram B_z and the ratio $ B_h/B_z $ of the middle pair. The arrows indicate the horizontal magnetic field vector $\mathbf{B}_h = (B_x, B_y)$	50
2.15	The Lorentz force drives flows along the polarity inversion line (PIL) of the middle pair. The color indicates $f_{L,\text{PIL}} = (\mathbf{J} \times \mathbf{B}) \cdot \hat{\mathbf{e}}$ (Left) and $f_{P,\text{PIL}} = (-\nabla p) \cdot \hat{\mathbf{e}}$ (Right), where $\hat{\mathbf{e}} = (-1/\sqrt{2}, 1/\sqrt{2})$ is a unit vector almost parallel to the PIL. Note that positive (negative) $f_{L,\text{PIL}}$ accelerates plasma in the upper-left (lower-right) direction. The same is true for $f_{P,\text{PIL}}$. The arrows denote the horizontal velocity, and the solid lines indicate the PIL ($B_z = 0$). The velocity is normalized by C_{s0}	51
2.16	Comparison of the δ -spot region NOAA 11429 and our simulation. The left and middle panels show the continuum and magnetogram images. The middle polarity pair between the largest opposite polarities is indicated by the arrow. The right panels show the snapshots of the magnetogram from our simulation at the time $t = 310\tau$ and 335τ . Note that the sign of B_z of the magnetogram from the simulation is reversed just for better comparison. This does not change its twist handedness.	52
2.17	Schematic diagram of the formation of a quadrupole photospheric structure. Top: the horizontal expansion of the kinked flux tube before the emergence. See also Figure 2.2 and 2.7. Bottom: 2D cut view of the expanding two magnetic arcades. The two magnetic concentrations below the photosphere correspond to the two parent flux tubes. The plus and minus signs denote the positive and negative polarities at the photosphere, respectively. See also Figure 2.8 and 2.9.	54

3.1	Schematic diagram of the initial and boundary conditions of the 2D MHD simulation. The solid arrows denote the magnetic field. The circled region indicate the region where the localized resistivity is applied. The grey region at the bottom is the chromosphere. The calculated domain is the region where $x > 0$	62
3.2	Time evolution of the temperature (Top) and density (Bottom) of the 2D MHD model. The solid lines denote the magnetic field.	64
3.3	One-dimensional plots parallel to the x -axis across $y = 10$ at $t = 13$ (across the reconnection outflow region). The density, temperature, pressure, J_z , v_x and v_y are displayed. The vertical dashed-lines indicate the slow shocks attached to the reconnection outflow.	65
3.4	Gas pressure (Left) and $\nabla \cdot \mathbf{v}/C_s$ (Right) maps of the loop top. Top: Snapshot when the termination shock consists of two oblique fast-mode shocks. Bottom: Snapshot when the termination shock consists of two oblique shocks and a horizontal shock. Note that most of the regions where $\nabla \cdot \mathbf{v}/C_s$ takes large negative values are slow or fast shocks.	67
3.5	Formation of the high-density regions called humps. Left: the density in logarithmic scale. Right: $\nabla \cdot \mathbf{v}/C_s$. The solid lines denote magnetic field lines. The velocity vectors projected to the x-y plane are also displayed in the density maps (only the vectors with $\sqrt{v_x^2 + v_y^2} > 0.3$ are shown). Note that most of the regions where $\nabla \cdot \mathbf{v}/C_s$ takes large negative values are slow or fast shocks.	68
3.6	Formation of the high-density loop-top. Left: the density in logarithmic scale. Right: $\nabla \cdot \mathbf{v}/C_s$. The solid lines denote magnetic field lines. Only one of the pair of the slow shocks heading to the apex is indicated by the arrows. Note that most of the regions where $\nabla \cdot \mathbf{v}/C_s$ takes large negative values are slow or fast shocks.	69
3.7	Snapshots of the density, temperature, entropy ($\log(p/\rho^\gamma)$), and plasma β at $t = 20$. The arrows indicate slow shocks in the flare loops (See also Figures 3.5 and 3.6). The solid lines in the first three panels denote the magnetic field. The contour in the plasma β map denotes the level where $\beta = 1$ ($\log_{10} \beta = 0$).	71
3.8	Evolution of a specific reconnected field line with the density map. The tracked field line is indicated by the thick black line. The foot-point of the field line is located at $(x, y) = (1.2, 0)$. The circle is the origin of the distance.	72

3.9	Time-distance diagrams of the density (Top Left), temperature (Top Right), v_{\parallel} (Bottom left), and $\nabla \cdot \mathbf{v}/C_s$ (Bottom Right). The physical quantities are measured along the field line which is originated from $(x, y) = (1.2, 0)$. The distance is measured along the field line, and its origin is the apex ($x = 0$). The data of the domain of $x < 0$ is also shown just for visual inspection. The sign of v_{\parallel} is defined as positive and negative when a plasma flow travels to the apex and foot-points, respectively. This field line does not pass through the termination shock. Note that the regions where $\nabla \cdot \mathbf{v}/C_s$ takes large negative values are slow or fast shocks.	74
3.10	Time evolution of the total (thick solid), magnetic (dashed), internal (dash-dot), and kinetic (thin solid) energies along the specified field lines in the 2D MHD model. The vertical dashed lines denote the times when each field line reconnects.	76
3.11	Schematic diagram of the reconnected magnetic field in 2D (Left) and the magnetic field mimicking the reconnected field in the 1D-approximation model (pseudo-2D MHD model, Right). The bottom panels show the difference in the reconnected magnetic field configurations between two models.	77
3.12	Schematic diagram of the set up of our pseudo-2D flare model (Right) based on a 2D picture (Left). h_{rx} and h_{TR} are the height of the reconnection point and height of the transition region, respectively. $\tan^{-1}(x_{max}/h_{rx}) = \theta$ is the reconnection angle. The grey shaded regions indicate the dense cool material representing the chromosphere. Note that in the pseudo-2D MHD model, all the physical quantities are function of x	78
3.13	The magnetic configurations of a specific field line in the initial state ($y_{line}(x, t = 0)$), at $t = t$ ($y_{line}(x, t = t)$), and in the final state ($y_{line,fin}(x)$), respectively. $\Delta d(x, t) = y_{line}(x, t) - y_{line,fin}(x)$ is also described.	81
3.14	Downward moving magnetic field line in the pseudo-2D MHD model. The dashed line denotes the assumed final configuration $y_{line,fin}$	83
3.15	One-dimensional plots parallel to the x -axis at $t = 0.7$ (across the reconnection outflow region). The density, temperature, pressure, J_z , v_x and v_y are displayed.	84

3.16	Comparison between the pseudo-2D MHD model (Left) and the 2D MHD model (Right). Time-distance diagrams of the density and $\nabla \cdot \mathbf{v}/C_s$ are shown. The physical quantities of the 2D MHD model are measured along the field line which is originated from $(x, y) = (1.2, 0)$. The distance is measured along the field line, and its origin is the apex ($x = 0$). The data of the domain of $x < 0$ is also shown just for visual inspection. Note that most of the regions where $\nabla \cdot \mathbf{v}/C_s$ takes large negative values are slow or fast shocks.	85
3.17	Time evolution of the total (thick solid), magnetic (dashed), internal (dash-dot), and kinetic (thin solid) energies along a field line in the pseudo-2D MHD model.	86
3.18	Temperature as a function of the initial β (Left), the height of the reconnection point h_{rx} (Middle), and the heat conductivity κ_0 (Right), respectively. The data points are taken from the pseudo-2D MHD simulations. T_{jet} denotes the temperature in the reconnection outflow. T^* denotes the maximum temperature after the pair of the two slow shocks generated by the chromospheric evaporation flows collides at the apex. The dashed lines show the analytical scaling laws.	87
4.1	Quasi-periodic propagating fast mode magnetoacoustic waves (QPF) in our simulation ($\beta = 0.08$). Top: Density map at time=349.2 sec from the start. The solid lines denote magnetic field lines. An enlarged image of the above-the-loop-top region is also displayed. Middle: The normalized running difference of the density $\Delta\rho/\rho$, defined as $(\rho(t) - \rho(t - \Delta t))/\rho(t)$, where $\Delta t = 1.8$ sec. Bottom: Observational example of QPF accompanied with a GOES C2.8 flare which occurred on 30 May 2011.	94
4.2	Snapshots of the above-the-loop-top region. Top row: Density distribution. Oblique and horizontal fast shocks are indicated. Bottom row: Total pressure (gas pressure plus magnetic pressure) distribution. Note that the total pressure in the reconnection outflow is smaller than that of the above-the-loop-top region. Solid lines denote magnetic field lines.	96

4.3 Passage of a specific field line through the multiple termination shocks. Left panels: Snapshots of the temperature and density distributions of the above-the-loop-top region. Black field line in the temperature map and white field line in the density map denote the same field line. Right panels: Time-sequenced images obtained along the tracked field line (density). The white solid lines denote the timings of the snapshots in the left panels. The shocks which the field line crosses in the region $x > 0$ are denoted by the yellow solid lines. The segments between a slow shock and a fast shock are indicated by arrows in the density map. 98

4.4 Comparison of a previous picture of flare loops based on a standard flare model and Yokoyama and Shibata [1998] model (Left) with a new picture based on our simulations (Right). Black solid lines denote magnetic field lines. Pale orange regions denote evaporated plasma. Orange regions indicate dense regions. Pale yellow regions denote regions inside the conduction fronts. Blue solid lines indicate shocks. Flows are denoted by arrows. A detailed description of the new picture is given in Takasao et al. [2015]. Enlarged images of the above-the-loop-top regions are displayed at the bottom. 99

4.5 Above-the-loop-top oscillation (the initial β is 0.08). Left: Snapshots of the distribution of $\log_{10} \beta$ of the above-the-loop-top region. Right: Time-sequenced images of $\log_{10} \beta$ and $\Delta p_{tot}/p_{tot}$ obtained along the slit shown in the left panels. The slit used is positioned so that its y -coordinates is 68 km below the interaction point of the two oblique shocks. The horizontal lines in the time-sequenced images denote the timings of the snapshots in the left panels. 100

4.6 (a) Backflow of the reconnection outflow in the above-the-loop-top region. (b) Schematic illustration of the above-the-loop-top oscillation. . . 102

4.7 Relation between the above-the-loop-top oscillation and coronal waves (a) Temporal evolution of the ratio of the pressures ahead (p_a) and behind (p_b) a topmost oblique shock (solid) and the maximum of the horizontal component of the backflow (dashed). (b) Wavelet analysis of the coronal fast waves. The running difference of the density at the position $(x, y) = (1.5 \times 10^4 \text{ km}, 3.9 \times 10^4 \text{ km})$ is used. 103

4.8 Plasma β dependence of the oscillatory property. (a) Plasma β dependence of the period (Left) and the maximum of the horizontal component of the backflow (Right). The period is estimated from the time interval between the initial and second peaks seen in the pressure ratio p_b/p_a . In the left panel, the dashed line indicates the slope $\propto \beta$. In the right panel, the dashed line denotes $0.45V_{A0}$. (b) Comparison of the cases with $\beta = 0.06$ (Left) and $\beta = 0.2$ (Right). The vertical sizes of the above-the-loop-top region are compared. (c) Schematic illustration of the plasma flow in the termination region. w denotes the vertical size of the magnetic tuning fork. 104

A.1 The grid points used to calculate the heat flux for the grid (i, j) in [Yokoyama and Shibata \[2001\]](#) (Left) and our method (Right). The red and blue grids have the physical quantities at the time $t = t^{n+1}$ and those at $t = t^*$, respectively. 116

A.2 Three possible solutions of the Riemann problem. Left column: Case without a guide field, where B_y is switched off by the slow shock (SS). Middle column: Case without a guide field, where B_y is switched off by the fast mode rarefaction wave (FRW). Right column: Case with a guide field, where the magnetic field is rotated by the rotational discontinuity (RD) and the magnetic energy is released at the slow shock (SS). First row: $x-t$ diagrams that show the Riemann fans. Second row: $|B_z| - |B_y|$ diagrams that show the transitions through the regions in the Riemann fans (the paths are indicated by the dashed lines in the first row). The third and fourth rows: $x-y$ diagrams that show the magnetic field configurations on the plane. Only for the case with a guide field, $x-z$ diagram is also depicted. The grey regions indicate the high-entropy regions due to the shock dissipation. 118

A.3 A phase diagram of the possible solutions of the symmetric Riemann problem in the situation without a guide-field. θ is the reconnection angle and β is the plasma beta. "Switch-off slow shock" regime and "pure hydro shock" regime corresponds to the left and middle panels in [Figure A.2](#), respectively. 119

A.4 Top: The normalized reconnection rate in the θ - β plane. Bottom: The normalized reconnection rate for $\beta = 0.1$ as a function of θ 120

A.5 Dependence of the fast-mode Mach number of the reconnection outflow (M_{FM}) on the plasma β . The data points indicated by diamonds and triangles are from [Seaton and Forbes \[2009\]](#). Diamonds and triangles denote the data points for the normalized conduction coefficient $\lambda^* = 0.03$ and 0.003 , respectively (see the text for the definition of λ^*). The dashed line indicates the slope $\propto \beta^{-2/7}$ 122

List of Tables

2.1	Normalization units for the flux emergence simulation	30
3.1	Normalization units for solar flare simulations	61

Chapter 1

General Introduction

1.1 What is a Solar Flare

Solar flares are the most energetic phenomenon in the solar system, where 10^{29} to 10^{32} ergs of magnetic energy in the corona is rapidly released during a short period of 10^3 – 10^4 s. The spatial size of a flare ranges 10^4 – 10^5 km, and it affects both the duration and the amount of the released energy. The released energy takes various forms such as radiative energy, kinetic bulk energy, thermal energy, and nonthermal particle energy. For this reason, the released magnetic energy is the source of diverse explosive phenomena. Solar flares are often associated with the ejection of a large amount of plasma (coronal mass ejection; CME) to the interplanetary space (up to 10^{16} g), and the acceleration of a huge number of nonthermal particles. Therefore, they can cause severe disturbances to the solar system, and even to our modern society.

Solar flares can be recognized in a wide range of electromagnetic waves. Figure 1.1 displays a schematic representation of the light curves of different electromagnetic waves from a solar flare [Kane, 1974] that ranges from gamma rays to radio waves. From this, it is reasonable to define a solar flare as a transient phenomenon which shows a sudden increase in multi-electromagnetic waves. The emissions come from different atmospheric layers, particularly the chromosphere and corona, and from different parts of a flare. Even the photosphere may respond to a flare if an extremely huge flare occurs. The maximum temperature reaches $\sim 3 \times 10^7$ K, whereas their feet are located in the chromosphere with the temperature of 10^4 K. The density contrast between the photosphere and corona is $\sim 10^8$. Hence, we may say that a solar flare is a phenomenon in which different atmospheric layers are dynamically coupled as a result of the release of magnetic energy in the corona. Because of this interesting but complex nature, solar

flares have been extensively studied over decades.

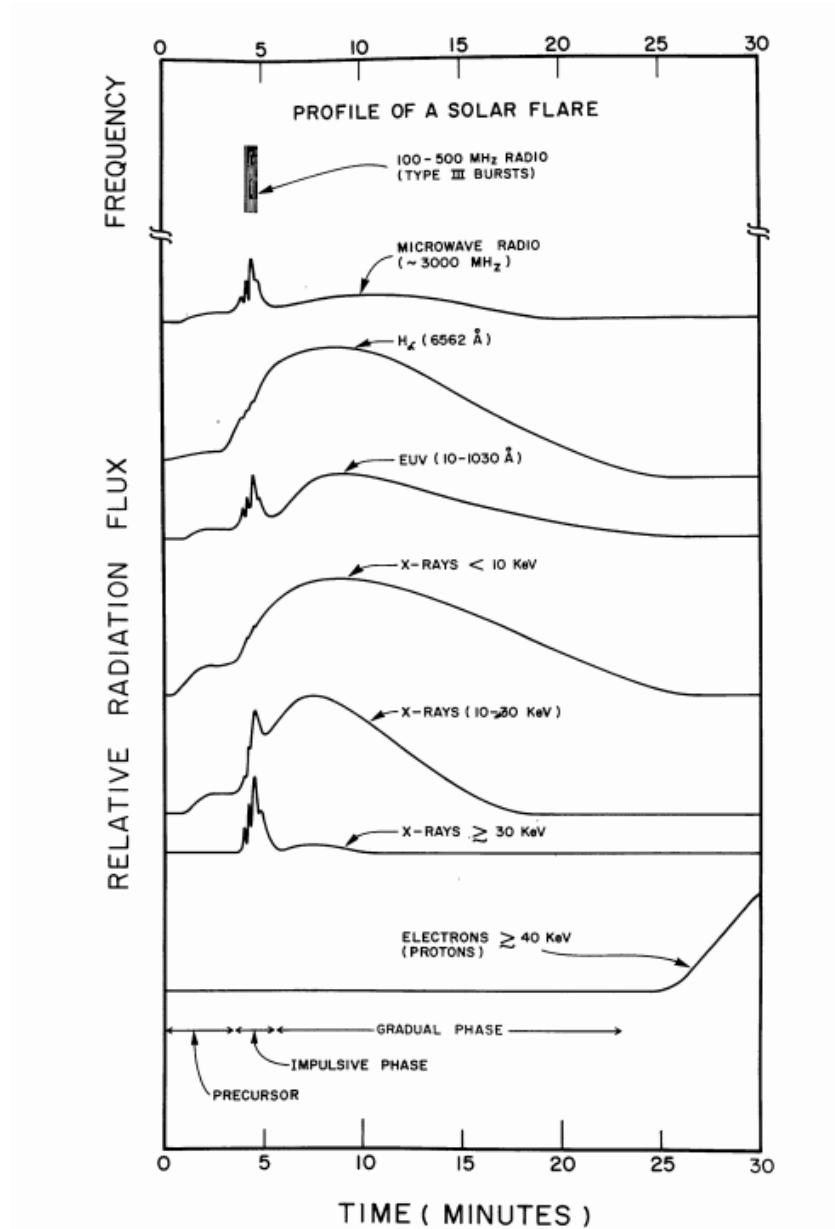


Figure 1.1: A schematic representation of the light curves of different electromagnetic waves from a solar flare [Kane, 1974].

Solar flares were discovered in the white light emission in the 19th century [Car-
rington, 1859; Hodgson, 1859]. After decades, a photospheric magnetic field in the

solar atmosphere was discovered by Hale [1908] through sunspot observations. The ground based visible observations mostly with H α filters revealed dynamic chromospheric plasma motions and beautiful bright two ribbons during flares [Svestka, 1976]. It was the *Skylab* mission (1973–1974) that for the first time performed detailed studies of the coronal structure and dynamics using soft X-ray. The *Skylab* mission revealed that the locations of the bright regions in soft X-ray, including flaring regions, correspond to intense magnetic field regions, which strongly supports the idea that the main energy source of the explosive events in the solar atmosphere is magnetic energy. The total magnetic energy stored in a sunspot with the size L and the magnetic field strength B is estimated as

$$E_{\text{mag}} \simeq \frac{B^2}{8\pi} L^3 \simeq 10^{33} \left(\frac{B}{10^3 \text{ G}} \right) \left(\frac{L}{3 \times 10^9 \text{ cm}} \right)^3 \text{ ergs.} \quad (1.1)$$

Of course only a small fraction of this energy is available for flares because a large portion of this is in the form of the potential field energy. Nevertheless, sunspots have a huge amount of magnetic energy that is sufficient to produce flares.

1.2 Phenomenological and Theoretical Modeling of Solar Flare

It was well established in 1940's from observations that flares are closely associated with sunspots. It was also noticed that complex active sunspot regions tend to produce flares more frequently than simple bipolar regions. Considering the facts, people began to develop phenomenological and theoretical models to account for the association. Giovanelli [1946] focused on the electric current induced by the magnetic field of a growing sunspot. To explain the sudden brightenings of the chromosphere (historically called the chromospheric flares), he proposed a scenario in which electrons accelerated by induction electric fields near neutral points excite the optical emissions of chromospheric atoms through collision. Hoyle [1949] presented a similar idea, but he is the first person who consider magnetic reconnection, a physical process in which a magnetic field in a highly conducting plasma changes its connectivity due to finite resistivity. However, Cowling [1953] heavily criticized their ideas mainly by pointing out the difficulty in explaining the timescale of flares. That is, if we assume that the

magnetic energy is released solely by magnetic diffusion, the timescale will be given as

$$t_{\text{diff}} \simeq \frac{L^2}{\eta} \simeq 10^{14} \left(\frac{L}{10^9 \text{ cm}} \right)^2 \left(\frac{T}{10^6 \text{ K}} \right)^{3/2} \text{ s}, \quad (1.2)$$

which is much larger than a typical timescale of flares ($\sim 10^{3-4}$ s), where T is a typical temperature of the corona and we assume the Spitzer resistivity [Spitzer, 1962]. In order to explain a reasonable flare timescale, the thickness of the electric current layer (current sheet) should be less than a kilometer, which is much smaller than a typical system size. For this reason, he concluded that their ideas are unpromising. Later, however, Hoyle's student Dungey [1958] showed that the Lorentz force tends to form a thin, extended current sheet, and disputed Hoyle's argument.

A big progress of the magnetic reconnection theory was made by Sweet [1958] and Parker [1957] who considered the plasma flows around the current sheet, and their model is now known as the Sweet-Parker model. The model considers magnetic reconnection under the assumption that resistivity is almost uniform spatially. The model predicts that the reconnection timescale is $t_{\text{recon}} = L/v_{in} = S^{1/2}t_A$ and the thickness of the current sheet is $w = S^{-1/2}L$, where L is the system size (typically, $L \sim 10^9$ cm), v_{in} is the reconnection inflow speed, t_A is the Alfvén time scale ($t_A \sim L/V_A \sim 10$ s), and S is the Lundquist number ($S = LV_A/\eta \sim 10^{14}$ for a typical coronal situation). Although the Sweet-Parker reconnection is a possible solution in some situations, the energy release timescale ($t_{\text{recon}} \sim 10^8$ s) is still larger roughly by four or five order of magnitudes than that of actual solar flares ($t_{\text{flare}} \sim 10^{3-4}$ s) if we use a macroscopic length. Also, the thickness of the Sweet-Parker current sheet should become extremely thin (~ 100 cm for the Spitzer resistivity), but the apparent thickness of the current sheet is $\sim 10^9-10^{10}$ cm and much larger than this [Lin et al., 2005] (note that the actual current sheet width still remains unclear). Thus, the Sweet-Parker model cannot explain the rapid energy release and observational features of solar flares.

Petschek [1964] found that the reconnection speed or rate can be large enough to account for the flare timescale if the diffusion region is spatially localized in the current sheet due to some reason. In this case, magnetic energy is released mainly at the slow shocks attached to the diffusion regions, not in the diffusion region. For this reason, the energy release timescale is no longer controlled by magnetic diffusion, and can be close to the Alfvén timescale. Although the Petschek model has fundamental problems, magnetic reconnection has been considered as one of the promising mechanisms for driving flares since he proposed this model.

Phenomenological models have been developed in parallel with the development of

the reconnection theory. A standard model of “eruptive” flares is based on the work by Carmichael [1964], Sturrock [1966], Hirayama [1974], and Kopp and Pneuman [1976], and therefore it is called CSHKP model. The CSHKP model considers that the central engine of flares is magnetic reconnection. This model gives an insightful picture of flares, and puts a great emphasis on the roles of magnetic reconnection. Figure 1.2 shows a schematic diagram of the temporal evolution of an eruptive flare by Hirayama [1974]. His model clearly describes many observational characteristics seen in $H\alpha$, Extreme UltraViolet, and soft X-ray, and the prominence eruption associated with a flare.

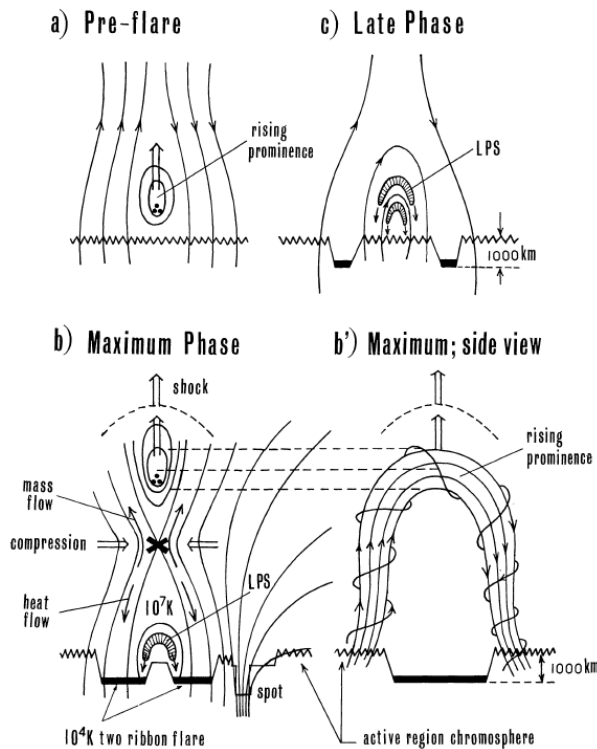


Figure 1.2: Schematic diagram of the temporal evolution of an eruptive flare by Hirayama [1974].

On the basis of the CSHKP model, many attempts have been made for understanding the influences of reconnection on the plasma flow and thermal structures of flares. The development of the models for flare loops are shown in Figure 1.3. Kopp and Pneuman [1976] proposed that a pair of gas-dynamic shocks propagate down the legs of the reconnected loops. Cargill and Priest [1982] considered the heating of the flare loops by the Petschek slow shocks, and they showed that the Petschek slow shocks can heat

the plasma to the temperature of $\sim 3 \times 10^7$ K. On the basis of numerical experiments, [Forbes and Priest \[1983\]](#) pointed out that a fast MHD shock is formed above reconnected loops when the sunward reconnection outflow collides with the loops. Now the fast shock is often called a termination shock. [Forbes \[1986\]](#) examined the formation of the termination shock using two-dimensional (2D) MHD simulations, and found that the downstream region of the shock is more complicated than was previously thought. [Forbes and Malherbe \[1986\]](#) considered the thermal structure of flares by noting the effects of the heat conduction, and split each slow shock into an isothermal slow shock and a standing conduction front. [Yokoyama and Shibata \[1997\]](#) carried out a direct numerical MHD simulation of magnetic reconnection coupled with heat conduction, and confirmed the split of each adiabatic slow shock into an isothermal slow shock and a conduction front. The effects of chromospheric evaporation were included in [Yokoyama and Shibata \[1998\]](#). [Yokoyama and Shibata \[1998\]](#) also derived a scaling law for the flare temperature, and established a new picture of solar flares (see the schematic illustration in [Figure 1.3](#)). A detailed parameter survey was performed by [Yokoyama and Shibata \[2001\]](#).

Solar flare models based on magnetic reconnection are broadly consistent with observations, but the understanding of solar flares was largely qualitative until the end of 1990's. Some attempts to model solar flares with time-dependent 1D hydrodynamics simulations were made by e.g. [Peres et al. \[1987\]](#), but they failed to account for essential aspects of the observations such as the slow decay of the flare emission and the dominant contribution to emission from the stationary component. Therefore, quantitative comparisons between such numerical models and observations had been unsuccessful. The main reason of the failure is that the previous studies treated the flare as a “single” loop and neglected the fact that magnetic field lines are successively reconnected during flares. This idea of successive reconnection was first incorporated by [Hori et al. \[1997, 1998\]](#). They modeled flares as a superposition of many independently-heated “threads”. In their model, the spatially averaged line profiles are generally dominated by the stationary component, which is qualitatively consistent with observations. Detailed quantitative comparisons between such a multithread model and observations were performed by e.g. [Reeves and Warren \[2002\]](#); [Warren \[2006\]](#), and succeeded in accounting for many observational aspects.

We note the fact that many people were skeptic about reconnection models and they proposed anti-reconnection models before the *Yohkoh* era (e.g. [Akasofu \[1984\]](#); [Alfvén and Carlqvist \[1967\]](#)). This is mainly because the investigation of magnetic reconnection just begun and people had less knowledge about it. For example, the

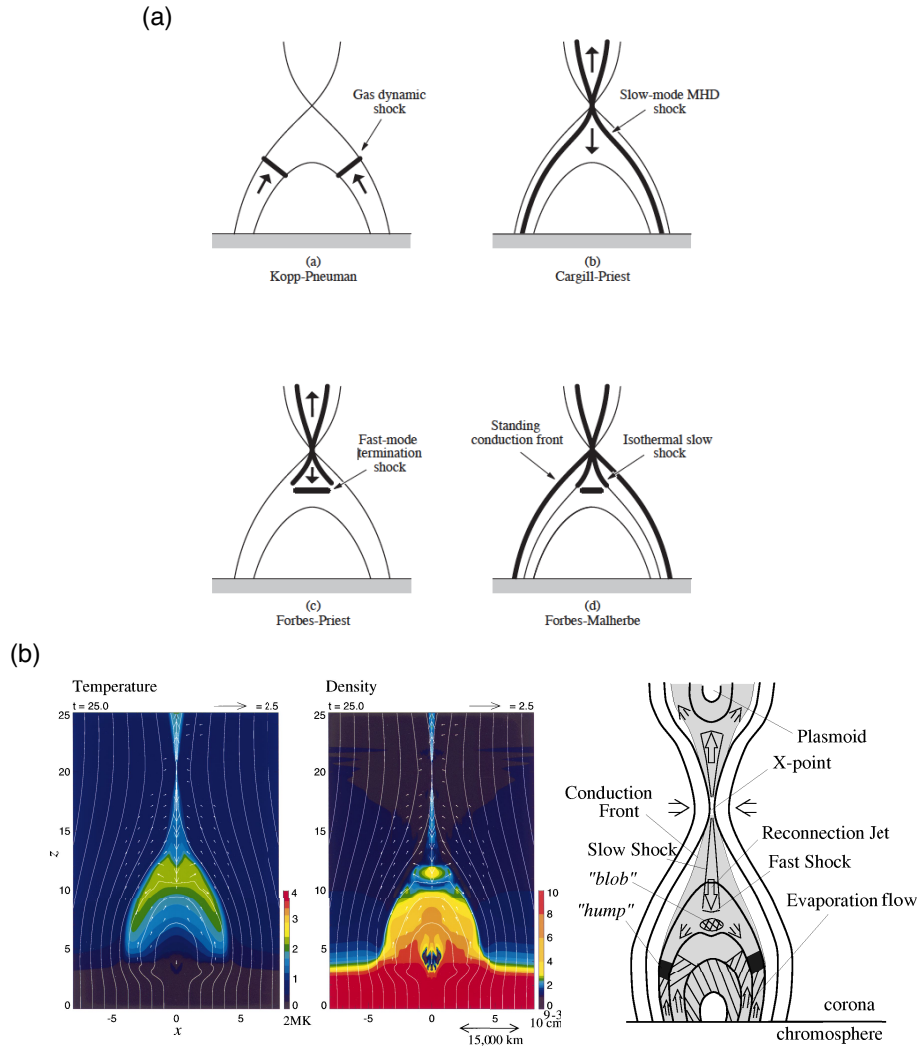


Figure 1.3: Development of the models for flare loops. (a) Comparison of [Kopp and Pneuman \[1976\]](#) model, [Cargill and Priest \[1982\]](#) model, [Forbes and Priest \[1983\]](#) model, and [Forbes and Malherbe \[1986\]](#) model (from [Priest and Forbes \[2002\]](#)). (b) Result of a direct 2D MHD model that includes the effects of reconnection, heat conduction, and evaporation, and a schematic illustration of the simulation results [[Yokoyama and Shibata, 1998](#)].

Petschek model assumes an incredibly small diffusion region (the size may be similar to the ion Larmor radius in the corona, 10^2 cm!), and therefore it is very hard to imagine that such a small region can control a flare with the size of 10^9 cm. The fact that people also lacked clear observational evidence of magnetic reconnection could be also a reason for this. However, reconnection models predict observable characteristics such as a hot cusp-shaped loop structure in the corona (e.g. [Hirayama \[1974\]](#)). Therefore, people looked forward more advanced observations of the corona in which reconnection occurs.

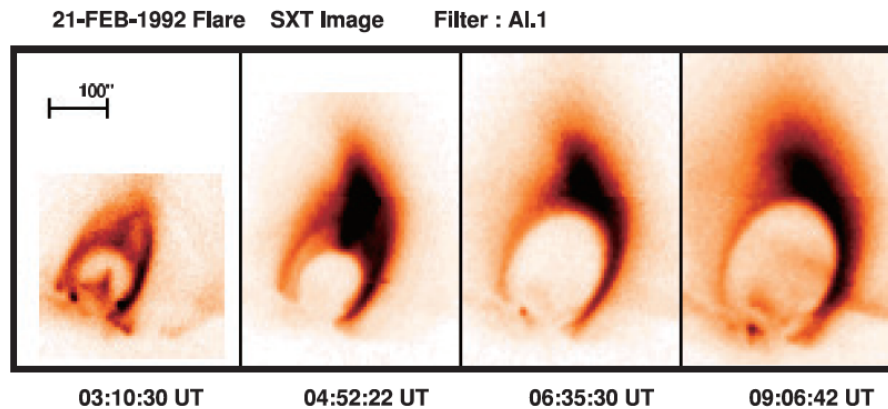


Figure 1.4: Temporal evolution of the LDE flare with a cusp-shaped loop structure (see also [Tsuneta \[1996\]](#); [Tsuneta et al. \[1992\]](#)).

It was *Yohkoh* that changed the situation of the solar flare research. The soft X-ray telescope (SXT) on board *Yohkoh* discovered a cusp-shaped loop structure of long-duration-event (LDE) flares, which is consistent with the CSHKP model. Figure 1.4 displays a famous example of a LDE flare [[Forbes and Acton, 1996](#); [Tsuneta, 1996](#); [Tsuneta et al., 1992](#)]. SXT images clearly showed that the apparent height of the cusp and the distance between the two legs increased with time. [Tsuneta et al. \[1992\]](#) found that the outer edge of the cusp-shaped loops have systematically higher temperature in the decay phase. These findings are consistent with the scenario in which magnetic reconnection successively occurred above the cusp.

In spite of those findings, the results were not sufficient enough to convince people that all the flares are caused by reconnection, because many compact, so-called impulsive flares do not show a cusp-shaped loop. It was considered that the energy release of impulsive flares occurs inside the loop, which is completely different from the picture of the reconnection models for flares. However, with the help of the hard X-ray tele-

scope (HXT) on board *Yohkoh*, Masuda et al. [1994] discovered a hard X-ray loop-top source above a soft X-ray loop in several impulsive flares (Figure 1.5), which indicates the energy release outside the soft X-ray loop. *Yohkoh* also revealed the hot plasma ejection is a common feature of the impulsive flares [Shibata et al., 1995; Tsuneta, 1997], suggesting that the overall properties of impulsive flares can also be explained by the CSHKP model. Hence, the observations strongly support the hypothesis that even impulsive flares are produced by reconnection and therefore LDE and impulsive flares have a common physics.

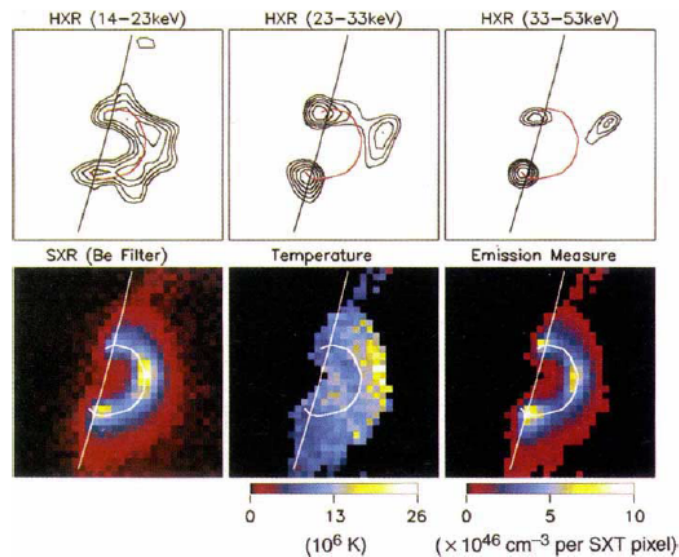


Figure 1.5: Hard X-ray (top row) and soft X-ray (bottom row) images of the 13 January 1992 flare that occurred near the west solar limb (from Masuda et al. [1994]).

Yohkoh unveiled new features in solar flares, such as cusp-shaped loops, above-the-loop-top hard X-ray sources, and hot plasmoid ejections from impulsive flares (where plasmoids are magnetically confined plasma). In addition, it also discovered new dynamic phenomena in the solar atmosphere, such as transient brightenings, X-ray jets, giant arcades associated with the filament eruption and coronal mass ejections. From observations, people found many pieces of evidence that not only flares but also other explosive phenomena are driven by magnetic reconnection. This implies a unified scenario for the explosive phenomena.

It was Shibata [1999] who proposed a unified magnetic reconnection scenario for the explosive phenomena. He noted that hot plasmoid ejections are commonly ob-

served during flares, and the plasmoid ejection is associated with the bursty energy release of flares [Ohyama and Shibata, 1997]. Considering these, he pointed out from a simple calculation that plasmoids in current sheets play significant roles in storing and impulsively releasing the energy. He proposed that apparent discrepancy among various kinds of explosive phenomena (flares, X-ray jets and so on) can be resolved if we consider magnetic reconnection between plasmoids and ambient fields. In the case of large scale flares, plasmoids will retain their coherent structures during the ejection, because of their large total magnetic flux. For this reason, the ejected flux ropes will be observed as CME. However, in the case of small scale flares, plasmoids will lose their coherent structures and disappear after the reconnection with an ambient field, because of their small magnetic flux. The remnant of the ejected plasmoids will be eventually observed as a (spinning) jet along the reconnected field lines. Since the suggestion was made, observations have gathered evidence to support the general picture of the unified model [Shimojo et al., 2007; Sterling et al., 2015]. Hence, now we can say that a reconnection model of flares and other explosive phenomena has been established, at least phenomenologically. The next step will be to clarify the detailed energy build-up and release processes and the consequences of the explosions. I believe that this is of great importance for understanding of astrophysical flares as well as solar flares.

Observations have found evidence of reconnection inflows and outflows associated with flares. Reconnection inflow was discovered by Yokoyama et al. [2001b] from Extreme UltraViolet (EUV) observations by the *Solar and Heliospheric Observatory (SOHO)*/EUV imaging Telescope (EIT) [Delaboudinière et al., 1995], and a statistical study of reconnection inflow was performed by Narukage and Shibata [2006]. The signatures of reconnection outflow were detected by spectroscopic observations [Innes et al., 2003]. The EUV Imaging Spectrometer (EIS) [Culhane et al., 2007] on board *Hinode* revealed detailed properties of hot reconnection outflows [Hara et al., 2011; Imada et al., 2013]. Continuous full-disk EUV imaging observations by Atmospheric Imaging Assembly (AIA) on board Solar Dynamics Observatory (SDO) has accumulated tremendous examples of reconnection outflows [Kumar and Cho, 2013; Liu et al., 2013; Takasao et al., 2012].

One of the fundamental problems of solar flares is how a fast reconnection is established in actual solar flares. As mentioned earlier, the Sweet-Parker model predicts a very slow reconnection if we take the system size ($\sim 10^9$ cm) as a typical length scale, and the Petschek model has a potential problem about the origin of the assumed localized resistivity. *Yohkoh* observations and MHD simulations motivated Shibata and Tanuma [2001] to propose the idea of a fractal reconnection where many plasmoids with

different sizes are created in a current sheet in a fractal manner. If this is the case, it becomes possible to shorten the current sheet and reduce the reconnection timescale. Also, it may be possible to connect a huge gap in the micro (~ 100 cm) and the macro scales. Such reconnection is recently termed as “plasmoid-dominated-reconnection,” and many theoretical investigations have been made [Bárta et al., 2011; Bhattacharjee et al., 2009; Loureiro et al., 2007]. However, there were no clear observational evidence of plasmoids in the current sheets of flares before. The first discovery of plasmoids was made by Takasao et al. [2012] from the direct EUV imaging observations by SDO/AIA (Figure 1.6). They also found that the disappearance of the plasmoids in the later phase coincides with the reduction of the reconnection rate (from 0.20 to 0.055), which is consistent with the idea that plasmoids play an important role in enhancing the reconnection rate. Observations of plasmoids were also reported by e.g. Kumar and Cho [2013]; Liu et al. [2013]; Nishizuka et al. [2015].

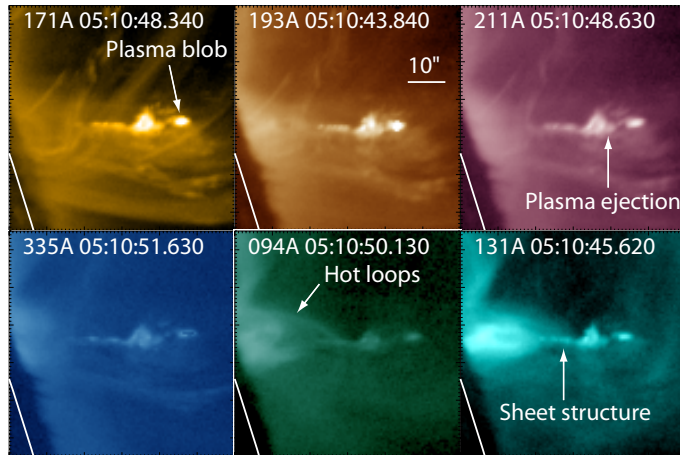


Figure 1.6: Close-up images of the reconnection site in six different wavelengths (171, 193, 211, 335, 94, and 131 Å) of AIA at the time when the current sheet, the plasma blob, and the hot flare loops are observed. White solid lines indicate the solar limb (from Takasao et al. [2012]).

Observations revealed that various kinds of oscillations are excited in solar flare regions [Liu and Ofman, 2014; Nakariakov and Melnikov, 2009]. Quasi-periodic pulsations (QPP) in the flare emissions with periods ranging from fractions of seconds to several minutes are commonly observed in a wide range of wavelengths [Nakajima et al., 1983; Nakariakov and Melnikov, 2009]. Clear QPP are often seen in the nonthermal emissions (Figure 1.7). Recent observations have found that fast mode MHD waves

are quasi-periodically emitted from some flaring sites (quasi-periodic propagating fast mode magnetoacoustic waves; QPF) [Liu et al., 2011]. The high sensitive monitoring observations by AIA enable us to study the wave properties in some events in detail [Liu et al., 2012; Yuan et al., 2013], although the statistical characteristics remains still unclear. The observed period ranges from a few 10 sec to a few 100 sec. Both of QPP and QPF imply a cyclic disturbance originating from the flaring sites. In addition, it has been pointed out that there will be a relationship between the generation of QPF and the time variability of the flare energy release (QPP) [Liu et al., 2011, 2012; Shen and Liu, 2012; Yuan et al., 2013]. However, the origins of QPP and QPF remain puzzling.

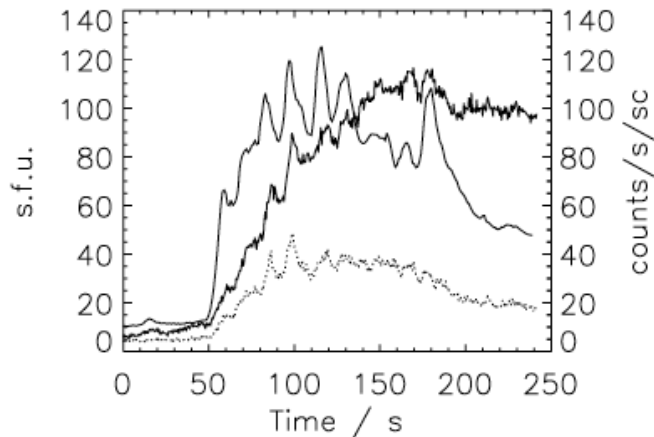


Figure 1.7: Light curves of the flare on 1998 May 8 at 01:57 UT recorded with Nobeyama Radioheliograph in 17 GHz (thick curve) and with Yohkoh/HXT in the L (13-23 keV, thin solid curve) and M1 (23-33 keV, dotted curve) channels (from Nakariakov and Melnikov [2009]). The original data is from Inglis et al. [2008]).

The studies of oscillations of flares are based on several motivations. Since the oscillatory nature is a common feature of flares, the oscillations will have potential to tell us about the fundamental mechanisms responsible for the energy release. From the point of view of the coronal seismology, the oscillations could provide local coronal plasma conditions which are difficult to directly observe. If we once understand the relationship between the oscillations and the physical parameters (such as the magnetic field strength) of flaring regions, we will be able to estimate the parameters of actual flaring regions from observations of the oscillations. The development of the coronal seismology will also contribute to the stellar coronal seismology. In most cases it is

difficult to obtain physical parameters of the stellar flares (so the parameters of the stellar coronae) from spatially resolved observations, which makes investigation of the stellar magnetic activity difficult. The stellar coronal seismological approach could provide a powerful method to investigate the stellar magnetic activity. Despite of these importance, the generation of quasi-periodic coronal waves and its causal relation to quasi-periodic pulsations in flare emissions remain unresolved. This thesis tries to reveal the relationship in Chapter 4.

1.3 What is an Active Region

Active regions are areas with an especially strong magnetic field and sunspots are commonly found (Figure 1.8). They are bright in EUV and soft X-ray, and they are the source of solar flares and other explosive phenomena (such as X-ray jets). The typical size is $\sim 10^9\text{--}10^{10}$ cm, and the total magnetic flux is typically $\sim 10^{21\text{--}23}$ Mx.

The active regions show well-organized bipolar structures, and exhibit some systematic properties, in spite of the fact that they are embedded in the turbulent convection. The active regions appear roughly within two latitudinal belts which are located nearly symmetrically on the two hemisphere. It has been known that the active region belts on both hemispheres propagate from the mid-latitude ($\sim 35^\circ$) toward the equator with the cycle of 11-year [Maunder, 1922]. Hale [1908], who established that sunspots are magnetic, found a strong tendency for the east-west alignment of magnetic polarities in sunspots, with mirror symmetry across the equator. He also noted that the polarity in each hemisphere switches orientation from one sunspot cycle to the next. This systematic property is now commonly referred to as Hale's law or the Hale-Nicholson law [Hale and Nicholson, 1925; Hale et al., 1919]. More careful observations show that the axis connecting the leading and the following polarities of each active region shows on average a small tilt relative to the east-west direction: The leading polarity is closer to the equator than the following. This tendency was first noted by Hale et al. [1919], but is now usually referred to as Joy's law. Note that the tilt angle of individual active regions show a large scatter about the mean value [Fisher et al., 1995].

Vector magnetic field observations revealed that magnetic field of many active regions have a small but statistically significant mean twist. The twist is usually defined as $\alpha = \langle J_z/B_z \rangle$, that is, the ratio of the vertical electric current to the vertical magnetic field (note that there are several ways to evaluate the average Hagino and Sakurai [2004]; Otsuji et al. [2015]). Observations indicate that active regions in the northern and southern hemispheres tend to have left-handed and right-handed twists, respec-

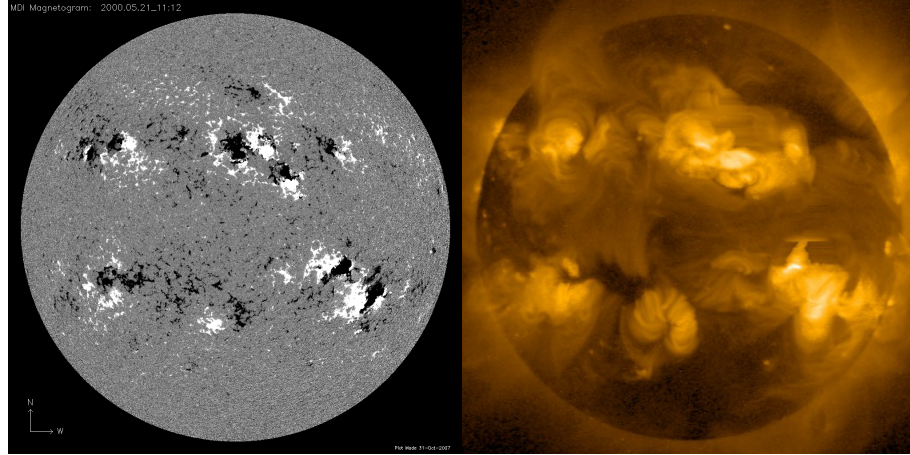


Figure 1.8: A full disk magnetogram image obtained by SOHO/MDI (Left) and a full disk soft X-ray image by Yohkoh/SXT (Right) on May 21, 2000. The magnetogram shows the line-of-sight magnetic flux density on the photosphere. White and black colors indicate a positive and negative polarities, respectively.

tively [Pevtsov et al., 1995]. The signature of the twist can be indeed found in the coronal structures. Soft X-ray observations often show S or inverse-S shape structures called “sigmoids” (Figure 1.9). The inverse-S shapes reflect the left-handed twist (so often seen in the northern hemisphere), and the S-shapes the right-handed twist (so often seen in the southern hemisphere) [Canfield et al., 1999; Rust and Kumar, 1996]. Note that the hemispheric preference of the sign of the active region twist (and therefore the direction of the sigmoids) do not change with the solar cycle [Pevtsov et al., 2001]. Investigating magnetic twist of active regions is important because the degree of magnetic twist is an indicator of the free magnetic energy available to drive flares and eruptions. Indeed, it is known that sigmoidal active regions tend to produce flares more frequently than others [Canfield et al., 1999].

The generation and maintenance of magnetic fields are believed to be controlled by a dynamo mechanism, where dynamo is a process in which a large scale magnetic field is generated and sustained by fluid motions (for a review, see e.g. Charbonneau [2014]). Hale’s law implies that there is a large scale toroidal field below the surface. The large scale toroidal magnetic field is inferred to be generated, amplified, and stored in the deep convection zone and/or a thin shear layer at the base of the convection zone called “tachocline”, where solar rotation changes from the latitudinal differential rotation of the convection zone to the nearly solid-body rotation of the radiative zone. If this is

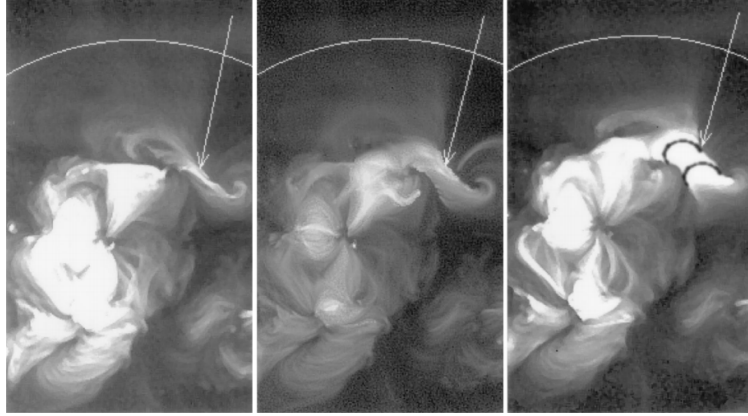


Figure 1.9: *Yohkoh* images of the solar X-ray corona on 1992 March 1992 at 19:51UT, 21:36UT, and 1:05UT (left to right) on 1992 March 28. The arrow in the leftmost image points out the reverse-S feature (“sigmoid”) that signals the onset of a flare event. In the middle, the arrow shows the beginnings of the transformation into a loop arcade. In the final image, the loop arcade is fully developed and very bright. The two black curves drawn on the image show the shape of the late-phase loops. From [Rust and Kumar \[1996\]](#).

true, the magnetic fields have to rise in the convective and rotating layer before the emergence at the photosphere. Vortical or helical motions of plasma in the convection zone may twist rising flux tubes [[Longcope et al., 1998](#)]. As for the rise of flux tubes in the convection zone and their emergence into the solar atmosphere, a review is given by [Fan \[2009\]](#).

1.4 Basic Concepts of Active Region Formation

The basic mechanism of magnetic flux emergence was first considered by [Parker \[1955\]](#) for understanding the formation of active regions and sunspots in the context of dynamo. He introduced the concept of “magnetic buoyancy” using a simple mathematics. Consider a magnetic structure embedded in the solar convection zone with magnetic field strength B is in the total pressure equilibrium with the ambient plasma:

$$p_i + \frac{B^2}{8\pi} = p_{\text{amb}}, \quad (1.3)$$

where p_i and p_{amb} are the internal and ambient gas pressures, respectively. Here it is assumed that the vertical thickness of the magnetic structure is much smaller than the

local pressure scale height, and therefore the pressure gradient of the ambient plasma can be neglected. The radiation in the convection zone will smooth out the temperature structure, so that we may assume that the magnetic structure is in thermal equilibrium with its surroundings ($T = T_{\text{amb}}$). In this case, the internal mass density becomes lower than the ambient density by a relative amount

$$\frac{\rho - \rho_{\text{amb}}}{\rho} \equiv \frac{\Delta\rho}{\rho} = -\frac{B^2}{8\pi p_i} = -\frac{1}{\beta}, \quad (1.4)$$

where $\beta = 8\pi p_i/B \gg 1$ in the convection zone. In the case that the interior and the external plasmas have the same specific entropy s (different from thermal equilibrium), the density deficit will be

$$\frac{\Delta\rho}{\rho} = -\frac{1}{\gamma_1\beta} \quad (1.5)$$

$$\gamma_1 = \left(\frac{\partial \ln p}{\partial \ln \rho} \right)_s \quad (1.6)$$

where γ_1 is Chandrasekhar's first adiabatic index [Chandrasekhar, 1967]. In either case, the magnetic structure starts to rise in the convection zone because of the buoyancy force $\Delta\rho g$. Note that apart from the buoyancy force, the upward convective flows can also contribute to the rise of the magnetic structure [Nelson et al., 2014].

The convection zone is, as its name suggests, convectively unstable, but the photosphere and chromosphere is convectively stable. Therefore, when a magnetic structure emerges from the convection zone into the photosphere, the rising must stop or be greatly decelerated at this height. This means that emergence of magnetic flux from the convection zone into the solar atmosphere is operated by other mechanisms. They are considered to be magnetic buoyancy instabilities and the action of turbulent convective flows near the photosphere. I focus on magnetic buoyancy instabilities in this thesis. As for the action of turbulent convective flows, see Cheung et al. [2010] and Cheung and Isobe [2014].

Magnetic buoyancy instabilities play a central role in magnetic flux emergence. The convectively-stable photosphere acts like a barrier for passage of magnetic flux from the interior to the chromosphere and corona, but it is shown that magnetic buoyancy instabilities aid the further rise into the solar atmosphere.

Let us consider a simple situation in which a horizontal magnetic flux sheet of finite vertical extent is embedded in a stratified layer and is initially in mechanical equilibrium

with the non-magnetic layers above and below:

$$\frac{d}{dz} \left(p + \frac{B^2}{8\pi} \right) = -\rho g \quad (1.7)$$

Note that the magnetic pressure supporting the gas above is a source of free gravitational potential energy. Also note that this equation is different from Equation 1.3, since the magnetic flux sheet is not necessarily thin compared to the local pressure scale height. The magnetic buoyancy instabilities are methods to release this free potential energy.

Figure 1.10 shows the different modes of the magnetic buoyancy instabilities. Since the magnetic field introduces a preferred direction in the plane, different modes of instability arise depending on the angle between the magnetic field \mathbf{B} and the wave vector of the perturbation \mathbf{k} [Acheson, 1979; Newcomb, 1961].

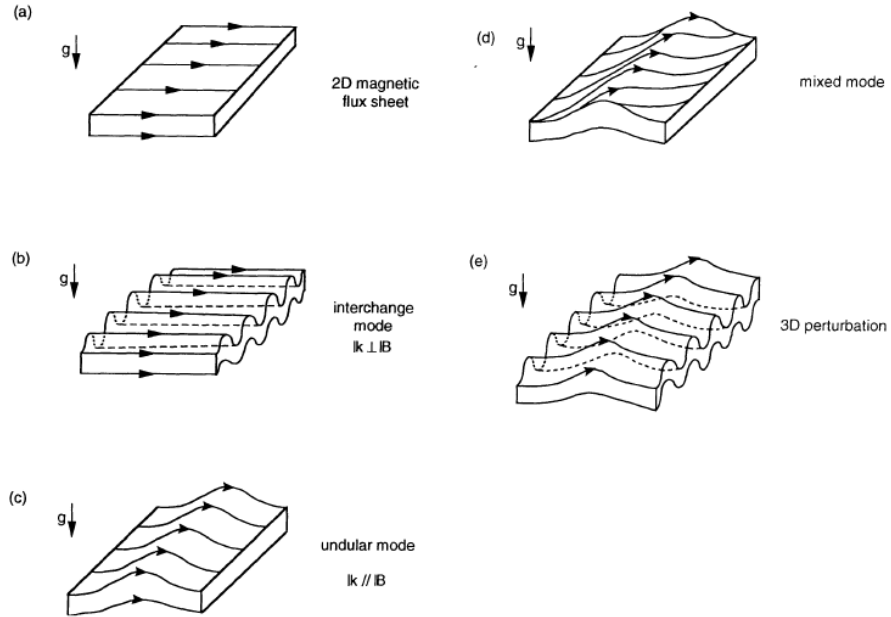


Figure 1.10: Schematic diagram of the different modes of the magnetic buoyancy instabilities of a horizontal flux sheet [Matsumoto et al., 1993].

Parker [1966] considered the undular mode ($\mathbf{k} \parallel \mathbf{B}$) as the mechanism for interstellar cloud formation (including the effect of cosmic ray pressure), and therefore this mode is often called Parker instability. Later, the same idea was applied by many authors to the rise of flux tubes in the solar interior [Acheson, 1979; Spruit and van Ballegoijen, 1982]

and to flux emergence into the chromosphere and beyond [Matsumoto and Shibata, 1992; Nozawa et al., 1992; Shibata et al., 1989a].

1.5 Phenomenological and Theoretical Modeling of Active Region Formation

It was well established in the 1980's that active regions are formed as a result of magnetic flux emergence from the solar interior to the solar atmosphere. Figure 1.11 displays a phenomenological model of flux emergence based on photospheric magnetic field and H α observations [Zwaan, 1985]. It was known that the opposite poles of bipolar regions show separation with a speed of $\sim 1 \text{ km s}^{-1}$ [Chou and Wang, 1987; Zwaan, 1978]. Using H α observations, Bruzek [1967] found evidence that magnetic loops are rising through the upper chromosphere with a speed of 10–15 km s^{-1} during the growing phase of active regions. He also found downflows with a speed of $\sim 50 \text{ km s}^{-1}$ along the rising loops. He interpreted the observations as that plasma was sliding down along the rising loops due to gravity. In the photosphere, the rising speed of the loops and the speed of downdrafts is of the order of 1 km s^{-1} [Chou and Wang, 1987; Kawaguchi and Kitai, 1976].

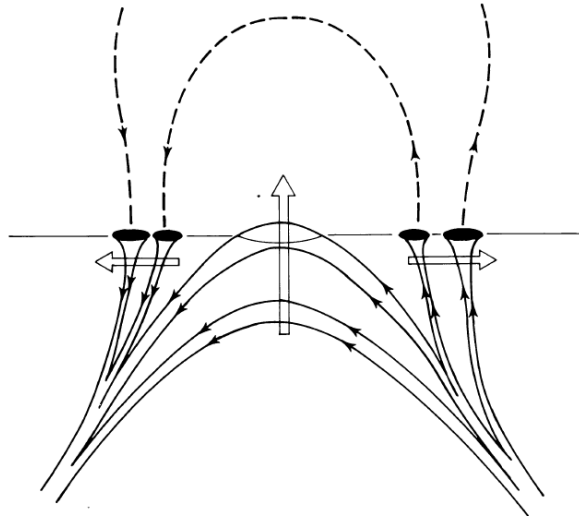


Figure 1.11: A model of flux emergence by Zwaan [1985].

Magnetic flux must rise through different atmospheric layers (from the convection zone into the convectively stable layers like the chromosphere and the corona) with huge

density contrast and change of plasma beta (from fluid dominated to magnetically dominated), the modeling of the active region formation is very difficult. For this reason, the early 2D MHD simulations by Nakagawa and Steinolfson [1976] and Forbes and Priest [1984] were limited to flux emergence into the corona in which the lower atmosphere is treated as the bottom boundary.

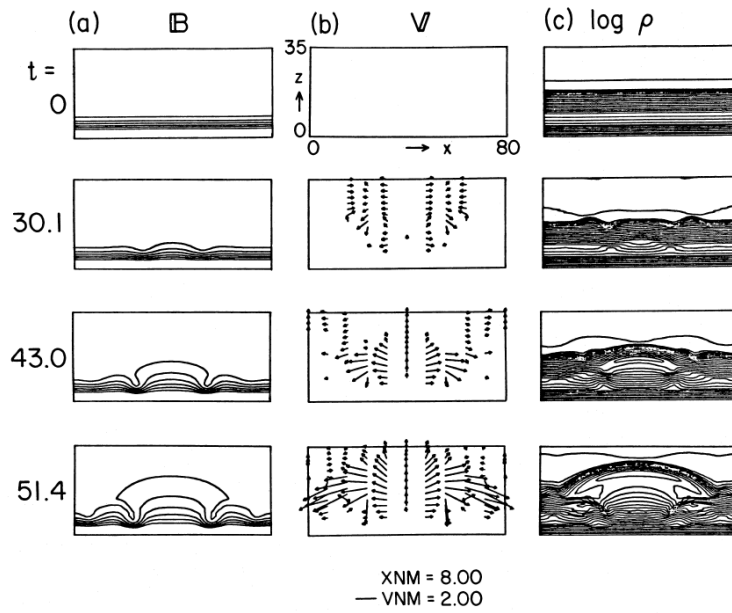


Figure 1.12: 2D MHD simulation of the Parker instability of a flux sheet embedded in the photosphere [Shibata et al., 1989a].

It was Shibata et al. [1989a,b] who first applied the Parker instability to explain the emerging flux in the solar atmosphere and performed 2D MHD simulations. I heard from him that when he was working on the problem of the Parker instability in a magnetized gas disk (e.g. galactic gas disk), he got an idea that the Parker instability can be applied to flux emergence in the solar atmosphere. Figure 1.12 displays the result of a 2D MHD simulation by Shibata et al. [1989a]. In his simulations, a flux sheet is embedded in the isothermal photosphere/chromosphere, and a small perturbation is given in horizontal velocity locally at the center of the flux sheet. Then, the perturbation leads to the initiation of the Parker instability, and the flux sheet undulates and rises into the upper atmosphere, forming Ω -loops. The Ω -loops lift up dense and cool plasma from below, and therefore they may be seen as filamentary loops in $H\alpha$. Since the height of Ω -loops is greater than many scale heights, downflows

along a field line become supersonic, forming shocks near the loop foot-points. The rise velocity of the loops ($10\text{--}15\text{ km s}^{-1}$) and the velocity of downflows along the loops ($30\text{--}50\text{ km s}^{-1}$) are consistent with observations.

The pioneering work of flux emergence has been extended further [Kaisig et al., 1990; Nozawa et al., 1992]. Matsumoto and Shibata [1992] performed the first 3D MHD simulations of solar flux emergence in which the interchange mode is allowed to appear. The initial setting is essentially the same as their previous 2D simulation, namely a (sheared in some cases) flux sheet is embedded in the photosphere/chromosphere. They confirmed that the overall behavior of emergence in 3D is similar to that of 2D simulations, indicating that the global structure is determined by the Parker instability, although the interchange mode can create fine scale structures. The consequence of interchange modes was investigated in detail by Isobe et al. [2005, 2006].

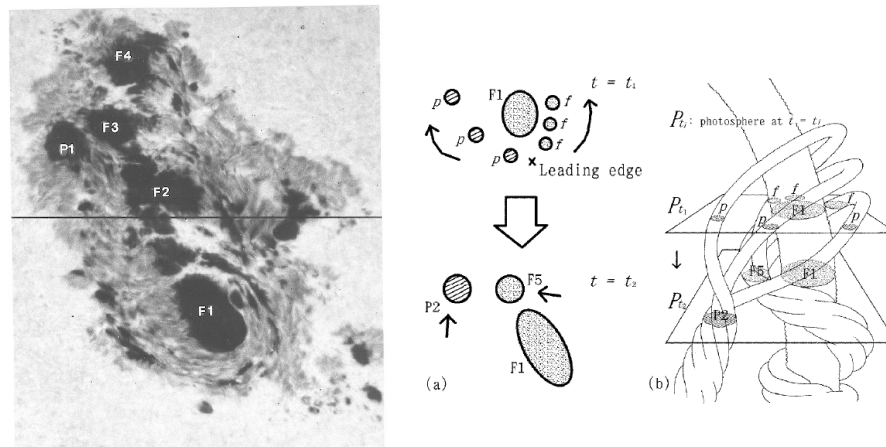


Figure 1.13: An example of the emergence of twisted flux tubes (Left) and a schematic illustration of the active region (Right) (from Ishii et al. [1998]).

Observations revealed that flare-productive active region sunspots tend to have a strong twist (e.g. Leka et al. [1996]) and sigmoidal structure seen in soft X-ray [Canfield et al., 1999]. Phenomenological models of emergence of twisted flux tubes were proposed on the basis of observations [Ishii et al., 1998; Tanaka, 1991]. Figure 1.13 displays an example of sunspots which show a strong twist (Left) and a schematic illustration of the active region (Right). The observations motivated the numerical models of the rise and emergence of twisted flux tubes. Matsumoto et al. [1998] presented the first results of 3D MHD simulations of the emergence of a highly-twisted (kink-unstable, see below) flux tube from the interior to the corona, and found that the resulting coronal

structure is similar to the sigmoidal structure in soft X-ray. [Magara and Longcope \[2001\]](#) investigated the formation of sigmoid structure. [Manchester et al. \[2004\]](#) studied the eruption of a flux rope formed in the corona as a result of the emergence of a twisted flux tube from the interior.

If a flux tube is sufficiently twisted, then it can be subject to the kink instability below the photosphere, where the kink instability is a magnetohydrodynamic (MHD) instability of a highly twisted flux tube. When the kink instability sets in, the field-line twist about the axis will be converted to the writhe of the axis as a result of helicity conservation (the twist around the axis will be reduced), and therefore the tube will be knotted or kinked [[Moffatt and Ricca, 1992](#)]. It should be noted that the twist and writhe in this case have the same sign, where a positive/negative twist (writhe) is defined as right/left-handed twist (writhe).

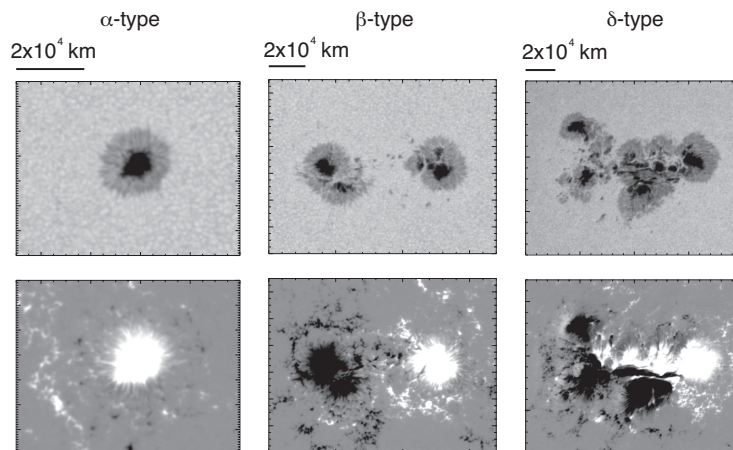


Figure 1.14: The Mount Wilson classification (top row: continuum images, bottom row: magnetogram). α -type: A sunspot group dominated by a single unipolar spot. β -type: A sunspot group that has a pair of sunspots of opposite magnetic polarity, but with a simple and distinct spatial division between the polarities. δ -type: a sunspot group in which sunspot umbrae of opposite magnetic polarities are pressed together in a common penumbra. The images are taken by HMI/SDO.

It has been known that certain photospheric structures of active regions are closely related to the flare activity. To clarify the differences of the magnetic structures of sunspots, the Mount Wilson observatory defined the classifications of magnetic structures. Figure 1.14 shows examples of basic magnetic classifications. α -spot regions have the simplest magnetic structure, and δ -spot regions have the most complex struc-

ture. The δ -spot regions are known to be among the most flare-productive active regions [Sammis et al., 2000], in which sunspot umbrae of opposite magnetic polarities are pressed together in a common penumbra. The population of the δ -spot regions is small, but they are the main source regions of the large flares (See Figure 1.15(a). According to Sammis et al. [2000], more than 80% of X-class flares occur in δ -spot regions). Takizawa and Kitai [2015] performed an observational statistical study of δ -spot regions, and clarified that δ -spot regions with a more complex structure tend to show a higher flare activity (Figure 1.15(b)).

The importance of the emergence of knotted flux tubes for the formation of isolated δ -sunspots was first pointed out by Tanaka [1991] from observations. Motivated by the observations, Fan et al. [1998] performed a 3D MHD simulation of the buoyant rise of a kink-unstable flux tube in the solar interior, and speculated that the emergence of the kinked flux tube can give rise to a compact magnetic dipole with polarity order inverted from Hale’s law, similar to the configuration often seen in δ -sunspots (see also Fan et al. [1999]; Linton et al. [1996, 1999]). However, these studies focus on the evolution in the solar interior only. Hence, the resulting photospheric and coronal magnetic structures remain unclear. This issue will be discussed in Chapter 2.

I briefly introduce tremendous progresses made in recent years in modeling of active region formation. Radiative MHD simulations of active region scale flux emergence from the interior to the middle chromosphere became possible owing to the development of computational resources [Cheung et al., 2010; Rempel and Cheung, 2014], and the approach to include the corona has just begun (Rempel, private communication). Data-driven simulations of evolving active regions have been motivated by modern observations of vector magnetic fields and/or Doppler velocity at the photosphere [Cheung and DeRosa, 2012; Mackay et al., 2011; Yeates et al., 2007], enabling us to study the energy build-up process in real active regions in detail. Those approaches have advanced our understanding of the active region formation and energy build-up processes, but still many challenges and open questions remain unresolved. For example, the back reaction of the coronal and chromospheric dynamics to the photospheric magnetic structure during flux emergence (e.g. submergence of emerged fields), which cannot be fully dealt with by the current data-driven simulations using photospheric data only, remain to be investigated. This may be important for understanding of the formation of complex δ -sunspots.

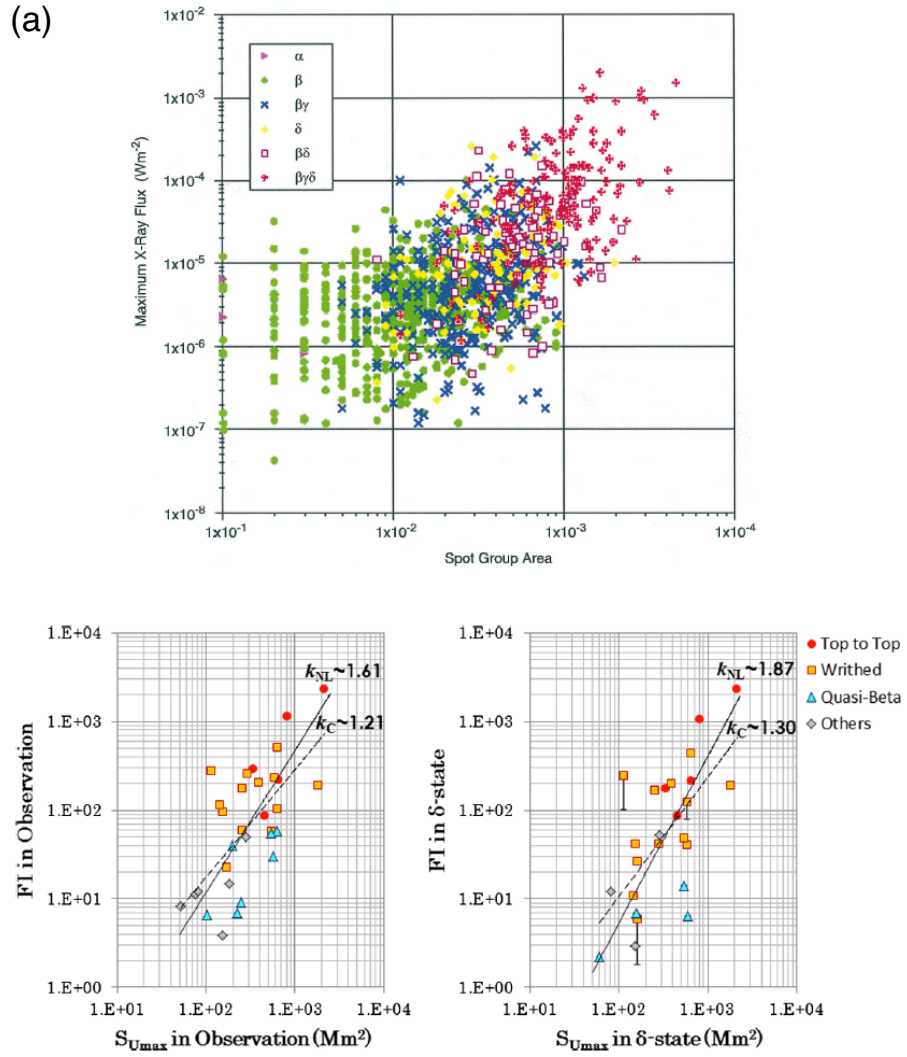


Figure 1.15: Statistical investigations of the relation between the magnetic structure of active regions and flare activity. (a) Peak flare intensities in W m^{-2} for each sunspot group as a function of peak area in disk fraction, with each magnetic class plotted separately (from Sammis et al. [2000]). (b) Flare index versus maximum umbral area on a logarithmic scale (from Takizawa and Kitai [2015]).

1.6 Outstanding Problems

With the help of observations and numerical simulations, our knowledge about the energy release by magnetic reconnection and the birth of active regions have been greatly improved. We can say that models of solar flares and active region formation have been established at least phenomenologically. However, there are still many fundamental puzzles. From a macroscopic aspect, I summarize several remaining outstanding problems below. I recognize that they are selected from a biased point of view, and not independent of each other. The problems summarized below are what I am very interested in and aim to solve in this thesis.

For the active region formation,

- What is the formation mechanism of flare-productive active regions (specifically, δ -spot regions)?
- How is a complex multipolar structure (favorable for the eruption) formed?
- How are current sheets formed during the formation of flare-productive active regions?

For the energy release of solar flares,

- What are the flow and shock wave structures in and around the flare loops?
- What causes the oscillatory nature of flares? What excites oscillations? What can we learn from the oscillations?

Modeling of a simple bipolar active region has been greatly improved recently by a number of simulations and observations, but the formation of the flare-productive active regions, specifically (isolated) δ -spot regions, remains puzzling. δ -spot regions often show complex, multipolar photospheric structures, implying an abnormal subsurface magnetic structure. However, we have currently no method to speculate the subsurface magnetic configuration of emerging fields before the emergence, which makes it difficult to deduce the subsurface structure. Reconnection in current sheets formed above such multipolar structures will lead to the onset of flares and eruptions, but the formation process of the current sheets is not obvious. To model the energy buildup and eruption during the evolution of active regions, nonlinear force-free-field modeling has been widely adopted. However, because the method neglects the effect of the gas pressure and gravity (i.e. zero- β approximation), the modeling may miss some important keys. Hence, the understanding of the evolution of the 3D field structure in the

different layers (from the convection zone to the corona) based on 3D MHD simulations is necessary. This issue will be discussed in Chapter 2.

Shocks in and above the flare loops is believed to play an important role in the non-thermal particle acceleration and the evolution of the thermal structure of the loops, but because of the difficulty in performing high-resolution flare simulations and observations, the detailed structure has not been fully understood yet. Waves can be used as a powerful tool to diagnose the coronal magnetic field configuration and local condition of the plasma emitting the waves [Liu and Ofman, 2014; Nakariakov and Melnikov, 2009]. The development of the coronal seismology will also contribute to the stellar coronal seismology. However, we have very less knowledge about the excitation mechanisms and sites of waves during flares. By resolving the puzzles, I aim to update the current view of solar flares. Shocks in and above the flare loops will be investigated in Chapter 3. The oscillation excited in the flare loops will be discussed in Chapter 4.

Chapter 2

Formation of Flare-Productive Active Regions

2.1 Introduction

As introduced in Chapter 1, magnetic flux emergence from the solar interior to the overlying atmosphere is responsible for the formation of active regions [Cheung and Isobe, 2014; Fan, 2009; Parker, 1979], and therefore it is the driver of various explosive phenomena [Shibata and Magara, 2011; Takasao et al., 2013]. The free energy buildup in the corona during flux emergence, which is essential for the eruptive events, has been extensively studied by many authors [Cheung and DeRosa, 2012; Fang et al., 2012; Magara and Longcope, 2003; Manchester et al., 2004].

It has been known that certain photospheric configurations of active regions are closely related to the flare activity [Kurokawa, 1989; Zhongxian and Jingxiu, 1994]. The so-called "δ-spot regions" are known to be among the most flare-productive active regions [Sammis et al., 2000], in which sunspot umbrae of opposite magnetic polarities are pressed together in a common penumbra. The population of the δ-spot regions is small, but they are the main source regions of the large flares (According to Sammis et al. [2000], more than 80% of X-class flares occur in δ-spot regions). In this sense, δ-spot regions have a significant impact on the space weather.

Observations show that a fraction of the δ-spot regions have strong magnetic shear along the polarity inversion line and emerge with polarity orientations not following the Hale-Nicholson and Joy Laws (hereafter, Joy's law) obeyed by the majority of active regions [Zirin and Liggett, 1987]. It is speculated from observations that they are formed as a result of the emergence of current-carrying (twisted) flux tubes [e.g. Leka et al.,

1996], which implies that a considerable amount of the free energy is stored in such δ -spot regions. In addition, they tend to appear with complex multipolar spots [Ishii et al., 1998; Zirin and Tanaka, 1973]. Multipolar regions are generally more favorable for the ejections than bipolar regions [Antiochos, 1998], because smaller energy is enough for plasma to escape from the closed magnetic field region (the number of the field lines that plasma has to stretch is much smaller than that for the bipolar systems). Therefore, their strong magnetic shear and multipolar structure are important characteristics of the flare-active δ -spot regions.

It is suggested that δ -spot regions are formed as a result of the emergence of the twisted flux tubes with an abnormal structure. Tanaka [1991] analyzed the time evolution of the August 1972 δ -spot region in detail. He found that the behavior of this region can be explained by the emergence of a twisted flux tube with a knotted structure, and the twist and writhe of the flux tube having the same sign. Tanaka [1991] pointed out the importance of the kink instability for the formation of isolated δ -sunspots. Kurokawa et al. [2002] also reported an event which is likely related to the emergence of a knotted flux tube.

It is believed that the sign of the tilt angle of an active region with respect to the solar equator can be used as a proxy for the sign of the writhe. Therefore, investigating the relation of the sign for the twist and tilt from observations is an important step to check the possibility of the kink instability scenario. Statistical studies of the correlation between active region twist and tilt angles have been performed [Holder et al., 2004; Tian and Liu, 2003; Tian et al., 2005]. Holder et al. [2004] found a significant correlation between active region twist and tilt angles by analyzing 368 active regions, where the correlation between them denotes that twist and writhe have the same sign. They identified that the correlation is mainly contributed by those active regions (174 of 368 regions) that deviate significantly from Joy's law. Tian et al. [2005] obtained a similar result by surveying 104 δ -spot regions. Takizawa and Kitai [2015] also confirmed this result by looking at the birth phase of the 31 flare-productive δ -spot regions in the cycle 23. Detailed case studies (e.g. López Fuentes et al. [2003]; Tanaka [1991]) have shown that a non-negligible fraction of these active regions seems formed by the emergence of kinked flux tubes with the same sign for twist and tilt. Nandy [2006] found the tendency that δ -spot regions have stronger twist than others, which may support the idea of the kink instability scenario.

There are several theoretical investigations of kink unstable flux tubes in the context of the formation of flare-productive active regions [Fan et al., 1999; Linton et al., 1996, 1999; Matsumoto et al., 1998]. Matsumoto et al. [1998] performed the first 3D MHD

simulations of the emergence of kinked flux tubes into the corona, and they argued that the emergence of kinked flux tubes can explain the formation of a sequence of (strongly sheared) S-shaped active regions. [Linton et al. \[1999\]](#) studied basic properties of a kink unstable flux tube with high plasma- β , but neglected gravitation, where the plasma- β is defined as the ratio of the gas pressure to the magnetic pressure. [Fan et al. \[1999\]](#) performed several sets of MHD simulations of the rise of kink unstable flux tubes in the interior of the Sun. They found that the kinking motion is promoted by the gravitational stratification, and that a kinked tube has strong shear along the polarity inversion line (PIL) in the buckled part. Since the models by [Linton et al. \[1996\]](#) and [Fan et al. \[1999\]](#) are confined to the solar interior, it remains unclear if the kinked tube can emerge into the atmosphere to produce the observational characteristics of δ -spot regions. Moreover, another important observational feature is that many δ -spot regions contain multipolar spots (e.g. [Zirin and Tanaka \[1973\]](#)), which is not explained by the kinked tube model of [Linton et al. \[1996\]](#) and [Fan et al. \[1999\]](#).

Other mechanisms to form δ -spot regions have also been considered. For instance, [Toriumi et al. \[2014\]](#) and [Fang and Fan \[2015\]](#) performed MHD simulations of the emergence of a single twisted (kink stable) flux tube with two buoyant segments, and they successfully obtained δ -spot-like regions as a result of the collision of the non-paired spots. [Toriumi et al. \[2014\]](#) showed that the sheared polarity inversion line does not form when the pair of photospheric bipoles are due to the emergence of two adjacent (but unconnected) flux tubes. Considering their result, the multipolar spots should be magnetically connected below the surface to keep the active region compact.

Here, we present the results of an MHD simulation in which a subsurface twisted kink-unstable flux tube emerges from the solar interior into the corona. From this simulation we found that a complex quadrupole structure is spontaneously formed as a result of the emergence of a single kinked flux tube. The remainder of the chapter is structured as follows. Section 2.2 provides some basic properties of the kink instability. Section 2.3 describes the numerical setup of our simulation. In Section 2.4, we show numerical results of the emergence of a kinked flux tube, and briefly compare our simulation with observations. Finally, in Section 4.4, we discuss our findings through comparison with previous studies, and also discuss the implications of this work for understanding of the formation of δ -spot regions.

2.2 Kink Instability of a Twisted Flux Tube Confined in Unmagnetized Plasma

Before we introduce the results, we will provide some basic properties of the kink instability. The initial investigation of the kink instability of a twisted flux tube in an electrically conducting cylinder or in a toroidal magnetic field was carried out by [Kruskal and Schwarzschild \[1954\]](#); [Kruskal et al. \[1958\]](#); [Lundquist \[1951\]](#). It is found that for any twist, the flux tube is unstable to a helical kink with a certain wavenumber [[Priest, 1982](#)]. This finding greatly emphasizes the importance of twist in determining the evolution of the flux tube, but the result cannot be directly applied to the case of flux tubes in the interior of the Sun, because they are embedded in the high- β plasma.

It is [Linton et al. \[1996\]](#) that for the first time investigated the linear kink instability of a flux tube of a isolated, twisted magnetic flux tube confined by the pressure of the unmagnetized plasma. They concentrated on equilibria where a flux tube is uniformly twisted: $B_\theta/rB_x = q = \text{const.}$ Important findings of their study are as follows:

1. There is a minimum twist that a tube must have in order to be kink unstable: $q_{\text{cr}} = A^{1/2}$, where A is the r^2 coefficient in the Taylor series expansion of the equilibrium axial magnetic field B_x about the tube axis ($r = 0$), that is, $B_x(r) = B_0(1 - Ar^2 + \dots)$. Thus if we take a Gaussian profile for the axial field ($\exp(-r^2/a^2)$), $q_{\text{cr}} = 1/a$.
2. When the twist q exceeds this threshold q_{cr} , the tube is subject to the kink instability. The most unstable mode has a helical wavenumber k which is near but not equal to the field line pitch q .
3. The maximum growth rate for a strongly twisted tube ($qa \gtrsim 1$, where a is the radius of the tube) is given by $\omega_{\text{max}} \simeq 0.25v_A a(q^2 - q_{\text{cr}}^2)$, where v_A is the axial Alfvén speed. If we take $q = 1.5/a$, then $\omega_{\text{max}} \simeq 0.1v_A/a$.
4. The range of unstable wavenumbers is $-q - \Delta k/2 < k < (-q + \Delta k/2)$, where $\Delta k \simeq qa(q^2 - q_{\text{cr}}^2)^{1/2} \simeq 2qa(\omega_{\text{max}}/v_A a)^{1/2}$. If we take $q = 1.5/a$, then $\Delta k \simeq 0.6q$.

[Fan et al. \[1999\]](#) noted that the growth time for the fastest growing kink mode (τ_{min}) should be smaller than the rise time of a tube through the convection zone. The rise time τ_{rise} can be estimated as $\tau_{\text{rise}} \sim H_p/v_{\text{rise}}$, where H_p is the pressure scale height and $v_{\text{rise}} \sim (a/H_p)^{1/2}v_A$ is the rise velocity [[Parker, 1975](#)]. If we take $a \sim 0.1H_p$, then $\tau_{\text{rise}} \sim 30(a/v_A)$. It is found that τ_{min} becomes comparable to τ_{rise} when $q \simeq 1.34/a$,

which means that one can expect a significant kinking of the tube axis during the rise of a tube if the initial twist q is greater than this value.

It is also possible that a tube becomes unstable to the kink instability even if the initial twist is smaller than this value, because the expansion of the tube makes it more kink unstable through the reduction of the threshold of the twist (since $q_{\text{cr}} = 1/a$ in the case of a Gaussian profile). Considering the magnetic flux conservation, we obtain the following:

$$B_z a^2 = \text{const} \quad (2.1)$$

$$B_\theta a = \text{const.}, \quad (2.2)$$

which gives $B_x/B_\theta \propto a^{-1}$. This illustrates a basic reason why the azimuthal field can be dominant against the axial field as a result of the expansion and why the tube can become more unstable to kinking. The expansion during its rise is caused by the density stratification. Since $q_{\text{cr}} = a^{-1} \propto \rho^{1/2}$ in the case that the flux tube cross-section expands self-similarly, the rise of the twisted tube leads to the decrease of q_{cr} and the enhancement of the kink instability. Parker [1974] showed that an expanded segment of a twisted flux tube becomes more kink unstable. He found that the helical coils are propelled onto the expanded portion to achieve the torque balance. The magnetic flux surface forms a coil spring, which is weak in the expanded segment and strong in the unexpanded part. The magnetic field of the expanded segment is too weak to resist. As a result, the spring in the unexpanded part dominates and coils is transferred from the unexpanded part to the expanded segment. Hence, the expanded segment becomes more twisted, and more unstable to buckling. The shifting coils is essentially the propagation of torsional Alfvén waves launched by the mismatch of the torque.

2.3 Numerical Setup

2.3.1 Basic Equations

We solved the MHD equations in the following form:

$$\frac{\partial \rho}{\partial t} = -\nabla \cdot (\rho \mathbf{v}), \quad (2.3)$$

$$\frac{\partial \rho \mathbf{v}}{\partial t} = -\nabla \cdot \left[\rho \mathbf{v} \mathbf{v} + \left(p + \frac{|B|^2}{8\pi} \right) \mathbf{1} - \frac{\mathbf{B} \mathbf{B}}{4\pi} \right] + \rho \mathbf{g}, \quad (2.4)$$

$$\frac{\partial \mathbf{B}}{\partial t} = -\nabla \cdot (\mathbf{v} \mathbf{B} - \mathbf{B} \mathbf{v}) - \nabla \times (\eta \nabla \times \mathbf{B}), \quad (2.5)$$

$$\frac{\partial e}{\partial t} = -\nabla \cdot \left[\mathbf{v} \left(e + p + \frac{|B|^2}{8\pi} \right) - \frac{1}{4\pi} \mathbf{B} (\mathbf{v} \cdot \mathbf{B}) \right] + \frac{1}{4\pi} \nabla \cdot (\mathbf{B} \times \eta \nabla \times \mathbf{B}) + \rho (\mathbf{g} \cdot \mathbf{v}), \quad (2.6)$$

$$e = \frac{p}{\gamma - 1} + \frac{\rho |\mathbf{v}|^2}{2} + \frac{|\mathbf{B}|^2}{8\pi}, \quad (2.7)$$

where ρ is the density, \mathbf{v} is the velocity vector, \mathbf{B} is the magnetic field vector, e is the total energy density, and p is the gas pressure. γ is the specific heat ratio (here 5/3). The equation of state for the ideal gas is used. The gravity $\mathbf{g} = -g_0 \hat{\mathbf{z}}$ is a constant vector and the non-dimensional form is given by $\mathbf{g} = (0, 0, -1/\gamma)$. The normalization units of our simulations are summarized in Table 2.1. In the expanding magnetic field in the corona, the plasma β can become very small, where the calculated gas pressure can be negative due to numerical errors. To avoid the numerical instability, the energy equation in the low-beta ($\beta < 0.01$) regions is replaced by the following equation:

$$\frac{\partial e_{int}}{\partial t} = -\nabla \cdot (\mathbf{v} e_{int}) - (\gamma - 1) e_{int} \nabla \cdot \mathbf{v}, \quad (2.8)$$

where $e_{int} = p/(\gamma - 1)$. In Equation 2.5, η is the magnetic diffusivity, and an anomalous resistivity model is assumed:

$$\eta = \begin{cases} 0 & (J < J_c \text{ or } \rho > \rho_c) \\ \eta_0 (J/J_c - 1) & (J \geq J_c \text{ \& } \rho < \rho_c), \end{cases} \quad (2.9)$$

where $\eta_0 = 0.1$, $J_c = 0.1$ and $\rho_c = 0.1$. Density is normalized such that $\rho = 1$ corresponds to the density at the photospheric base (see also Table 2.1). Thus, the resistivity works only in the region where the current density is strong above the photosphere.

The numerical scheme is based on Vögler et al. [2005]: Spatial derivatives are calculated by the 4th-order central differences and temporal derivatives are integrated

Table 2.1: Normalization units for the flux emergence simulation

Quantity	Unit	Value
Length	H_{p0}	170 km
Velocity	$C_{s0} = [\gamma(k_B/m)T_0]^{1/2}$	6.8 km s ⁻¹
Time	$\tau = H_p/C_{s0}$	25 s
Temperature	$T_0 = T_{ph}$	5,600 K
Density	$\rho_0 = \rho_{ph}$	1.4×10^{-7} g cm ⁻³
Pressure	$\gamma(k_B/m)\rho_0T_0$	6.3×10^4 dyn cm ⁻²
Magnetic field strength	B_0	250 G

by a 4-step Runge-Kutta scheme. We also adopt the artificial diffusion term described in [Rempel et al. \[2009\]](#) to stabilize the numerical calculation. Errors caused in $\nabla \cdot \mathbf{B}$ are controlled by using an iterative hyperbolic divergence cleaning method, where the cleaning technique is based on the method described in [Dedner et al. \[2002\]](#).

2.3.2 Initial and Boundary Conditions

The initial background atmosphere consists of three regions: an adiabatically stratified static atmosphere (representing the convection zone), a cool isothermal layer (photosphere/chromosphere), and a hot isothermal layer (corona) (see Figure 2.1 (a)). The initial distribution of temperature is given as

$$T(z) = T_{ph} - \left. \frac{dT}{dz} \right|_{ad} z \quad (2.10)$$

for the convection zone ($0 \leq z \leq z_{ph}$), and

$$T(z) = T_{ph} + (T_{co} - T_{ph}) \left\{ \frac{1}{2} \left[\tanh \left(\frac{z - z_{tr}}{w_{tr}} \right) + 1 \right] \right\}, \quad (2.11)$$

for the upper atmosphere ($z \leq z_{ph}$), where T_{ph} and T_{cr} are the temperatures in the photosphere and the corona, and are set to T_0 and $150T_0$, respectively. $|dT/dz|_{ad} \equiv (\gamma - 1)/\gamma$ is the adiabatic temperature gradient. The photospheric height is $z_{ph} = 80H_{p0}$, and the transition region between the chromosphere and the corona is located at $z_{tr} = z_{ph} + 18H_{p0} = 98H_{p0}$. The width of the transition w_{tr} is set to $2H_{p0}$. A magnetic flux tube is initially located below the photosphere (the depth is ~ 10 Mm).

The longitudinal and azimuthal components of the flux tube are respectively given by

$$B_x(r) = B_{\text{tube},0} \exp\left(-\frac{r^2}{R_{\text{tube}}^2}\right), \quad (2.12)$$

$$B_\theta(r) = \alpha \frac{r}{R_{\text{tube}}} B_x(r), \quad (2.13)$$

where $r = [y^2 + (z - z_{\text{tube}})^2]^{1/2}$, $z_{\text{tube}} = 18H_{p0}$, and $B_{\text{tube},0} = 53B_0$. $R_{\text{tube}} = 5H_{p0}$ is the radius of the tube. These profiles are truncated at $r = 3R_{\text{tube}}$. The total magnetic flux of 3×10^{20} Mx is assumed. The plasma β at the center of the initial tube is approximately 20. α is a measure of the twist of the flux tube, and is set to -1.5 (negative sign denotes the left-handed twist). Note that α is defined as a non-dimensional constant here. α/R_{tube} gives the rate of field line rotation per unit length along the tube. The absolute value of α is larger than the critical value for the kink instability, 1, and therefore the flux tube is initially kink-unstable. The vertical distributions of the density, pressure, temperature, and magnetic field strength in the initial condition are shown in Figure 2.1 (b).

The simulation domain is $(-124H_{p0}, -124H_{p0}, 0) \leq (x, y, z) \leq (124H_{p0}, 124H_{p0}, 294H_{p0})$ resolved by a $600 \times 600 \times 740$ grid. In the x and y -directions, the mesh size is $\Delta x = \Delta y = 0.25H_{p0}$ within $|x|, |y| < 30H_{p0}$ and gradually increases up to $0.8H_{p0}$ for $|x|, |y| > 30H_{p0}$. In the z -direction, the mesh size is $\Delta z = 0.24H_{p0}$ within $0 \leq z \leq z_{ph} + 40H_{p0}$, and for $z > z_{ph} + 40H_{p0}$, it gradually increases up to $1.6H_{p0}$. To facilitate investigation of the coupling between the kink and Parker instabilities, we take a domain size large enough to allow the latter to develop. The critical wavelength for it is ~ 9 times the local pressure scale height, $\sim 230H_{p0}$, which is comparable to or smaller than the calculation domain size in the x -direction, $248H_{p0}$.

We make the flux tube buoyant by introducing a small perturbation to the density in the flux tube. The perturbation is described as

$$\rho = \rho_0 [1 - a(x)], \quad (2.14)$$

$$a(x) = \frac{1}{\beta} [(1 + \epsilon) \exp(-x^2/\lambda^2) - \epsilon], \quad (2.15)$$

where ρ_0 is the unperturbed density, $\epsilon = 0.2$ and $\lambda = 15H_{p0}$. We have checked that the evolution of the rising flux tube is not sensitive to the wavelength of the initial perturbation.

The boundaries in the x -direction (the direction of the initial flux tube axis) are assumed to be periodic. The boundaries in the y and z -directions are assumed to be

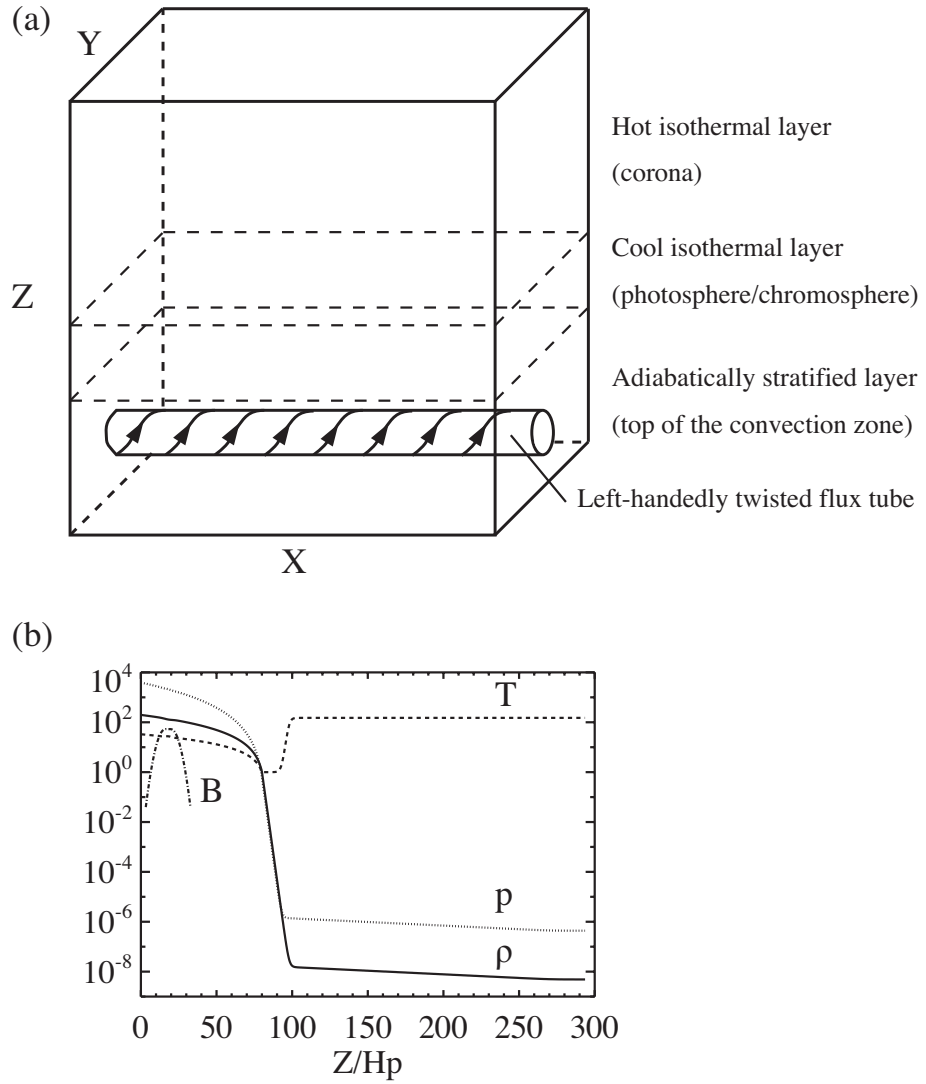


Figure 2.1: Initial setup of the simulation. (a) Schematic diagram of the model atmosphere and initial flux tube. (b) Vertical distributions of the density ρ (solid), pressure p (dotted), temperature T (dashed), and magnetic field strength B (dashed dotted line) in the initial condition. See Table 2.1 for the normalization units.

a perfectly conducting wall and is non-penetrating. Many previous studies adopted a free boundary condition for the top boundary, but we applied the non-penetrating boundary for it to avoid numerical instabilities arising from the use of a free boundary condition. The top boundary is located at a much higher position ($z = 294H_{p0}$) than the top of the emerging coronal loops ($z \sim 200H_{p0}$), and therefore the top boundary will not significantly affect the evolution of the flux emergence process.

2.4 Numerical Results

2.4.1 Evolution of Flux Tube in the Solar Interior

The rise of the flux tube with a single buoyant segment is shown in Figure 2.2. Since the tube is initially kink-unstable, the knotted structure develops during the rise, as in the previous study by Fan et al. [1999]. In this study, the box size in the x -direction is ~ 9 times larger than the pressure scale height at the initial tube axis, whereas they are similar in Fan et al. [1999]. With the larger domain size, the rising tube develops a Ω -shape with a central kinked part.

To examine the deformation and expansion of the apex of the rising tube, we looked at the relation between the plasma density and the magnetic field strength of the most buoyant part. We confirmed that the magnetic field strength of the most buoyant part can be well described by $B \propto \rho^{1/2}$ (see Figure 2.3), which means that the flux tube experiences a strong horizontal expansion during its rise to the surface [Cheung et al., 2010]. The strong horizontal expansion leads to the formation of a pancake-like (flat, horizontally extended) magnetic distribution below the surface (see Figure 2.2). Because of the deformation by the kinking and the strong horizontal expansion, it is difficult to deduce the resulting photospheric and coronal magnetic structures only from the magnetic structure of the rising kinked flux tube in the interior of the Sun.

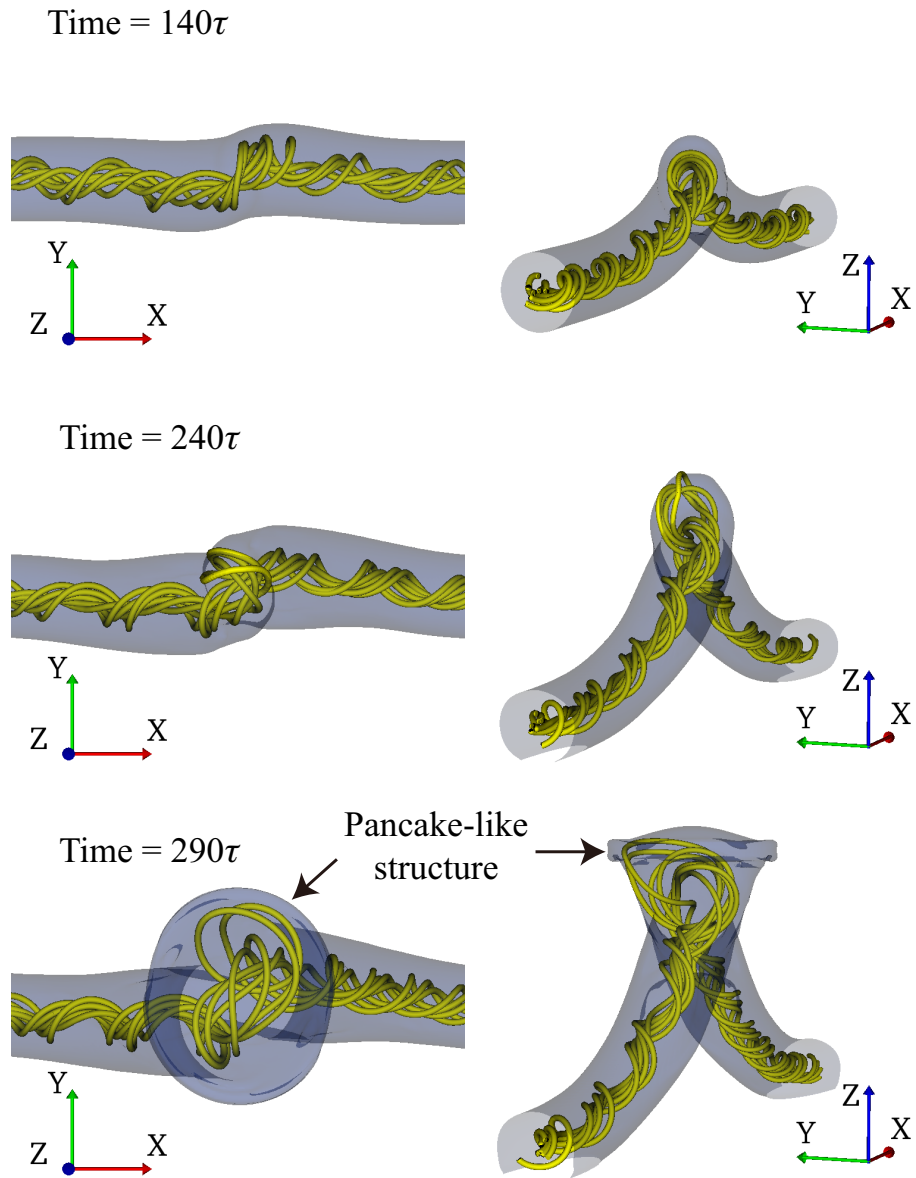


Figure 2.2: The rise of the flux tube in the solar interior. The yellow lines denote the selected magnetic field lines, and the blue surfaces indicate the isosurface where $B = 2B_0$.

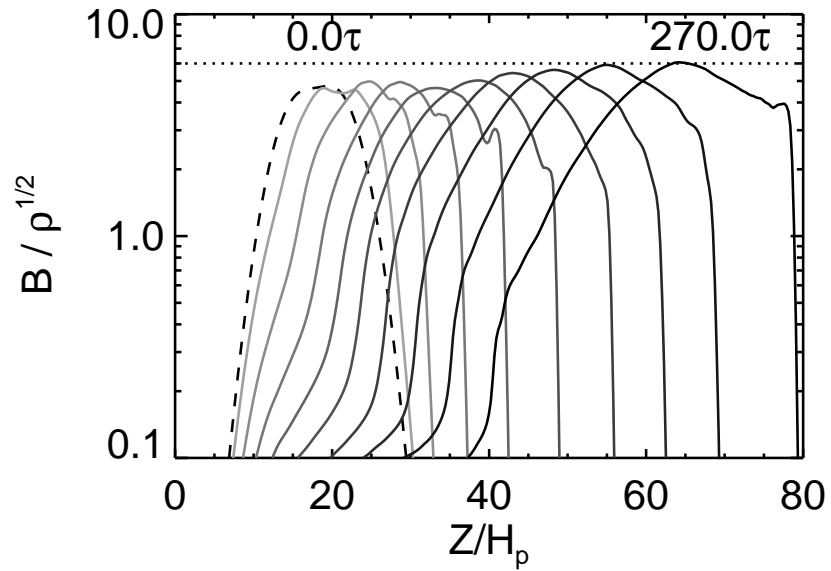


Figure 2.3: Temporal evolution of the ratio of the magnetic field strength B to the square root of the density $\rho^{1/2}$. The ratio is measured along the z -axis crossing the point $(x, y) = (0, 0)$. The dashed line denotes the initial profile. The solid lines with different colors indicate the profiles at different times. The time interval between successive plots is 30τ .

2.4.2 Formation of Complex Quadrupole Structure at Photospheric Level

The evolution of the vertical components of the photospheric ($z = 80H_{p0}$) and chromospheric ($z = 96H_{p0}$) magnetic field, B_z , is displayed in Figure 2.4. At the beginning of the emergence ($t = 305\tau$), a pair of opposite polarity spots (we call them the “main pair”) appear with a large inclination with respect to the initial axis direction (x -direction). As time progresses, another pair of strong magnetic regions appear at the middle of the main pair of spots (called the “middle pair”). Later, the structure of the middle pair becomes disordered, although the main spots show a coherent structure and strong twist. The main pair and middle pair have the maximum field strength of $\sim 10B_0$ and $\sim 3-4B_0$, respectively.

In order to describe the motion of this quadrupole region, we measured the flux-weighted centroids of positive and negative polarities (x_{\pm}, y_{\pm}), where

$$(x_{\pm}, y_{\pm}) = \left(\frac{\Sigma x B_{z,\pm}}{\Sigma B_{z,\pm}}, \frac{\Sigma y B_{z,\pm}}{\Sigma B_{z,\pm}} \right). \quad (2.16)$$

Relative motion of the positive and negative polarities at the photosphere is shown in Figure 2.5. The centroid position for each polarity is computed including all the parts of that polarity (i.e. include both the main pair and the middle pair). The tilt angle of this region, measured from the positive x -direction, is large at the beginning of the emergence (note that the direction of the initial tube axis is in the x -axis). However, it becomes smaller later. This change may be regarded as a clockwise motion of this region, as predicted by the emergence of a knotted tube with a left-handed twist [Linton et al., 1999; Tanaka, 1991]. We note that the distance between the flux-weighted centers of the opposite polarities increases as time progresses.

It should be noted that a complex quadrupole structure is formed by the emergence of a kinked tube with a single buoyant segment, not with two buoyant segments assumed in the previous studies by Toriumi et al. [2014] and Fang and Fan [2015]. The narrow middle pair becomes prominent well after the emergence of the main pair, and its structure gets disordered, but the chromospheric B_z maps in Figure 2.4 show a more smooth quadrupole distribution than the photospheric distribution.

We investigated the formation of the middle pair. Figure 2.6 shows the temporal evolution of the vertical velocity v_z at the center $(x, y) = (0, 0)$ during the formation. Magnetic field is rising in the early phase ($t = 310\tau$), but later v_z becomes negative, which means the submergence of emerged magnetic fields. Figure 2.7 (a) displays the

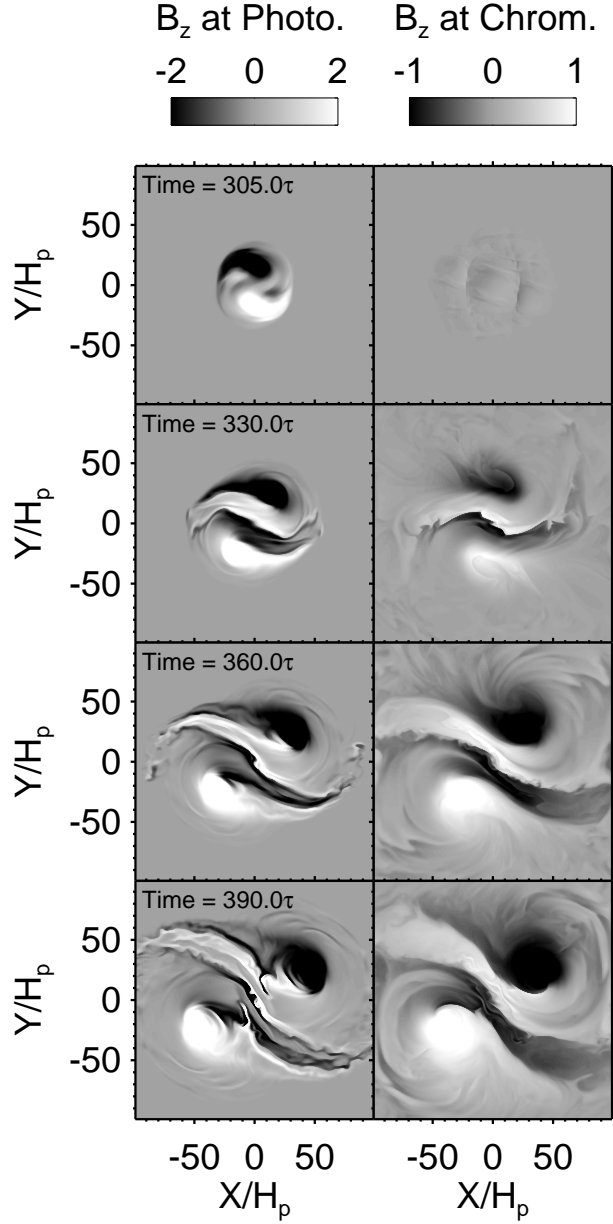


Figure 2.4: Temporal evolution of the photospheric (Left) and chromospheric (Bottom) line-of-sight magnetic fields B_z . The heights of the photospheric and chromospheric planes are $80H_{p0}$ and $96H_{p0}$, respectively. $H_{p0}=170 \text{ km s}^{-1}$, and $\tau=25 \text{ s}$.

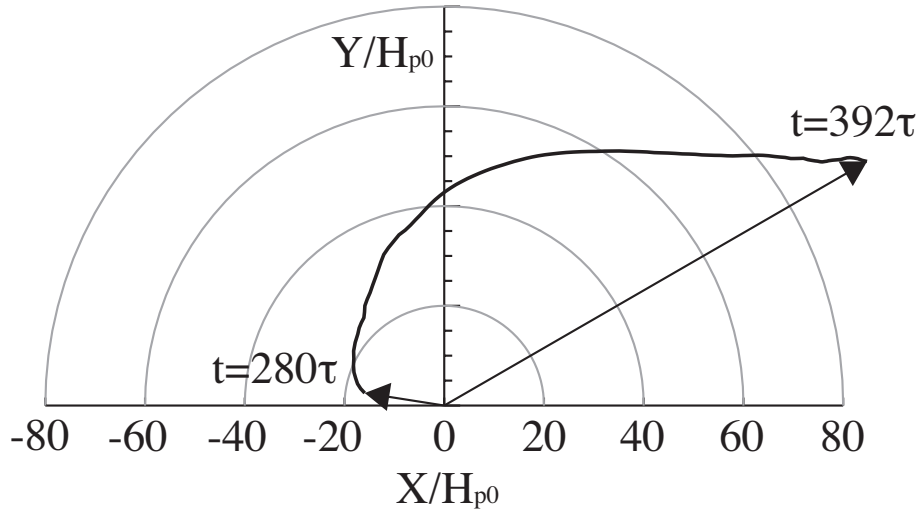


Figure 2.5: Temporal evolution of the direction and distance from the centroid of the positive polarity region to the centroid of the negative polarity region. The centroids are defined by Equation 2.16. $H_{p0}=170 \text{ km s}^{-1}$, and $\tau=25 \text{ s}$.

3D magnetic field evolution, where it is shown that the middle pair is formed as emerged magnetic fields submerge. For this reason, the middle pair appears after the formation of the main pair. To clarify the cause of the submergence, we measured the vertical forces at the center. Figure 2.7 (b) indicates that the sum of the upward Lorentz force and pressure gradient becomes weaker than the downward gravitational force, which means that the submergence is caused by the downward motion of the heavy material.

2.4.3 Evolution of Coronal Magnetic Field

Figure 2.8 (a-c) illustrate the evolution of the magnetic field and density distribution in the $y-z$ plane at $x = 0$. Two magnetic flux concentrations are located just below the photosphere at the beginning of the emergence ($t = 300\tau$) with a single arcade field emerging into the atmosphere. In this model, as in many previous numerical models of emerging flux, the expansion of the magnetic arcade into the atmosphere is enabled by a magnetic Rayleigh-Taylor instability [Archontis et al., 2004; Matsumoto et al., 1993; Shibata et al., 1989b]. As the expanding arcade plows through the atmosphere, plasma is compressed above the arcade, leading to a top heavy layer (see Figure 2.8 panel d). Due to the continued emergence of the two strong flux concentrations, and the comparatively weaker twist at the middle between the two concentrations, the top

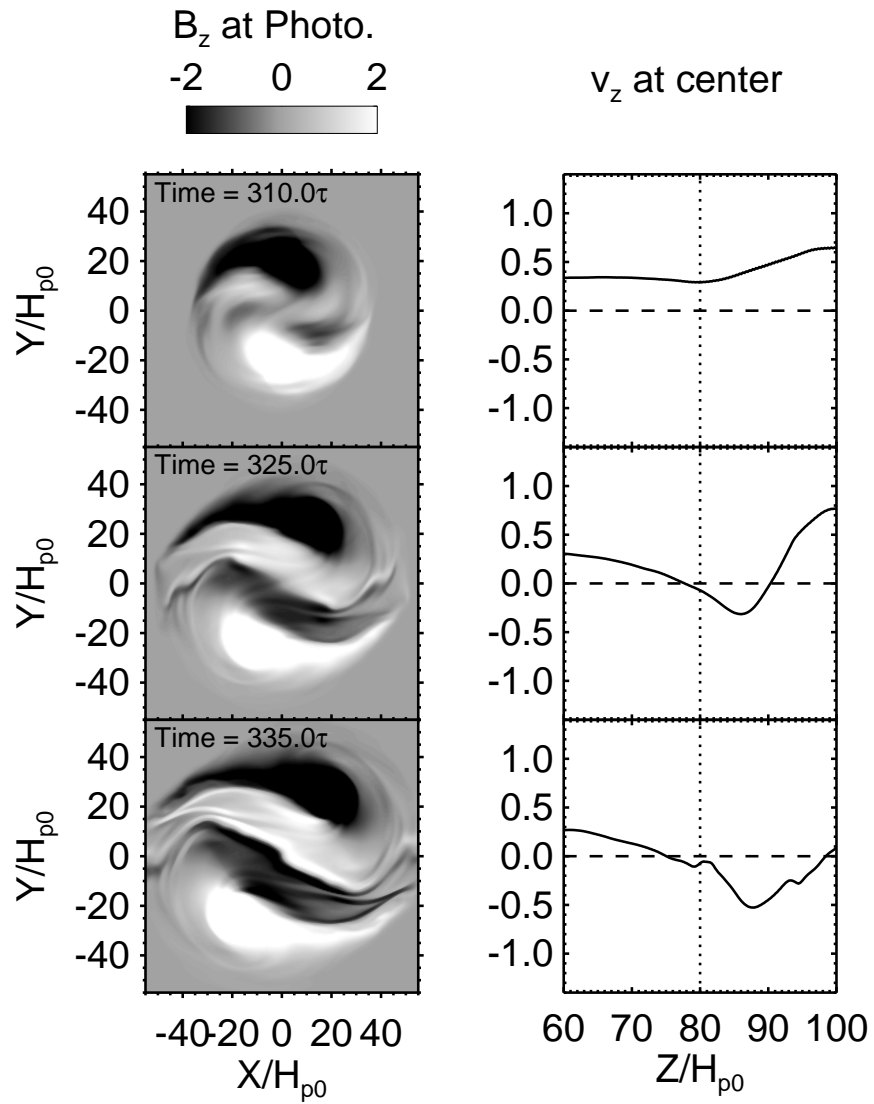


Figure 2.6: Time evolution of the photospheric ($z = 80H_{p0}$) line-of-sight magnetic field B_z (Left) and the vertical velocity component v_z measured at the center $(x, y) = (0, 0)$ (Right). In the right panels, the horizontal dashed lines denote the $v_z = 0$, and the vertical dotted lines indicate the photospheric height. Note that the sinking motion is seen when the middle pair is formed.

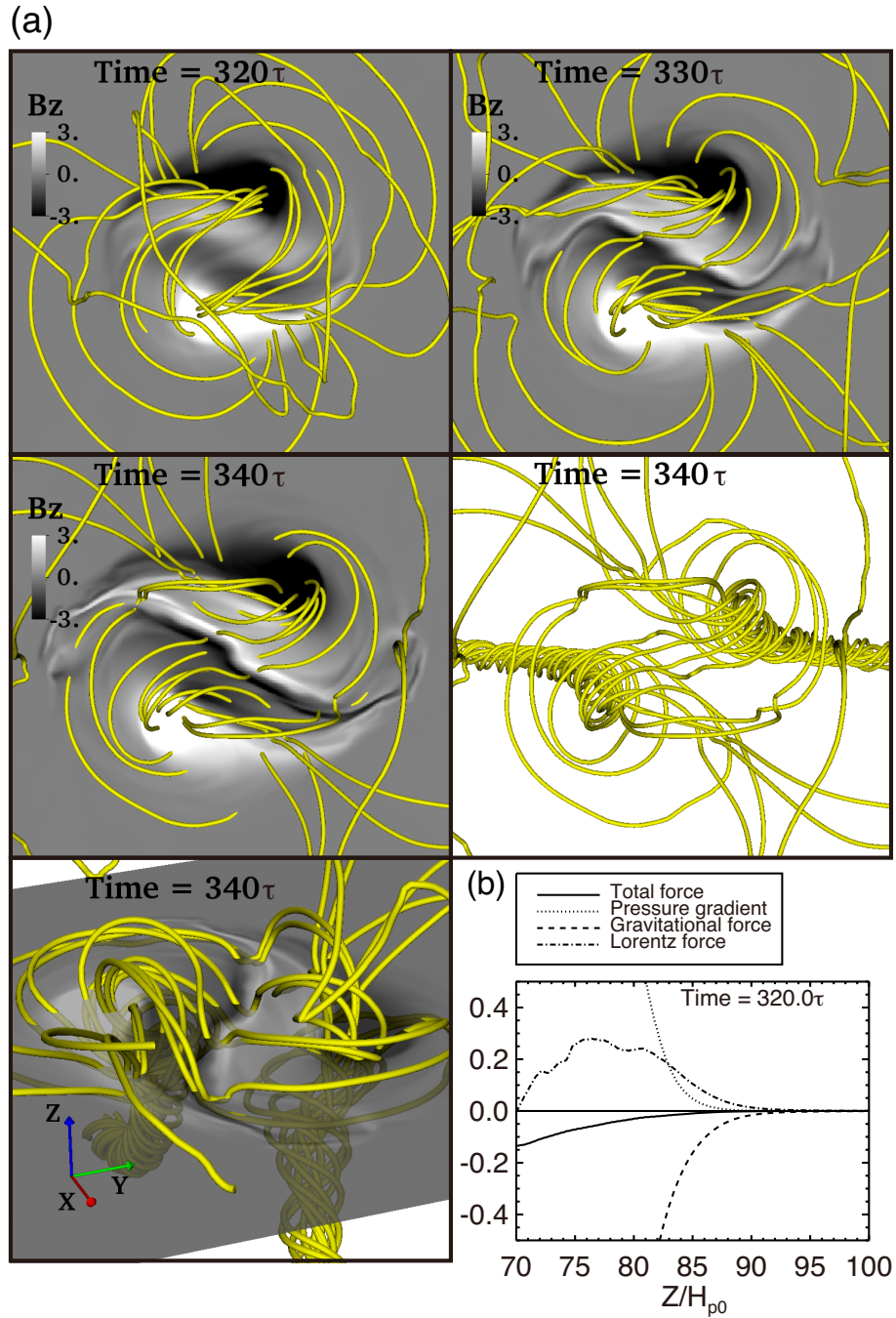


Figure 2.7: Formation of the middle pair. (a) Temporal evolution of the 3D magnetic field (solid lines) and magnetogram B_z . The last two panels shows the magnetic structure below the photosphere and the dip of emerged magnetic fields at the time $t = 340\tau$. (b) Profiles of the vertical forces measured at the center $(x, y) = (0, 0)$. The total force (solid), pressure gradient force (dotted), gravitational force (dashed), and Lorentz force (dashed-dotted) are shown. Note that the sign of the total vertical force is negative near the photosphere, meaning that the downward gravitational force is the most dominant force.

heavy layer is driven to accumulate plasma at a central dip (see Figure 2.8 panels d and e). The continued plasma accumulation results in the submergence of the heavy plasma at the dip and the formation of the two adjacent magnetic arcades.

A snapshot of the 3D coronal magnetic structure is shown in Figure 2.9. The current sheet indicated in Figure 2.8 (c) is located between the blue and yellow magnetic arcades, where magnetic reconnection takes place. Two sets of the new loops colored purple and white are interpreted as reconnected field lines (Figure 2.9 (a-d)). Looking at the reconnection site, we see the reconnection angle (the angle between the merging field lines) is not 180 degree (i.e. not perfectly antiparallel), and merging field lines have a large guide field (panel (e)). As shown in Figure 2.9(d) and (f), the lower new arcade (purple lines) is almost parallel to the polarity inversion line, and is connected to the middle pair. The upper new arcade (white lines), which was ejected upward from the reconnection site, connects the far ends of the two magnetic arcades (yellow and blue).

We also note the magnetic connectivity above the photosphere shown in Figure 2.9. A fraction of the magnetic field of the main spots is connected to the middle pair. The other magnetic field connects the two main spots. A portion of the magnetic field connecting the main spots is the reconnected field (white lines in Figure 2.9).

We have seen that in Figure 2.9, both the yellow and blue arcades on two sides of the polarity inversion line (PIL) as well as the (purple) reconnected loops connecting the middle pair are highly sheared along the PIL of the middle pair. When we look at the photospheric motion, we find the vortical or rotational motion within each of the two main polarities (Figure 2.10 (a)). Figure 2.10 (b) shows the temporal evolution of the vertical vorticity ω_z averaged over the area where $|B_z|$ is above 75% of the peak $|B_z|$ value. From the figure, we find that the counterclockwise vortical motion becomes prominent at time $t \sim 320\tau$, and persists throughout the subsequent evolution. To illustrate the development of magnetic shear, we show the temporal evolution of the vector magnetogram of the middle pair at the photosphere and middle chromosphere in Figure 2.11. We can clearly observe that the horizontal magnetic field becomes more parallel to the PIL at those heights as time progresses. Note that the horizontal magnetic field strength is small just on the PIL. This is because the middle pair is formed as a result of the submergence, not the emergence. As investigated by Fan [2009], the vortical motion (and the horizontal motion) of the main polarities builds-up magnetic shear in this simulation. We also note that the magnetic shear near the PIL is not due to the direct emergence of a sheared field.

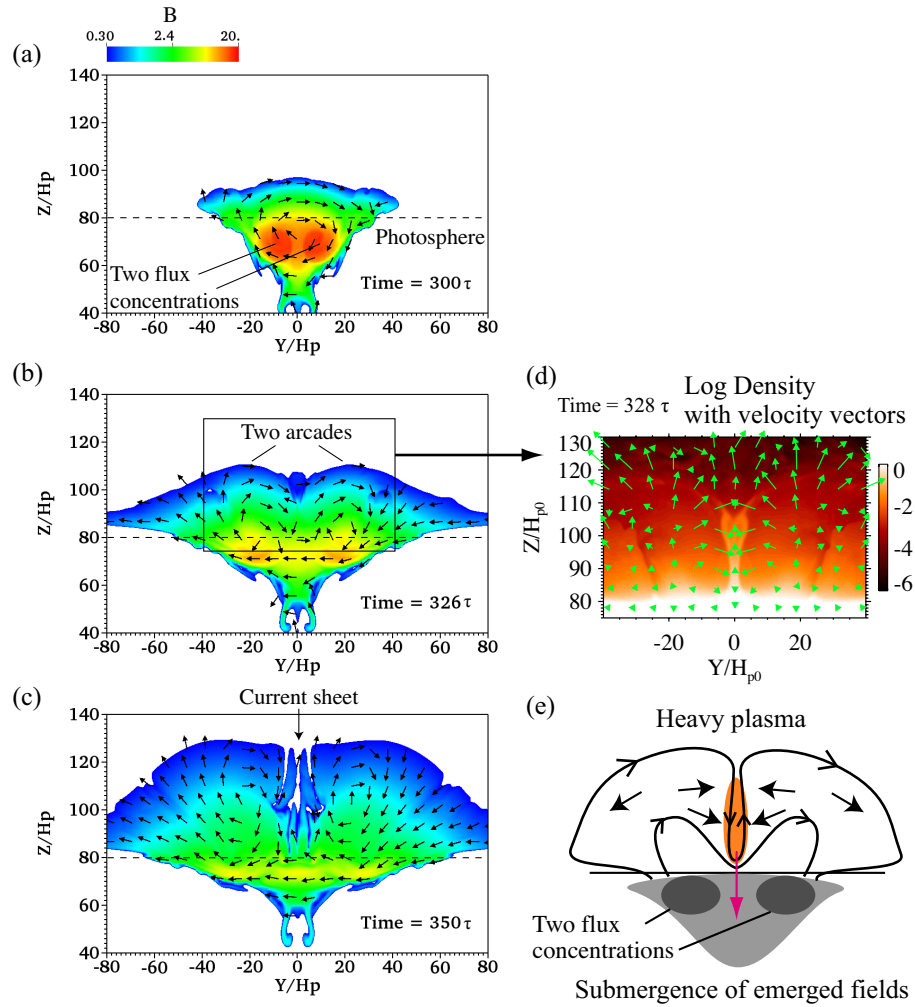


Figure 2.8: (a-c): Time sequence of the magnetic field distribution on the y - z plane at $x = 0$. The arrows denote the direction of the magnetic field projected onto this plane (note that the size of the arrows does not represent the magnetic field strength). (d): The density distribution with velocity vectors on this plane. A high-density region is formed between the two arcades. (e): A schematic diagram to describe the submergence process. Plasma is accumulated in the middle of this region, and the heavy portion of the emerged fields submerges.

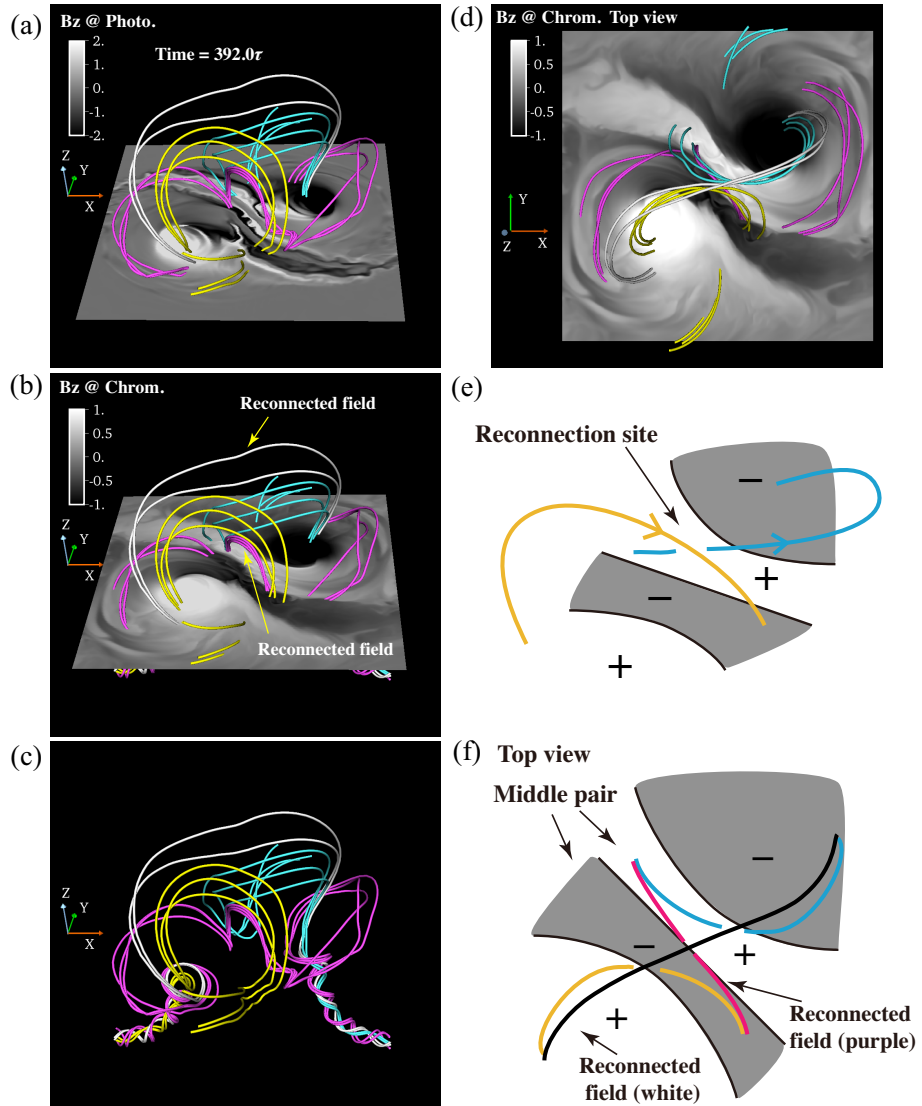


Figure 2.9: 3D Magnetic structure and photospheric and chromospheric line-of-sight magnetic fields B_z at the time 392τ . The yellow and blue field lines denote field lines passing by the current sheet between the two arcades. The white field lines denote field lines enveloping the two arcades. The purple and white field lines denote field lines created by reconnection between the blue and yellow magnetic loops. (a-c): Bird's eye view. (d): Top view. (e): A schematic diagram of the merging field lines. (f): A schematic diagram of the magnetic field structure shown in the panel (d). Note that the purple reconnected field lines are almost parallel to the neutral line at the middle.

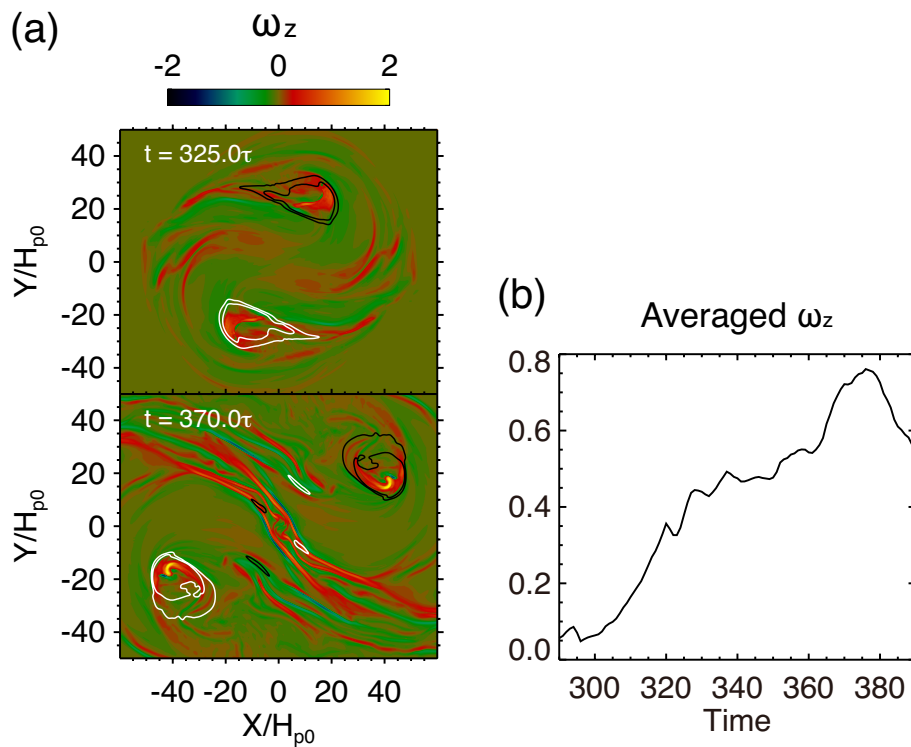


Figure 2.10: (a) Snapshots of the z -component of the vorticity ω_z at the photospheric level. White and black contours denote positive ($3B_0, 4B_0$) and negative ($-4B_0, -3B_0$) B_z , respectively. Note that the main polarities show counterclockwise motion. (b) Temporal evolution of the averaged ω_z over the area where $|B_z|$ is above 75% of the peak $|B_z|$.

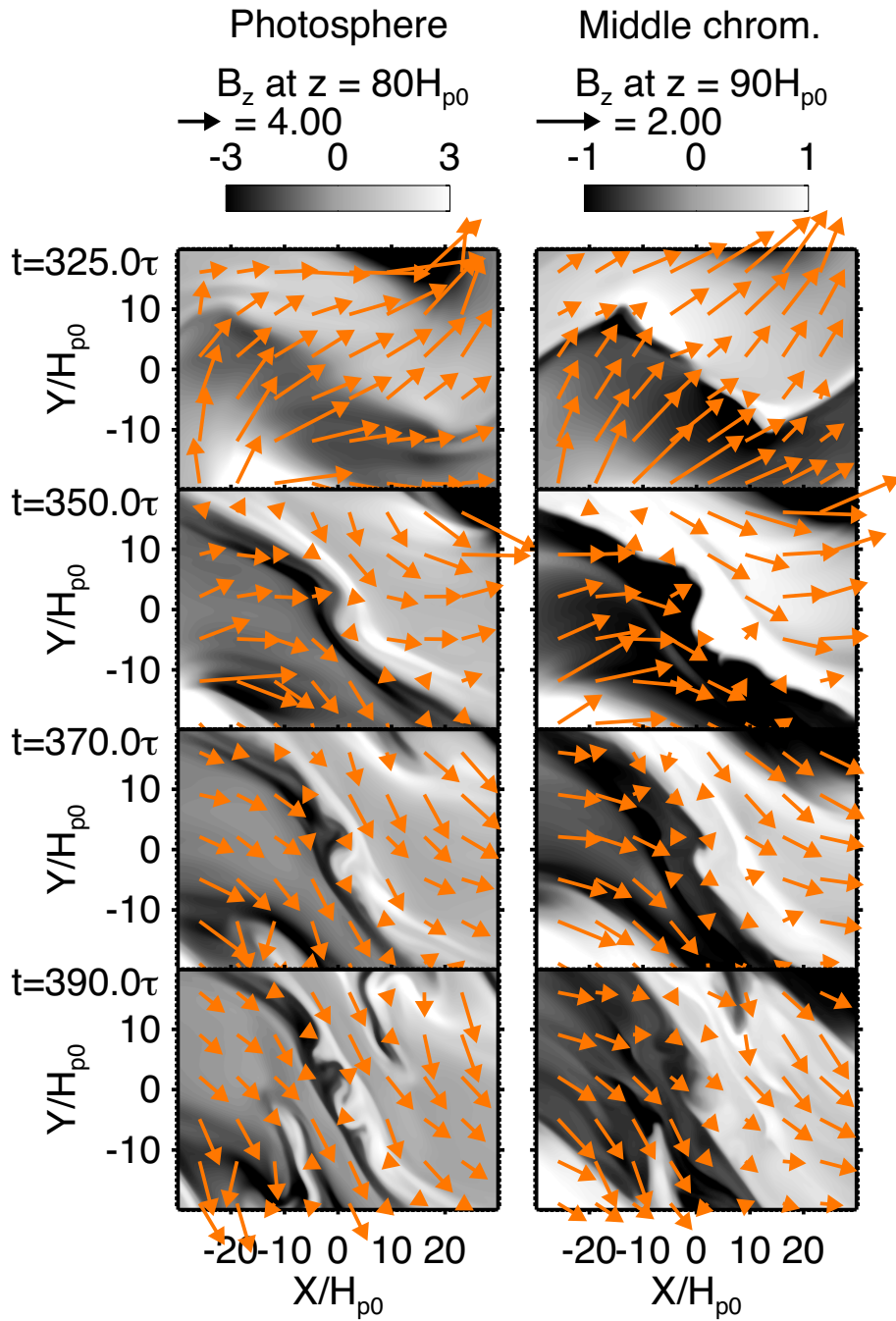


Figure 2.11: Temporal evolution of the vector magnetogram of the photosphere and middle chromosphere. Arrows show the horizontal magnetic field vectors. The horizontal magnetic field becomes more parallel to the polarity inversion line (PIL) at those heights as time progresses. Note that the horizontal magnetic field strength is small on the PIL. See also Figure 2.10 as for magnetic shear development).

2.4.4 Magnetic and Flow Structures in and near Middle Pair

The middle pair is pushed and confined in a narrow region after the formation (Figure 2.4). To understand the confinement mechanism, we looked at the flow structure and the Lorentz force at the photosphere. The top panel of Figure 2.12 shows horizontal velocity vector on the magnetogram, and we can see the converging flow to the PIL. This converging flow is a natural consequence of the development (expansion) of the two magnetic arcades. The bottom panel of Figure 2.12 displays the Lorentz force vector, and we can find that the horizontal Lorentz force is pushing the two polarities together. We checked the pressure balance across the PIL of the middle pair. Figure 2.13 displays the profiles of the total pressure, gas pressure, magnetic pressure, and dynamic pressure across the PIL. The total pressure is almost constant across the PIL, which will explain the persistent existence of the middle pair. We can see that the high gas pressure region is supported by the magnetic pressure. We also found that the magnetic pressure has its peaks at the edges of the high pressure region because of the dynamic pressure of the converging flows.

The horizontal magnetic field is important for producing the large magnetic pressure near the PIL. As shown in Figure 2.10, the main polarities show the vortical motion to shear the field. Figure 2.14 (a) displays the development of the horizontal field along the PIL (see also Figure 2.11). Figure 2.14 (b) shows the ratio of the horizontal field $B_h = \sqrt{B_x^2 + B_y^2}$ to the vertical magnetic field B_z . It is found that the horizontal field is much stronger than the vertical field outside the middle pair and the PIL is sandwiched in the strong horizontal field regions. Therefore, the development of the magnetic shear along the PIL by the vortical motion of the main polarities is a key to confine the narrow middle pair.

We also found persistent fast shear flows along the PIL (see the top panel of Figure 2.12). The maximum velocity is about $2C_{s0}$, which is supersonic at the photospheric level. To understand the driving mechanism, we investigated the acceleration by the Lorentz force and the pressure gradient force. Considering that the PIL is roughly straight and almost parallel to the unit vector $\hat{e} = (-1/\sqrt{2}, 1/\sqrt{2})$, we made the dot products of the two force vectors and this unit vector to see the acceleration in the direction of the PIL: $f_{L,PIL} \equiv (\mathbf{J} \times \mathbf{B}) \cdot \hat{e}$ and $f_{P,PIL} \equiv (-\nabla p) \cdot \hat{e}$, respectively. Figure 2.15 displays the relation between the two forces and horizontal flows. The color indicates $f_{L,PIL}$ (Top) and $f_{P,PIL}$ (Bottom). Note that positive (negative) $f_{L,PIL}$ accelerates plasma in the upper-left (lower-right) direction. The same is true for $f_{P,PIL}$. The horizontal velocity vector shows that the converging flows drastically change their

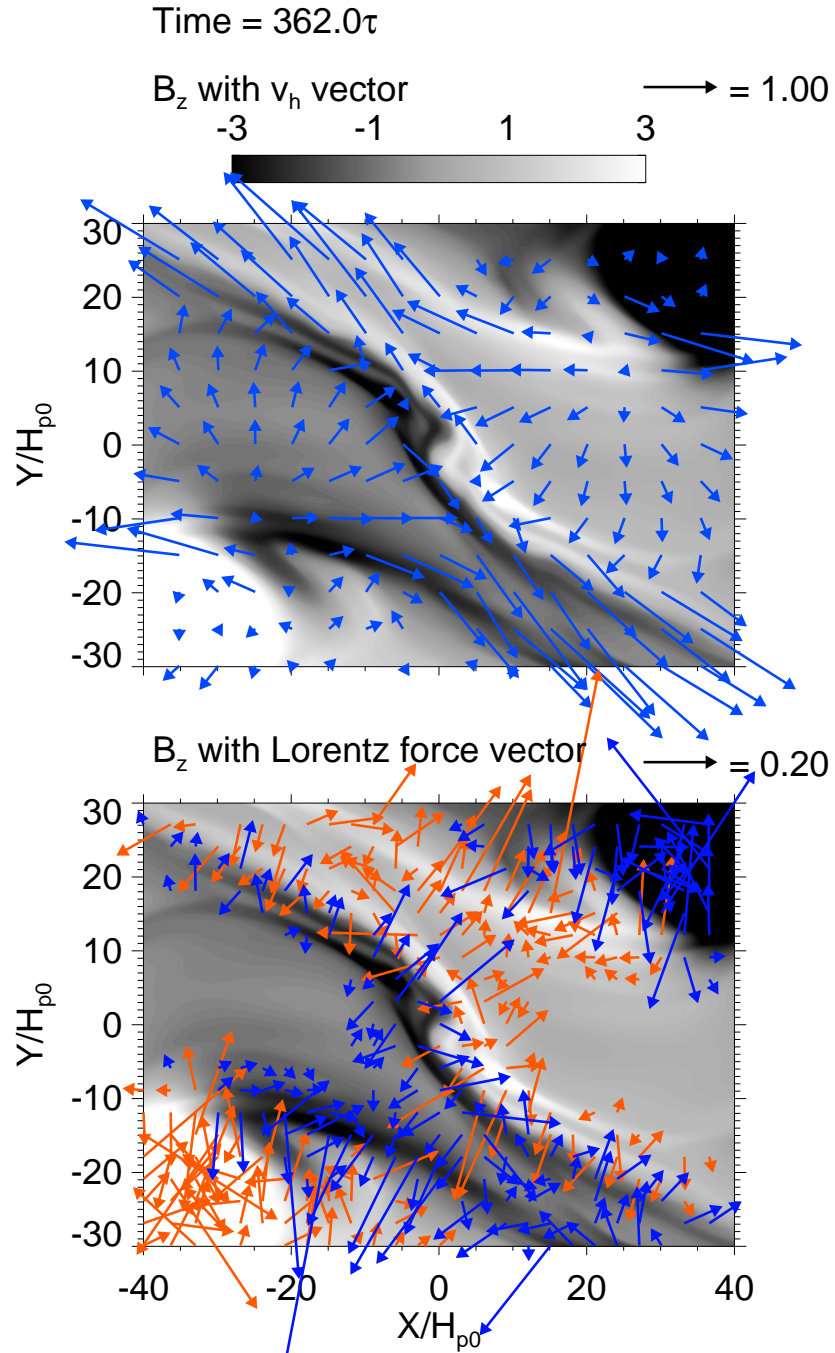


Figure 2.12: Magnetogram (B_z) with horizontal velocity vectors (Top) and with Lorentz force vectors (Bottom) at time $t = 362\tau$. In the bottom panel, red and blue arrows show the Lorentz force in positive and negative polarities, respectively. The velocity and Lorentz force are normalized by C_{s0} and B_0^2/H_{p0} , respectively.

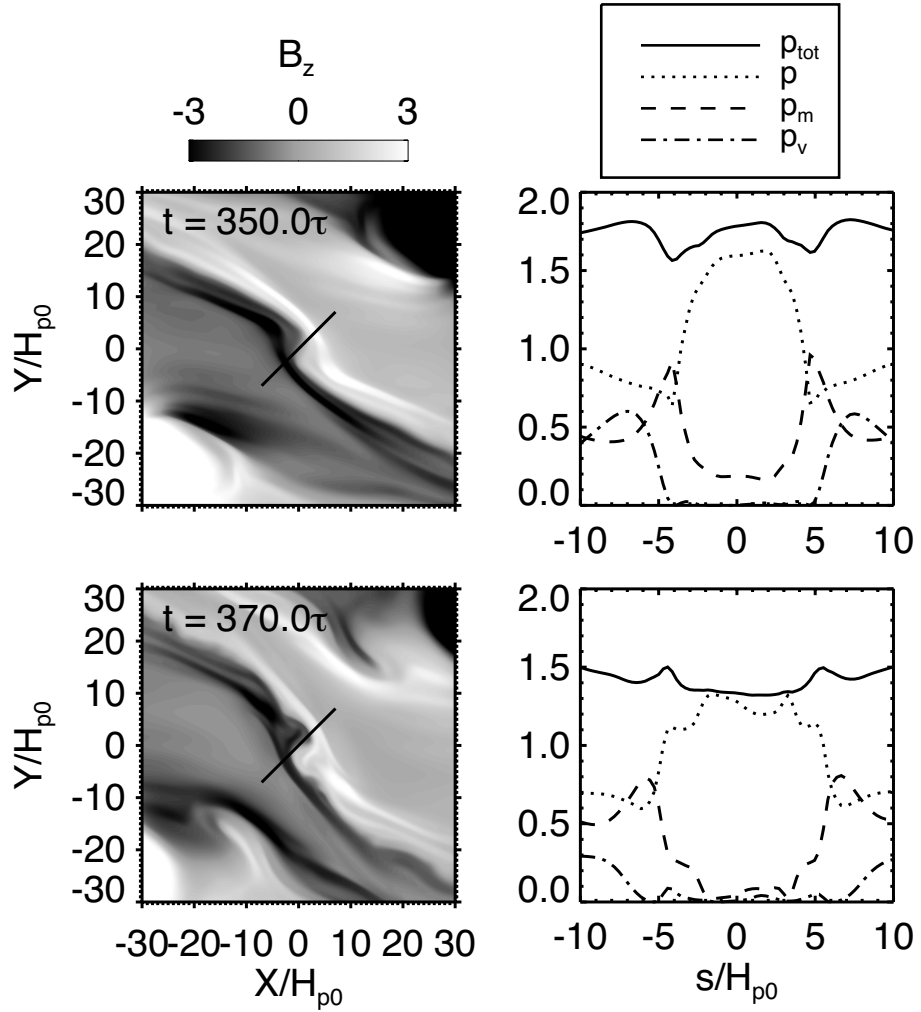


Figure 2.13: Profiles of the total pressure p_{tot} (solid), gas pressure p (dotted), magnetic pressure p_m (dashed), and dynamic pressure p_v (dashed-dotted) across the polarity inversion line of the middle pair. The profiles are measured along the slit shown in the B_z maps. The velocity component parallel to the slit is used to calculate p_v .

direction to the direction of the PIL at the edges of the middle pair. From the figure, it is found that the shear flows along the PIL are driven by the Lorentz force. The pressure gradient force has no significant contribution (this implies that the hydrodynamic baroclinic vorticity generation $(-\nabla(1/\rho) \times \nabla p)$ can be neglected). The acceleration regions coincide with the strong magnetic pressure regions at the edges of the middle pair, where the plasma β is less than unity (see Figure 2.13). The direction of the shear flow is determined by the expansion of each magnetic arcade: the magnetic arcade with the positive (negative) main polarity drives the shear flows in the positive (negative) x -direction.

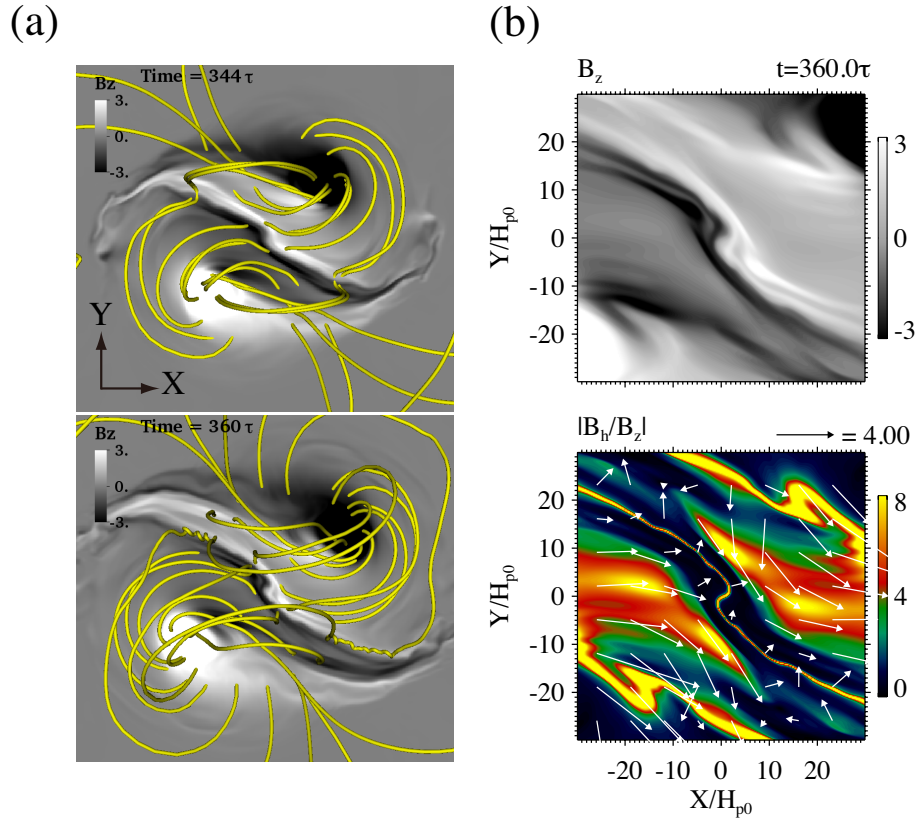


Figure 2.14: Development of the horizontal magnetic field just near the polarity inversion line of the middle pair. (a) Snapshots of 3D magnetic field lines with magnetogram. (b) Enlarged images of the magnetogram B_z and the ratio $|B_h/B_z|$ of the middle pair. The arrows indicate the horizontal magnetic field vector $\mathbf{B}_h = (B_x, B_y)$.

We briefly compare our simulation with an observational example of δ -spot regions. We focus on Active Region NOAA 11429 that was one of the most violent δ -spot regions

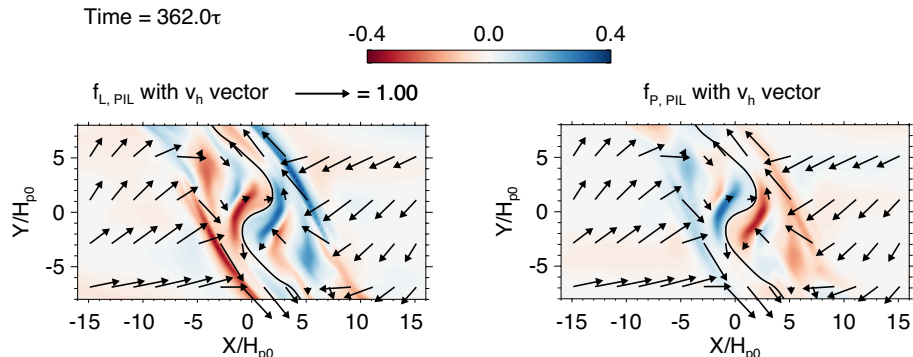


Figure 2.15: The Lorentz force drives flows along the polarity inversion line (PIL) of the middle pair. The color indicates $f_{L,PIL} = (\mathbf{J} \times \mathbf{B}) \cdot \hat{\mathbf{e}}$ (Left) and $f_{P,PIL} = (-\nabla p) \cdot \hat{\mathbf{e}}$ (Right), where $\hat{\mathbf{e}} = (-1/\sqrt{2}, 1/\sqrt{2})$ is a unit vector almost parallel to the PIL. Note that positive (negative) $f_{L,PIL}$ accelerates plasma in the upper-left (lower-right) direction. The same is true for $f_{P,PIL}$. The arrows denote the horizontal velocity, and the solid lines indicate the PIL ($B_z = 0$). The velocity is normalized by C_{s0} .

in the solar cycle 24. The δ -spot region appeared in March 2012, and produced three X-class flares. Because of the high activity, it has been drawing many authors' attention [Petrie, 2012; Shimizu et al., 2014]. Figure 2.16 displays snapshots of the active regions and snapshots of the magnetogram obtained from our simulation (note that the sign of B_z of the magnetogram from the simulation is reversed just for better comparison). The continuum and magnetogram images were taken by the Helioseismic and Magnetic Imager (HMI: Schou et al. [2012]) on board the Solar Dynamics Observatory. The active region appeared in the northern hemisphere, and did not follow the Joy's Law. The mean force-free parameter $\langle \alpha \rangle$ of this region calculated in SHARP (Spaceweather HMI Active Region Patch) data was negative, which means that the region obeyed the helicity hemispheric rule. This is consistent with the apparent magnetic structure: the largest positive and negative spots show a left-handed twist. Our simulation reproduced some observed features of this δ -spot region. The observed δ -spot region has a narrow complex polarity pair between the main polarities (indicated by the arrow in the figure), and therefore it had a complex quadrupole structure. In addition, the middle pair appeared after the emergence of the main polarities. These observed features are also found in our simulation.

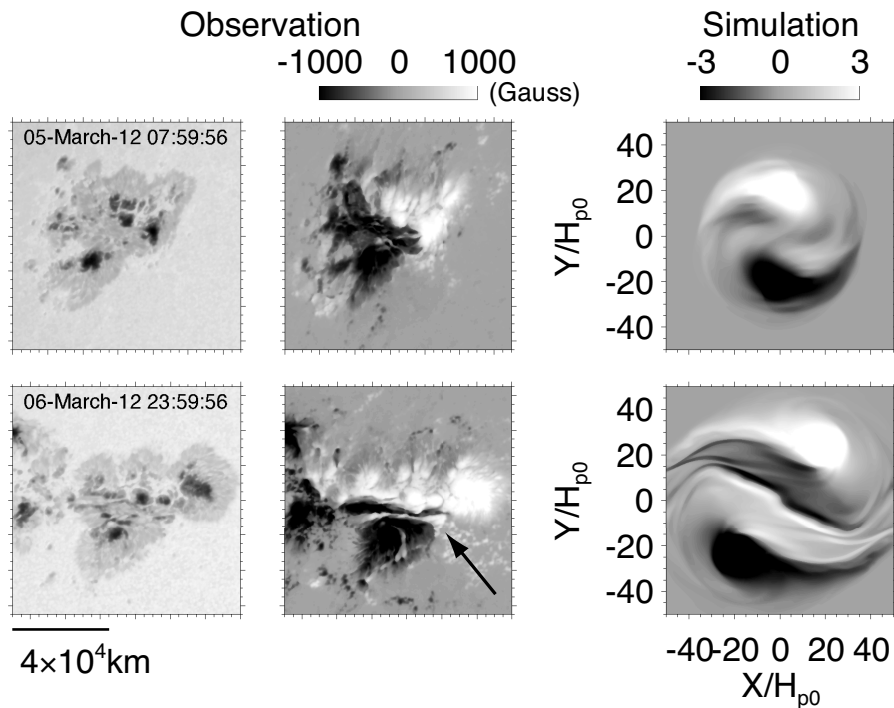


Figure 2.16: Comparison of the δ -spot region NOAA 11429 and our simulation. The left and middle panels show the continuum and magnetogram images. The middle polarity pair between the largest opposite polarities is indicated by the arrow. The right panels show the snapshots of the magnetogram from our simulation at the time $t = 310\tau$ and 335τ . Note that the sign of B_z of the magnetogram from the simulation is reversed just for better comparison. This does not change its twist handedness.

2.5 Discussion

We have examined the evolution of the emergence of a kinked flux tube from the interior of the Sun to the corona using a 3D MHD simulation: we studied the rising of the kinked tube in the interior, emergence into the corona, and evolution of the coronal magnetic field. On the basis of the results, we discuss the kinked tube emergence scenario as a possible origin of the δ -spot regions.

From the simulation, unlike the previous expectations based on the bodily emergence of a knotted tube [Fan et al., 1999; Linton et al., 1999], we found that the kinked tube can naturally form a complex quadrupole structure at the photospheric level. The appearance of the complex quadrupole structure has not been pointed out by the previous studies. This simulation is of much higher resolution compared to the previous study [Matsumoto et al., 1998], and therefore we could find the development of the middle pair and the quadrupole morphology. The main magnetic polarities appeared first, and later another pair of magnetic polarities is formed between it as a result of the submergence of emerged magnetic fields. This leads to the formation of a quadrupole structure and two coronal magnetic arcades.

Owing to the emergence of the two strong flux concentrations formed just below the photosphere, and the comparatively weaker twist at the middle between the two concentrations, the top heavy layer above the emerging fields is driven to accumulate plasma at a central dip, which results in the submergence of the heavy plasma and the formation of the quadrupole structure. A schematic diagram of the formation of a quadrupole photospheric structure and the two-arcade system is illustrated in Figure 2.17. The kinking of the tube reduces the magnetic twist of the tube at the apex, and the magnetic field at the apex becomes more unidirectional (see the top panel of Figure 2.17 and Figure 2.7). As a result, the magnetic tension force to retain the coherency of the flux bundle decreases locally. Owing to the small tension force, the horizontal expansion of the apex of the tube is promoted. The magnetic field strength and the upward Lorentz force becomes weaker, causing the submergence of emerged fields. The bottom panel of the figure describes the flux emergence in the y - z plane. The two flux concentrations on this plane are formed by the kinking of the axis (they correspond to the two parent flux tubes of the main spots). Two arcades develop from the two flux concentrations with a portion of the emerged fields undergoing submergence, which leads to the formation of a current sheet between them (see also Figure 2.8 and 2.9). Finally magnetic reconnection takes place there to form a sheared magnetic arcade above the polarity inversion line.

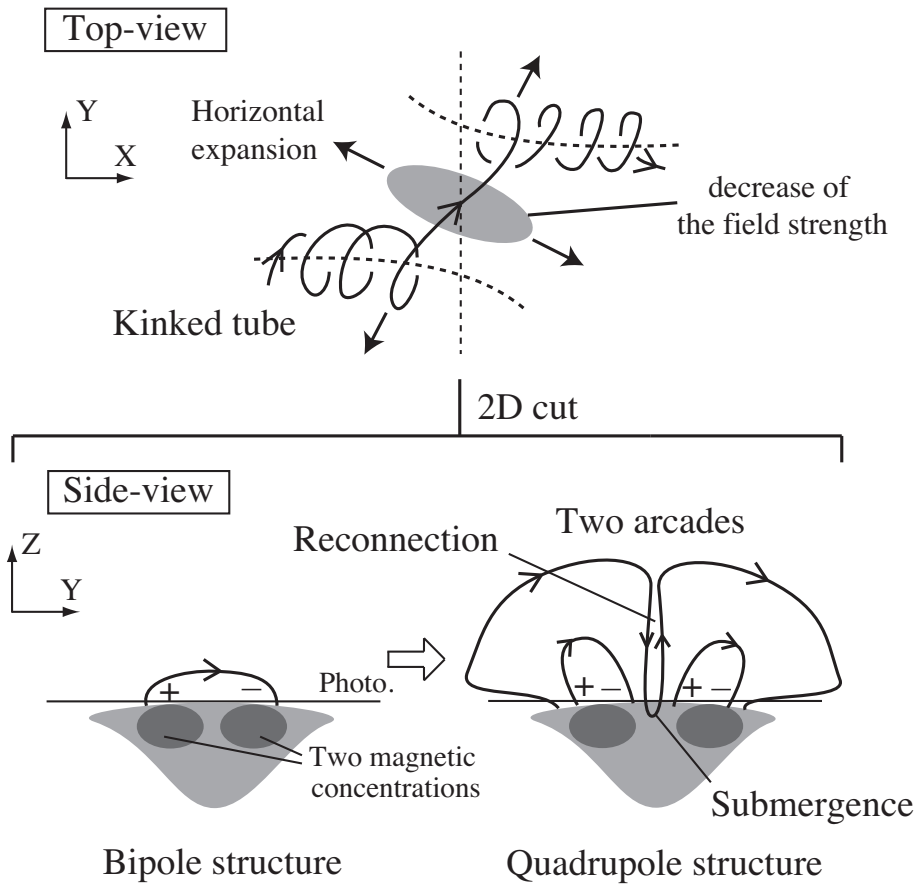


Figure 2.17: Schematic diagram of the formation of a quadrupole photospheric structure. Top: the horizontal expansion of the kinked flux tube before the emergence. See also Figure 2.2 and 2.7. Bottom: 2D cut view of the expanding two magnetic arcades. The two magnetic concentrations below the photosphere correspond to the two parent flux tubes. The plus and minus signs denote the positive and negative polarities at the photosphere, respectively. See also Figure 2.8 and 2.9.

The kinked part, which is the most buoyant part, is subject to the kinking and strong horizontal expansion. As a result, the twist and field strength are largely reduced. This means that some of the free magnetic energy of this segment is already released before the emergence. However, the twist and field strength of the parent flux tubes remain strong, which means that a large amount of the free energy is stored there. The free energy is injected in the form of the vortical motion of the main polarities after the emergence, and the less-sheared coronal field is twisted up eventually (Figure 2.10, 2.11, and 2.14). Also, the highly nonuniform distribution of the twist and field strength along the tube will explain that the middle pair has the less-coherent photospheric structure and the main pair has a strong twist with a coherent structure.

Fan et al. [1999] and Linton et al. [1999] speculated the origin of the sheared field above a polarity inversion line (PIL) by simply taking horizontal cuts of the kinked tubes approaching the surface, and argued that the shear can be introduced by the kinking of a tube. In this study, on the contrary, the magnetic shear along the PIL is weak in the early phase of the emergence, which means that the direct emergence does not provide a strong sheared field above the photosphere. The strong magnetic shear is built-up by the vortical motion of the main polarities.

As another possible origin of δ -spot regions, Toriumi et al. [2014] and Fang and Fan [2015] proposed a simple scenario in which a single twisted flux tube with two buoyant segments emerges (here we refer their model as the “multi buoyant segment model, MBS model”). It was found that this model successfully accounts for many observational characteristics of the active region with a quadrupole structure NOAA 11158. Here we compare the kinked tube model (KT model) and their MBS model. In both models, a quadrupole photospheric structure can be formed, and the middle pair is locked by the Lorentz force. In addition, the middle pair in both models are magnetically connected below the surface. However, we see a difference in the photospheric structure between the two models. The middle pair found in KT model shows a narrow and incoherent structure, but every spot in the quadrupole found in MBS model can have a coherent structure. In KT model, we found the flux imbalance between the main pair and the middle pair. However, the flux imbalance in MBS model is less prominent. Photospheric polarity motion and magnetic reconnection are important to form a sheared field on and near the PIL in both models. The magnetic shear in KT model is introduced mainly by the vortical motion of the main polarities. The shear in MBS model is introduced by the stretching of the reconnected field by the horizontal spot motion.

We observe supersonic shear flows along the PIL of the middle pair. We identified that the driving force is the Lorentz force, as found in previous studies [Fan, 2001;

[Manchester, 2001](#)]. The flows are driven by the Lorentz force at the edges of the middle pair, where the plasma β is less than unity. The strong magnetic field at the edges is resulted from the squeezing by the high gas pressure and the dynamic pressure of the converging flows. The converging flows are driven by the expansion of two magnetic arcades, and the direction of the shear flow is also determined by the expansion. Therefore, the generation of the shear flows is a direct consequence of the development of the two arcades.

We briefly compared our simulation with a δ -spot region NOAA 11429, and found similarities in the behavior of the photospheric magnetic structures. The δ -spot region has a narrow complex polarity pair between the main polarities. In addition, the middle pair appeared after the emergence of the main polarities. On the basis of our simulation, we expect that the spots in the δ -spot region are magnetically connected below the photosphere, which is important for keeping δ -spot regions compact. We note that we have to be careful to compare our simulations to observations: the total amount of the magnetic flux of a main spot is only 3×10^{20} Mx (smaller than a typical value, $\sim 10^{22}$ Mx), and the convection and radiative cooling are not included. Because of the lack of the radiative cooling, the penumbra that is important to define the δ -spot regions cannot be formed in the simulation. In this study, we hypothesize that the polarities of the middle pair is locked closely enough to be surrounded by a common penumbra. To confirm the speculation, more realistic simulations and detailed comparison with observations are necessary.

[Takizawa and Kitai \[2015\]](#) performed a statistical study, and found that flare-productive δ -spot regions tend to have a quadrupole structure and are likely to be formed by the emergence of a singly connected structure. In addition, they clarified that the flare activity is highly correlated with the magnetic complexity. Our simulation showed the formation of a complex quadruple structure from a single flux tube. Considering this, we conjecture that our results may give a general picture of the formation of the highly flare-productive δ -spot regions.

It has been argued that magnetic reconnection between sheared fields is important for the onset of solar flares [e.g. [Moore et al., 2001](#)]. It has been also discussed that a quadrupole structure is preferable for the filament eruption [e.g. [Antiochos et al., 1999](#); [Hirose et al., 2001](#); [Yurchyshyn et al., 2006](#)]. Our simulation shows that the coronal magnetic structure changes its topology via reconnection between sheared arcades in a quadrupole region, although the formation and eruption of a flux rope was not achieved probably due to a short-term calculation in a smaller domain size than the size of a real active region [Figure 2.9]. We note the similarity between the reconnection in our

Figure 2.9 and the reconnection in Figure 1 of [Moore et al., 2001](#)]. Considering this, our results could be relevant for understanding how the formation of δ -spot regions with a quadrupole structure can lead to the onset of solar flares. For comprehensive understanding including the onset of flares, it is necessary to perform longer-term calculations in a larger calculation domain size.

Chapter 3

MHD Shocks in and above Flare Loops: Two-dimensional Simulation and a Simplified Model

3.1 Introduction

In this chapter, the evolution of flare loops will be investigated in detail using MHD simulations.

There are many attempts to model solar and stellar flare loops. One-dimensional (1D) hydrodynamic models have been widely developed to study the thermal evolution and flows in a single loop. Depending on the assumed main energy transfer process, the models can be categorized into two branches: conduction-heating models [e.g. Nagai, 1980; Peres and Reale, 1993] and electron-beam-heating models [e.g. Fisher et al., 1985; Mariska et al., 1989]. Hori et al. [1997, 1998] developed a pseudo-2D loop model based on 1D hydrodynamic calculations, and gave a simple description of observed soft X-ray emissions (see Warren [2006] for further development of this kind of models).

The first 2D magnetohydrodynamic (MHD) simulation of a solar flare based on a reconnection model with the heat conduction was performed by Yokoyama and Shibata [2001], and they studied the thermal evolution in the flare loops and the physics that determines the flare temperature. Shiota et al. [2005] performed MHD simulations of reconnection with the heat conduction to study the coronal mass ejections

and associated giant arcade, where they do not include the chromosphere. [Miyagoshi and Yokoyama \[2004\]](#) carried out a MHD simulation of chromospheric evaporation jets formed as a result of reconnection between emerging magnetic flux and a coronal ambient field. Recently [Longcope et al. \[2009\]](#) and [Longcope \[2014\]](#) developed a theoretical model in which the dynamics of a reconnected field line is considered.

Shocks in and above the flare loops can be important for both the non-thermal particle acceleration and evolution of the thermal structure. The above-the-loop-top hard X-ray source found by [Masuda et al. \[1995\]](#) has posed problems about the electron acceleration mechanism (for recent progress, see e.g. [Krucker et al. \[2010\]](#) and [Oka et al. \[2015\]](#)). One of the promising scenarios is the acceleration by fast shocks which are expected to be formed above the soft X-ray flare loops [[Somov and Kosugi, 1997](#); [Tanuma and Shibata, 2005](#); [Tsuneta and Naito, 1998](#)]. Recently, acceleration from contracting plasmoids [[Drake et al., 2006](#)] and acceleration in plasmoids interacting with fast shocks [[Nishizuka and Shibata, 2013](#)] have been also proposed. It has been argued that a high-density region can be formed as a result of the shock-shock interaction at the top [[Hori et al., 1997](#)] and by the compression at termination shocks [[Yokoyama and Shibata, 2001](#)]. [Zenitani and Miyoshi \[2011\]](#) analyzed shocks in a plasmoid in a ideal 2D MHD simulation. Despite the importance, the shock formation in and above the flare loops has not been yet investigated in detail.

How flare loops evolve is one of our central interests. Since reconnection can produce hot and supersonic plasma flows in a low β plasma, the thermal structure will be determined by a coupling among the plasma flows, shocks, and heat conduction. The heat conduction is essential to drive the hot high-speed evaporation flows. However, the calculation of the plasma dynamics with the heat conduction effects is computationally expensive. This makes the extensive parameter survey in the multi-dimensional MHD simulations difficult. The development of a simplified flare loop model based on a reconnection model is therefore desired.

In this chapter, we study the shock formation and evolution of the thermal structure in and above the flare loops using MHD simulations. To understand the shock formation in 2D systems, a 2D MHD simulation of a solar flare has been carried out. We found new shock structures in and above the flare loops, which were not well resolved in the previous work by [Yokoyama and Shibata \[2001\]](#). To study the dynamics of flows along the reconnected magnetic field in detail, kinematics and energetics of the plasma are investigated along selected field lines. It is found that shocks in the flare loops are crucial to determine the thermal and flow structures in the flare loops. On the basis of the results of the 2D MHD simulation, we have developed a new flare loop model which

we call the pseudo-2D MHD model. The model is based on the 1D MHD equations, and has been developed to model a 3D reconnected field line. Through a comparison, it is found that the shock formation and thermal evolution in the pseudo-2D MHD model are similar to those in the 2D MHD model.

This chapter is structured as follows. In Section 3.2, the 2D MHD model of a solar flare is introduced. In Section 3.3, numerical results of the 2D MHD simulation are detailed. In Section 3.4, on the basis of the 2D MHD simulation, we develop our pseudo-2D MHD model of a flare loop. In Section 3.5, numerical results of the pseudo-2D MHD model are introduced and are compared with the 2D MHD simulation. Section 4.4 contains our summary and discussion.

3.2 2D MHD Model of a Solar Flare

3.2.1 Assumptions and Basic Equations

We performed a 2D MHD simulation of a solar flare similar to [Yokoyama and Shibata \[2001\]](#) simulations. We take a rectangular calculation domain in the x - y plane. The MHD equations in the following form are solved:

$$\frac{\partial \rho}{\partial t} + \nabla \cdot (\rho \mathbf{v}) = 0, \quad (3.1)$$

$$\frac{\partial \rho \mathbf{v}}{\partial t} + \nabla \cdot \left[\rho \mathbf{v} \mathbf{v} + \left(p + \frac{|B|^2}{8\pi} \right) \mathbf{1} - \frac{\mathbf{B}\mathbf{B}}{4\pi} \right] = 0, \quad (3.2)$$

$$\frac{\partial \mathbf{B}}{\partial t} + c \nabla \times \mathbf{E} = 0, \quad (3.3)$$

$$\frac{\partial e}{\partial t} + \nabla \cdot \left[\mathbf{v} \left(e + p + \frac{|B|^2}{8\pi} \right) - \frac{1}{4\pi} \mathbf{B}(\mathbf{v} \cdot \mathbf{B}) + \frac{c\eta}{4\pi} \mathbf{J} \times \mathbf{B} + \mathbf{F}_c \right] = 0, \quad (3.4)$$

$$\mathbf{F}_c = -\kappa_0 T^{5/2} \nabla_{\parallel} T, \quad (3.5)$$

$$p = \frac{k_B}{m} \rho T, \quad (3.6)$$

$$\mathbf{E} = \eta \mathbf{J} - \frac{1}{c} \mathbf{v} \times \mathbf{B}, \quad (3.7)$$

$$e = \frac{p}{\gamma - 1} + \frac{1}{2} \rho \mathbf{v}^2 + \frac{B^2}{8\pi}, \quad (3.8)$$

$$\mathbf{J} = \frac{c}{4\pi} \nabla \times \mathbf{B}, \quad (3.9)$$

where $\mathbf{v} = (v_x, v_y, v_z)$ and $\mathbf{B} = (B_x, B_y, B_z)$. κ_0 ($\sim 10^{-6}$ in cgs units) is the coefficient of the Spitzer-type conductivity, γ is the specific heat ratio (5/3 is used in this study), m is the mean particle mass and k_B is the Boltzmann constant. η is the electric resistivity.

Table 3.1: Normalization units for solar flare simulations

Quantity	Unit	Value
Length	L_0	3,000 km
Velocity	$C_{s0} = [\gamma(k_B/m)T_0]^{1/2}$	170 km s ⁻¹
Time	L_0/C_{s0}	18 s
Temperature	$T_0 = T_{cr}$	2×10^6 K
Density	$\rho_0 = \rho_{cr}$	$(10^9 \text{ cm}^{-3}) \times m$
Pressure	$\gamma(k_B/m)\rho_0 T_0$	0.47 dyn cm ⁻²
Magnetic field strength	$[8\pi\gamma(k_B/m)\rho_0 T_0]^{1/2}$	3.4 G

\mathbf{F}_c is the conduction flux. The normalization units of our simulations are summarized in Table 3.1. The radiative cooling time is expected to be longer than the dynamical time in the flare loops. Since we mainly focus on the dynamical processes such as the shock formation and flows, we neglect the radiative cooling.

3.2.2 Initial and Boundary Conditions

Our model is identical to the [Yokoyama and Shibata \[2001\]](#) model, except for the domain size and boundary conditions. The initial condition is same as their model. The initial and boundary conditions are as follows. The domain is $0 \leq x \leq x_{max,2D}$ and $0 \leq y \leq y_{max,2D}$, where $x_{max,2D}=10$ and $y_{max,2D} = 20$. A schematic diagram of the initial and boundary conditions are shown in Figure 3.1. The initial magnetic field is assumed to be a force-free field and is given by

$$B_x(x, y) = 0, \quad (3.10)$$

$$B_y(x, y) = B_0 \tanh(x/w), \quad (3.11)$$

$$B_z(x, y) = B_0 / \cosh(x/w), \quad (3.12)$$

where $w = 0.5$ is the width of the initial current sheet. The gas pressure is assumed to be uniform (p_0). The density distribution is described as

$$\rho(x, y) = \rho_{chr} + (\rho_{cor} - \rho_{chr}) \frac{1}{2} (\tanh[(y - h_{TR})/w_{TR,2D}] + 1), \quad (3.13)$$

where ρ_{cor} and ρ_{chr} are respectively the densities in the corona and chromosphere, and h_{TR} and $w_{TR,2D}$ are respectively the height and the width of the transition region between the corona and chromosphere. h_{TR} and $w_{TR,2D}$ are set to 1 and 0.2, respectively. The chromosphere is modeled as a dense and cool plasma. For simplicity, in this chapter

ρ_{chr} is set to $10^5 \rho_{cor}$. $T_{cor} = (m/k_B)(p_0/\rho_{cor})$ is the initial coronal temperature.

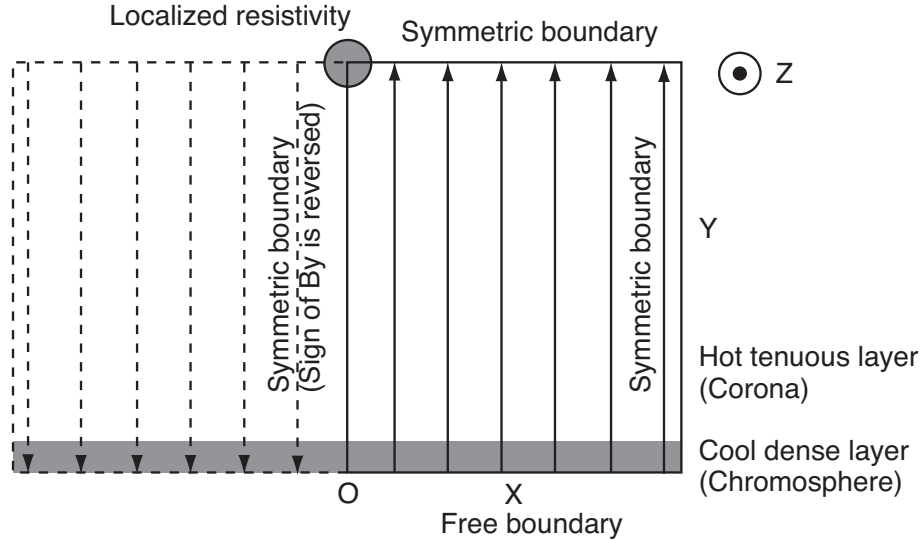


Figure 3.1: Schematic diagram of the initial and boundary conditions of the 2D MHD simulation. The solid arrows denote the magnetic field. The circled region indicate the region where the localized resistivity is applied. The grey region at the bottom is the chromosphere. The calculated domain is the region where $x > 0$.

To allow the magnetic field to reconnect, we impose a localized resistivity in the form of

$$\eta(x, y) = \eta_0 \exp[-(r/w_\eta)^2], \quad (3.14)$$

where $r = \sqrt{x^2 + (y - h_{TR})^2}$ and $w_\eta = 1$. We localize the resistivity and fix it with time to realize a fast and quasi-steady magnetic reconnection with a single X-point [Ugai, 1992].

All the boundaries are symmetric. At the boundary at $x = 0$ the sign of B_y is reversed.

The numerical scheme is based on a Harten-Lax-van Leer (HLL) scheme developed by Miyoshi and Kusano [2005], HLLD ("D" stands for Discontinuities), which is a shock-capturing scheme. It has the second-order accuracy in space and time. The heat conduction term is solved with an implicit method similar to Yokoyama and Shibata [2001] method to reduce the calculation time. We modify their method to more accurately calculate the heat conduction flux. A detailed description of the implicit method is given in Appendix A.2. The calculated domain is resolved with 800×1000 grids.

3.3 Numerical Results of 2D MHD Model

3.3.1 Overview of Evolution

Figure 3.2 displays an overview of the time evolution of the 2D MHD simulation. The region where $x < 0$ is also shown only for visual inspection. Reconnection takes place due to the localized resistivity and the Alfvénic collimated reconnection outflow is produced. The reconnected field lines pile up in the outflow region to form the growing loop system at the base of the corona. The temperature structure is smooth along the magnetic field owing to the heat conduction. The heat in the hot outflow is carried to the chromosphere along the magnetic field due to the heat conduction. As a result, the upper chromosphere is heated up and rapidly expands, leading to the formation of the hot dense upflows called the chromospheric evaporation. The evaporated plasma finally fills the reconnected field lines and forms the hot dense flare loops. We note that the weak disturbance which starts to propagate at the beginning of the simulation is generated because the initial condition is not in the thermal equilibrium between the chromosphere and corona. We confirmed that its effect is negligible for the dynamics of the flare loops.

One-dimensional plots parallel to the x -axis across $y = 10$ (i.e. across the reconnection outflow) are shown in Figure 3.3. It is shown that a Petschek-type reconnection is established because of the localized resistivity, where two slow shocks emanate from the reconnection region. The slow shocks can be discerned as a pair of the discontinuities in Figure 3.3. We note that due to the heat conduction the slow shocks become isothermal slow shocks [Chen et al., 1999; Forbes et al., 1989; Seaton and Forbes, 2009; Yokoyama and Shibata, 1997].

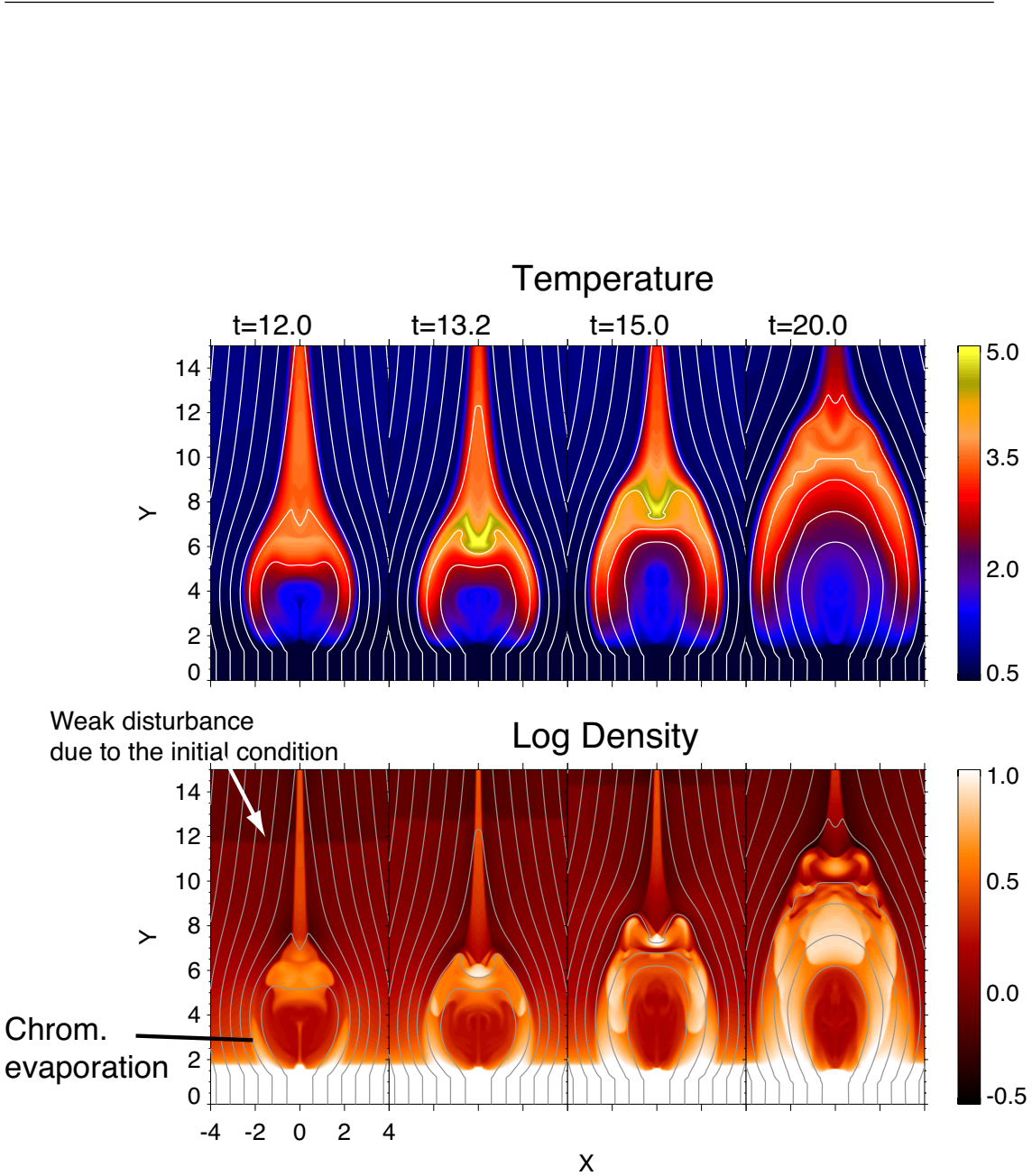


Figure 3.2: Time evolution of the temperature (Top) and density (Bottom) of the 2D MHD model. The solid lines denote the magnetic field.

One-dimensional plots of the reconnection outflow
(2D MHD Model)

Time = 13.0, Y = 10.0

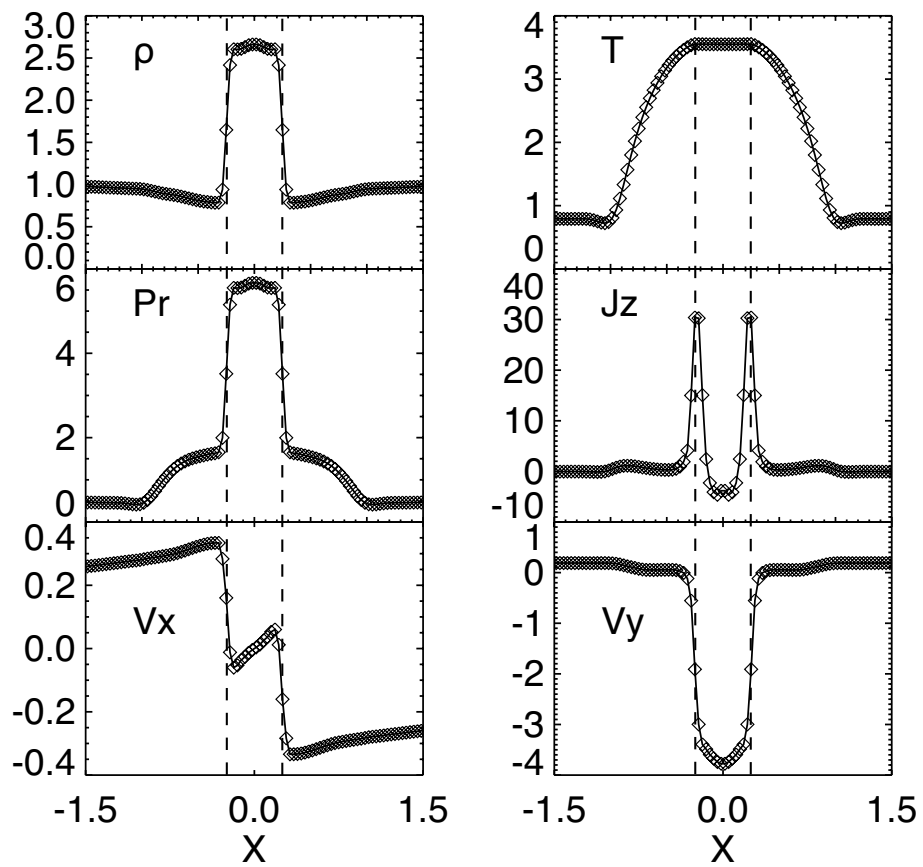


Figure 3.3: One-dimensional plots parallel to the x -axis across $y = 10$ at $t = 13$ (across the reconnection outflow region). The density, temperature, pressure, J_z , v_x and v_y are displayed. The vertical dashed-lines indicate the slow shocks attached to the reconnection outflow.

The thermal structure of the flare loops is determined by a complex coupling among the plasma flows, shocks, and heat conduction. When the reconnection outflow collides with the loop system below, two oblique fast-mode shocks and sometimes a horizontal fast-mode shock (Mach disk) are formed at the top (see Figure 3.4), which indicates that the termination shock is a combination of two or three fast-mode shocks. Note that most of the regions where $\nabla \cdot \mathbf{v}/C_s$ takes large negative values are slow or fast shocks. We found that the strength of the termination shock shows a quasi-periodic oscillation. We also found the shock reflection and Mach reflection in a concave magnetic field at the top (Figures 3.4 and 3.6). The relationship between the oscillation and the flow structure at the top will be discussed in our future papers.

The high-pressure plasma at the loop-top expands along the magnetic field to the foot-points, generating the high-speed downflows. Then the evaporation flows collide with the downflows, forming the dense regions in the flare loops ("humps" in Figure 3.5, named by Yokoyama and Shibata [2001]). After the collision, the fronts of the evaporation flows and downflows becomes slow shocks (see $\nabla \cdot \mathbf{v}/C_s$ maps). The pair of the upward slow shocks finally collide with each other at the apex, forming another dense region (see Figure 3.6). Note that the "blob" named by Yokoyama and Shibata [2001] is different from this high-density region. The blob is the high-density region in a concave magnetic field at the top.

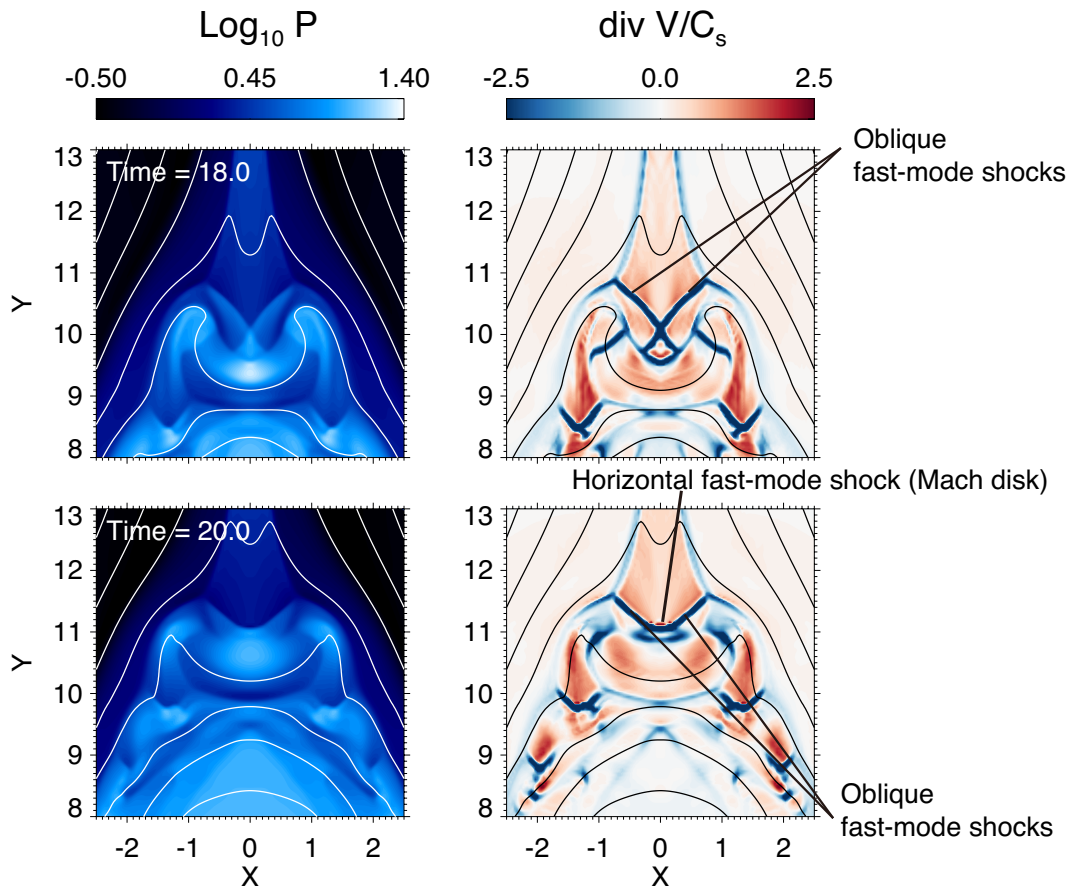


Figure 3.4: Gas pressure (Left) and $\nabla \cdot \mathbf{v}/C_s$ (Right) maps of the loop top. Top: Snapshot when the termination shock consists of two oblique fast-mode shocks. Bottom: Snapshot when the termination shock consists of two oblique shocks and a horizontal shock. Note that most of the regions where $\nabla \cdot \mathbf{v}/C_s$ takes large negative values are slow or fast shocks.

Formation of hump

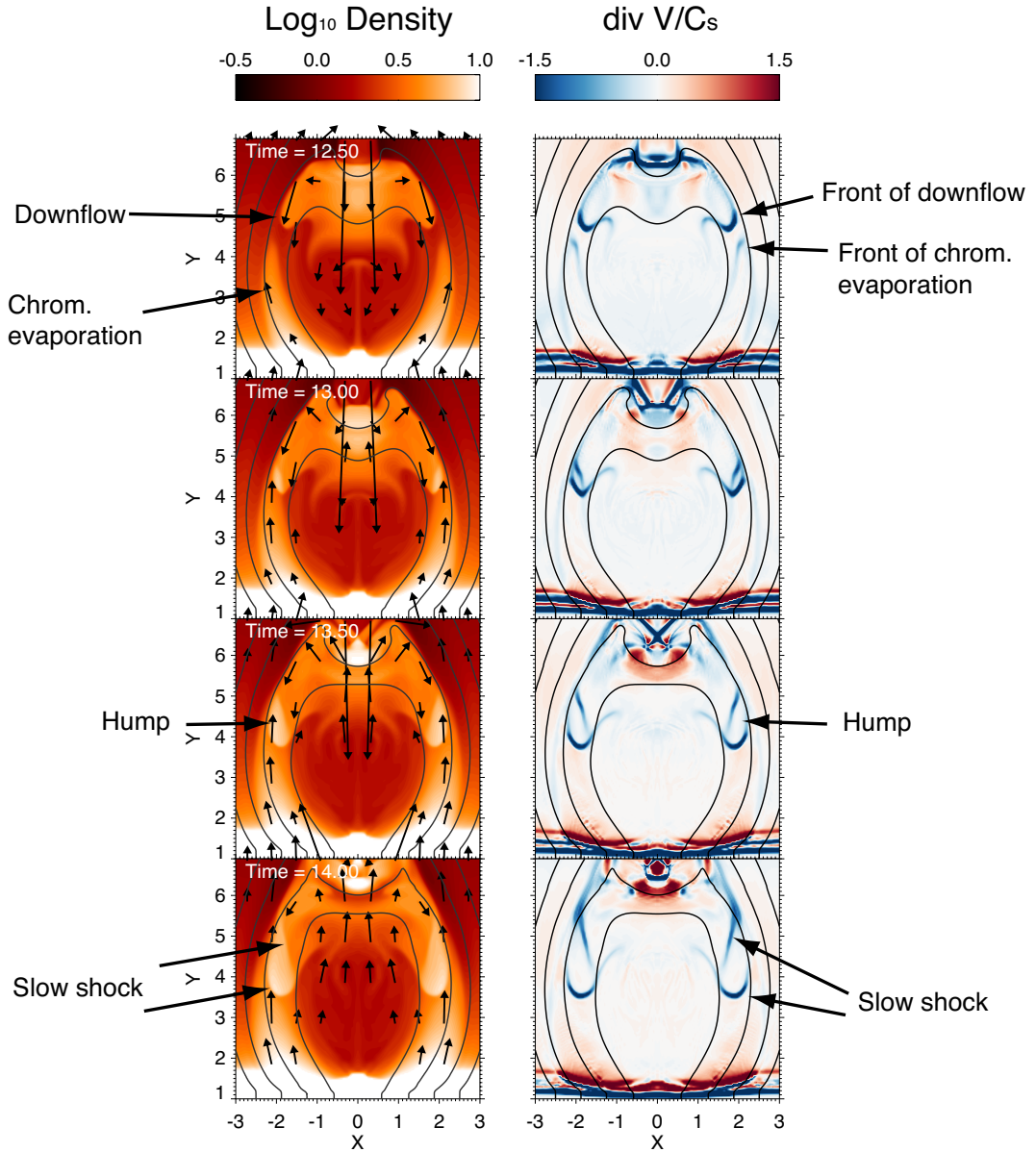


Figure 3.5: Formation of the high-density regions called humps. Left: the density in logarithmic scale. Right: $\nabla \cdot \mathbf{v}/C_s$. The solid lines denote magnetic field lines. The velocity vectors projected to the x-y plane are also displayed in the density maps (only the vectors with $\sqrt{v_x^2 + v_y^2} > 0.3$ are shown). Note that most of the regions where $\nabla \cdot \mathbf{v}/C_s$ takes large negative values are slow or fast shocks.

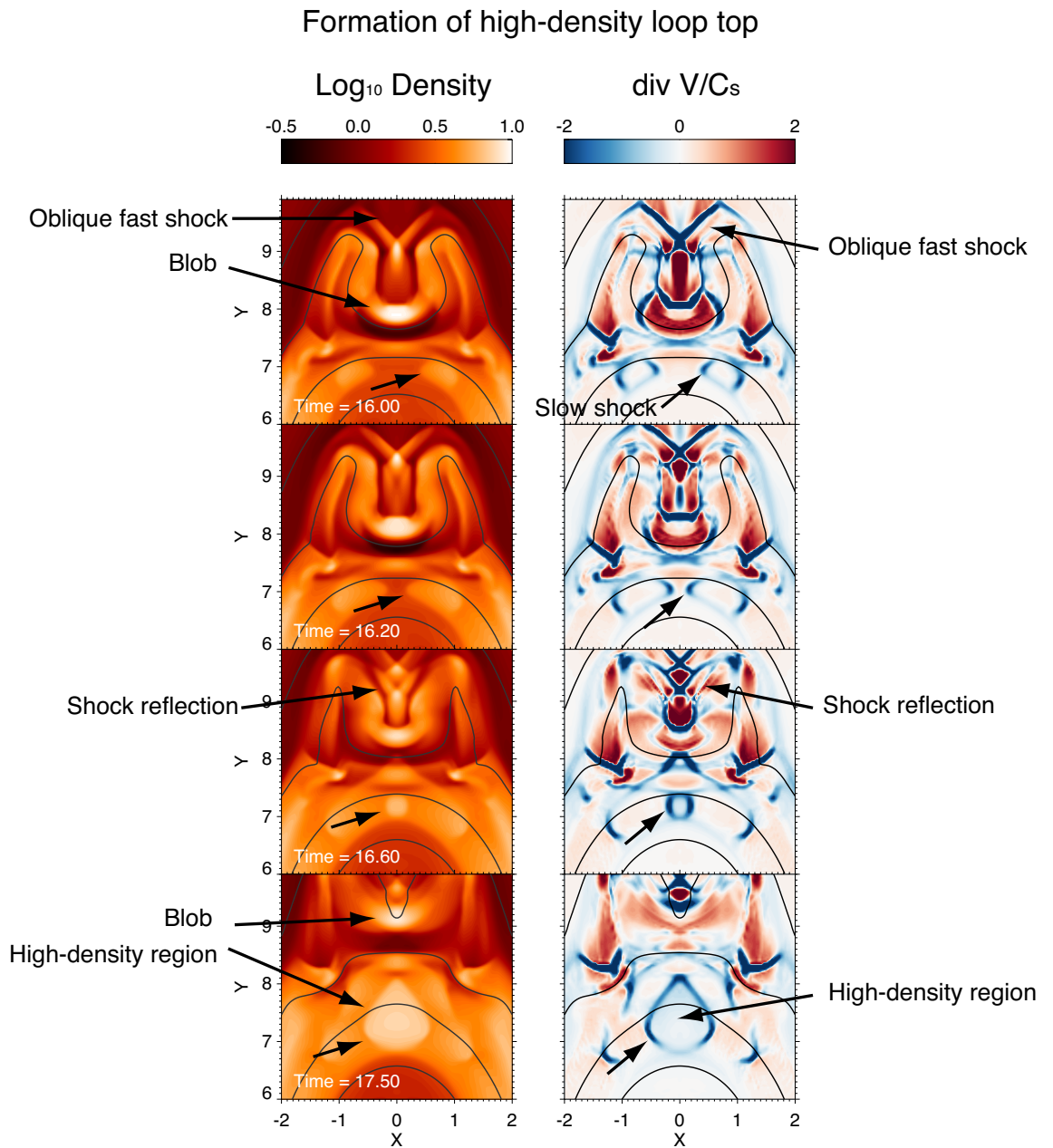


Figure 3.6: Formation of the high-density loop-top. Left: the density in logarithmic scale. Right: $\nabla \cdot \mathbf{v}/C_s$. The solid lines denote magnetic field lines. Only one of the pair of the slow shocks heading to the apex is indicated by the arrows. Note that most of the regions where $\nabla \cdot \mathbf{v}/C_s$ takes large negative values are slow or fast shocks.

Figure 3.7 displays the slow shocks in the flare loops mentioned above. The entropy is discontinuous at the two pairs of the discontinuities in the density map, but the temperature is smooth along the magnetic field, indicating that they are isothermal slow shocks. The plasma β in a large fraction of the flare loops, as well as in the outflow region, is larger than unity (the contour indicates the level where $\beta = 1$), meaning that the low- β approximation cannot be applied to the reconnected magnetic field. This is a consequence of the shock heating and compression. The high-pressure flare loops are confined by the surrounding low- β plasma. This is consistent with the observation by McKenzie [2013]; they concluded that plasma β is of the order of unity or larger than unity in the supra-arcade plasma in two flares analyzed.

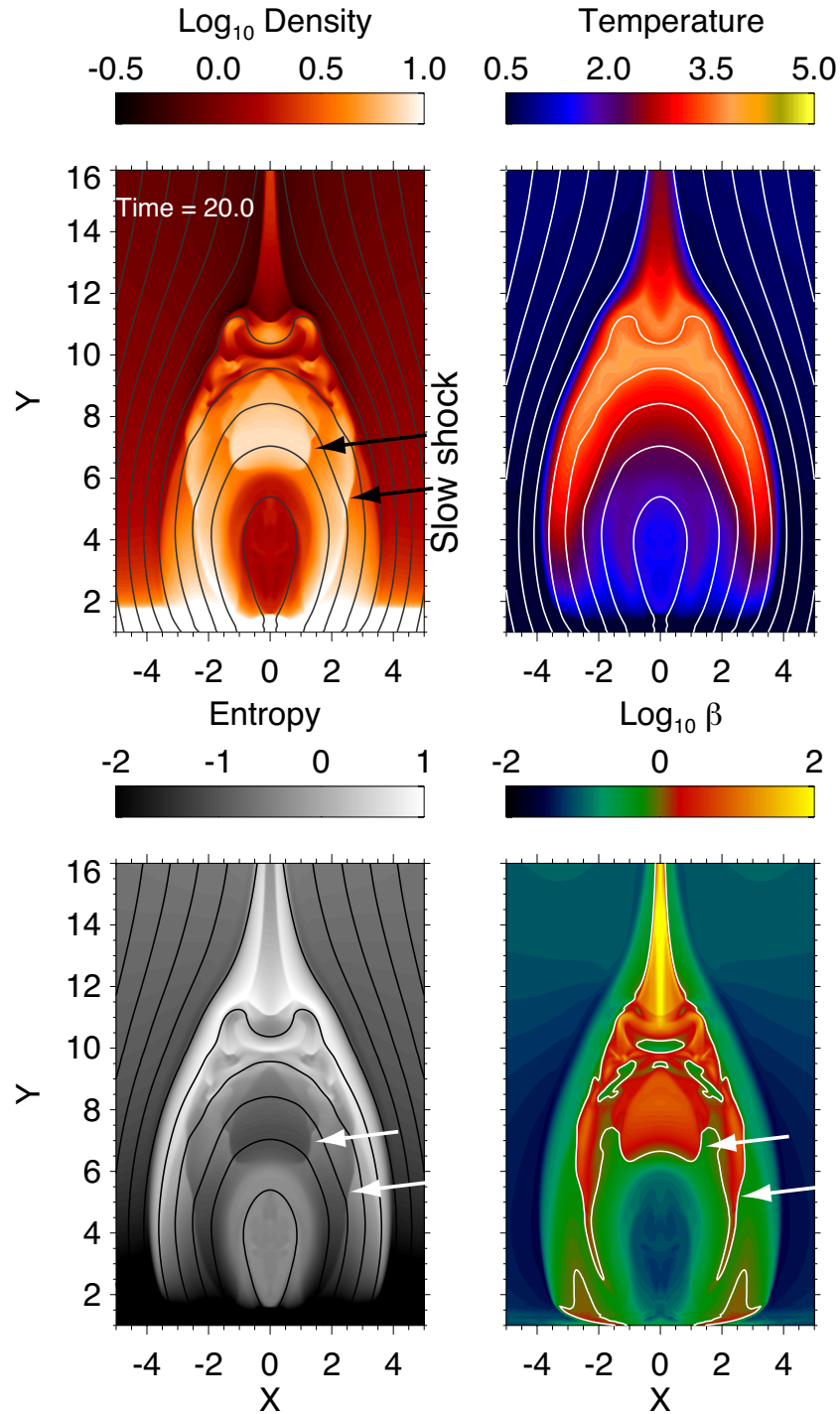


Figure 3.7: Snapshots of the density, temperature, entropy ($\log(p/\rho^\gamma)$), and plasma β at $t = 20$. The arrows indicate slow shocks in the flare loops (See also Figures 3.5 and 3.6). The solid lines in the first three panels denote the magnetic field. The contour in the plasma β map denotes the level where $\beta = 1$ ($\log_{10} \beta = 0$).

3.3.2 Dynamics and Energetics along a Specific Field Line

We have seen the two-dimensional evolution of a solar flare. To study the dynamics of flows along the reconnected magnetic field in detail, kinematics and energetics of the plasma are investigated along selected field lines. We performed the same analysis for other field lines and confirmed that they give similar results.

We picked up a magnetic field line and measured the physical quantities along it. The field line used in the analysis is shown in Figure 3.8. Figure 3.9 displays the time-distance diagrams of the density, temperature, $v_{\parallel} = |(\mathbf{v} \cdot \mathbf{B})\mathbf{B}/B^2|$ and $\nabla \cdot \mathbf{v}/C_s$ along the field line whose foot-point is located at $(x, y) = (1.2, 0)$, where C_s is the local sound speed. The distance is measured along the field line. Before the field line reconnects, the starting point of the distance is the intersection point between the field line and the top boundary. After reconnection, the starting point is the apex of the closed loop. The sign of v_{\parallel} is defined as positive and negative when a plasma flow travels to the apex and foot-points, respectively.

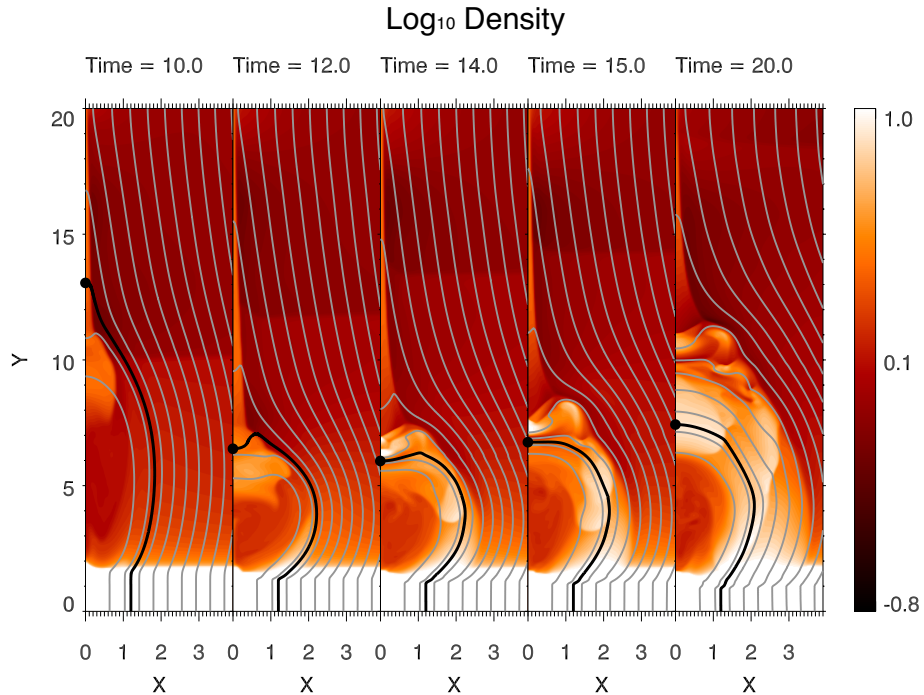


Figure 3.8: Evolution of a specific reconnected field line with the density map. The tracked field line is indicated by the thick black line. The foot-point of the field line is located at $(x, y) = (1.2, 0)$. The circle is the origin of the distance.

In Figure 3.9, we can discern the field line shrinking after reconnection. The heat released at the Petschek slow shocks is transferred to the chromosphere (see the temperature in Figure 3.9), leading to the generation of the chromospheric evaporation. The evaporation flows are seen as upflows from the chromosphere (see ρ and v_{\parallel} maps). The reconnection outflow is significantly decelerated at $t \sim 12$. This is seen as the enhancement of the density and temperature and negative $\nabla \cdot \mathbf{v}$ (compression), indicating that the kinetic energy of the outflow is converted to the thermal energy. After the termination, the high-pressure plasma at the top expands along the magnetic field, forming the downflows. The downflows collide with the chromospheric evaporation flows, leading to the formation of the humps (see also Figure 3.5). After the collision, the fronts of the evaporation flows and downflows become steep and finally become slow shocks. The pair of the upcoming shocks finally cross each other at the apex at $t \sim 16$, forming another high-density region (see also Figure 3.6).

We found slow shocks propagating along the field line, but there is no prominent shocks nor waves propagating back and forth from end to end. They are damped by the heat conduction [e.g. Ofman and Wang, 2002]. Also note that the propagation speed of the shocks is largely decelerated by the evaporation flow (i.e. Doppler effect), which significantly affects the traveling time of the slow-mode waves/shocks (the local sound speed is ~ 1.5 , but the propagation speed is ~ 0.6). That is, a simple estimation by $t_{travel,slow} \sim L/C_s$ is not a good approximation of the traveling time, where L and C_s is the loop length and the sound speed in the loop, respectively. We observe no prominent signature of the standing slow-mode waves in the calculated time range (as for acoustic waves in the flare loops, see e.g. Nakariakov et al. [2004]).

Figure 3.10 shows the time evolution of the total, magnetic, internal (thermal) and kinetic energies integrated along two specific field lines. The top and bottom panels are for the field lines which are rooted at $(x, y) = (1.2, 0)$ and $(1.8, 0)$, respectively. Considering that the cross-sectional area of the flux tube is inversely proportional to the magnetic field strength, we integrate the energies along a field line as follows:

$$E_{mag} = \int ds \frac{B^2}{8\pi} \frac{1}{B}, \quad (3.15)$$

$$E_{int} = \int ds \frac{p}{\gamma - 1} \frac{1}{B}, \quad (3.16)$$

$$E_{kin} = \int ds \rho \frac{v^2}{2} \frac{1}{B}, \quad (3.17)$$

$$E_{tot} = E_{mag} + E_{int} + E_{kin}. \quad (3.18)$$

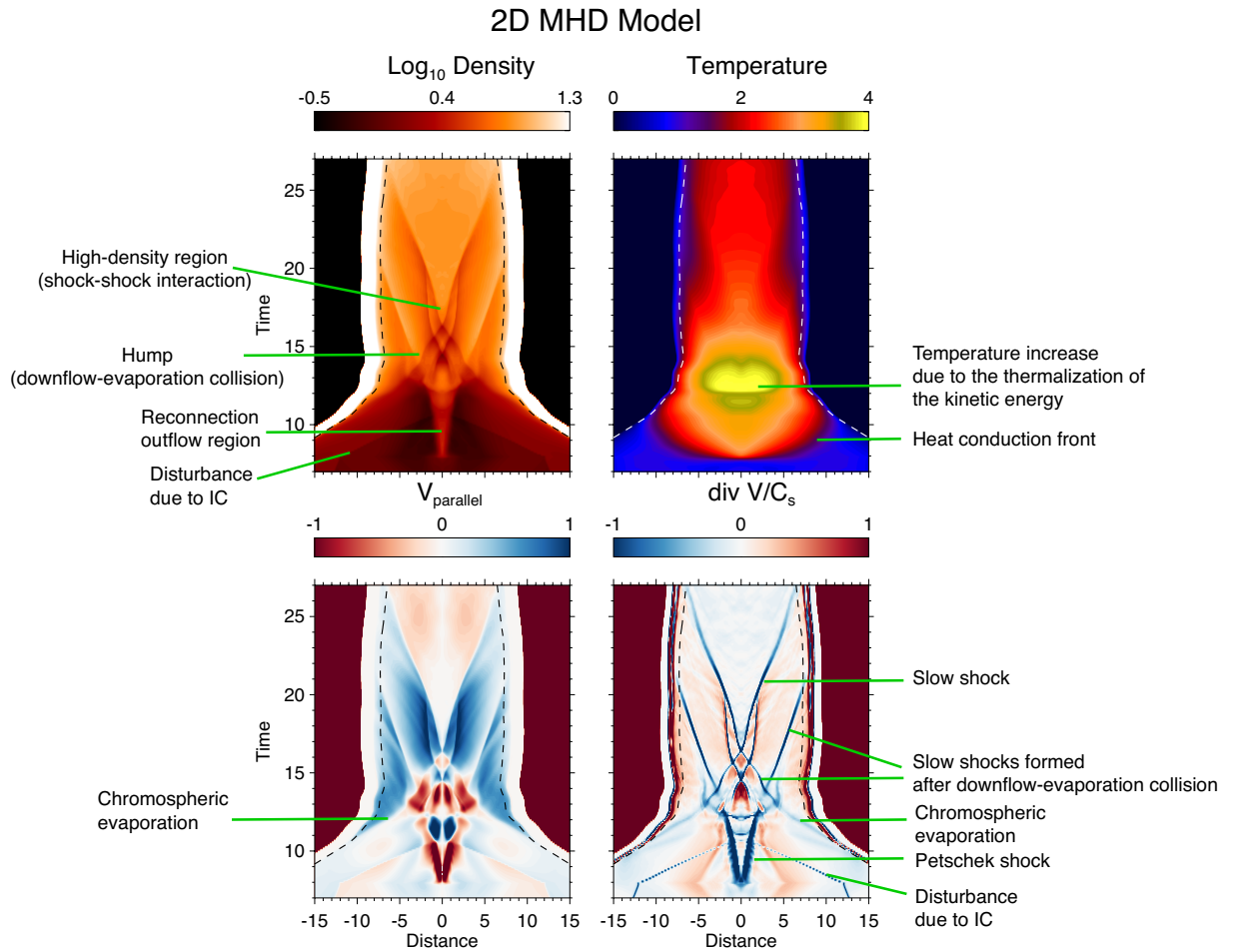


Figure 3.9: Time-distance diagrams of the density (Top Left), temperature (Top Right), v_{\parallel} (Bottom left), and $\nabla \cdot \mathbf{v}/C_s$ (Bottom Right). The physical quantities are measured along the field line which is originated from $(x, y) = (1.2, 0)$. The distance is measured along the field line, and its origin is the apex ($x = 0$). The data of the domain of $x < 0$ is also shown just for visual inspection. The sign of v_{\parallel} is defined as positive and negative when a plasma flow travels to the apex and foot-points, respectively. This field line does not pass through the termination shock. Note that the regions where $\nabla \cdot \mathbf{v}/C_s$ takes large negative values are slow or fast shocks.

In this chapter, all the energies are normalized by the initial total energy. After the field lines reconnect ($t \sim 8$), the magnetic energy is rapidly converted to the internal and kinetic energies. As for the field line rooted at $(x, y) = (1.2, 0)$, the maximum value of the kinetic energy is 0.35. Let us define the time when E_{kin} becomes $E_{kin,max}$ as t_{peak} . If we compare the total, magnetic and internal energies at $t = 0$ and those at $t = t_{peak} + 10$, $dE_{tot} = E_{tot}(t = t_{peak} + 10) - E_{tot}(t = 0) \sim 0.15$, $-dE_{mag} = -(E_{mag}(t = t_{peak} + 10) - E_{mag}(t = 0)) \sim 0.45$, and $dE_{int} = E_{int}(t = t_{peak} + 10) - E_{int}(t = 0) \sim 0.6$. Note that the variation of the total energy remains within $\sim 15\%$. The field line rooted at $(x, y) = (1.8, 0)$ also gives a similar result. The small variation in the total energy reflects the fact that the compressive and expanding motions by the surrounding plasma are localized in time and space (see Figure 3.9). Therefore, the compressive motion of the reconnected flux tube is found to be not significant with respect to the total energy variation.

3.4 Pseudo-2D MHD Model of a Flare Loop

3.4.1 Physical Processes Considered

Through the analysis of the 2D MHD simulation, we found that the field-aligned plasma motions (particularly evaporation flows and slow shocks) and heat conduction seem to mainly determine the dynamics in the flare loops. Fast shocks are important for converting the kinetic energy of the reconnection outflow to the heat and for locally changing the cross-sectional area, but they do not largely change the total energy of the field lines (Figure 3.10). On the basis of the results, we aim to model the multi-dimensional reconnection and flare processes in a simplified MHD scheme.

What is important for conduction-heating-type flare modeling would be 1. to model a reconnected field line, 2. to model the reconnection inflow and outflow, 3. to include MHD waves (since MHD waves can carry a large amount of the released energy from the reconnection sites [Kigure et al., 2010]), 4. termination of the reconnection outflow and energy conversion of the kinetic energy of the outflow into the thermal energy, and 5. to include the heat conduction which is essential to determine the temperature of the flare loops.

Considering that the plasma motions are frozen-in a magnetic field, a 1D MHD model will be the simplest form among the possible MHD models. We developed a model based on the 1D MHD equations, where all the variables depend on one space dimension and all the three components of the magnetic and velocity fields are

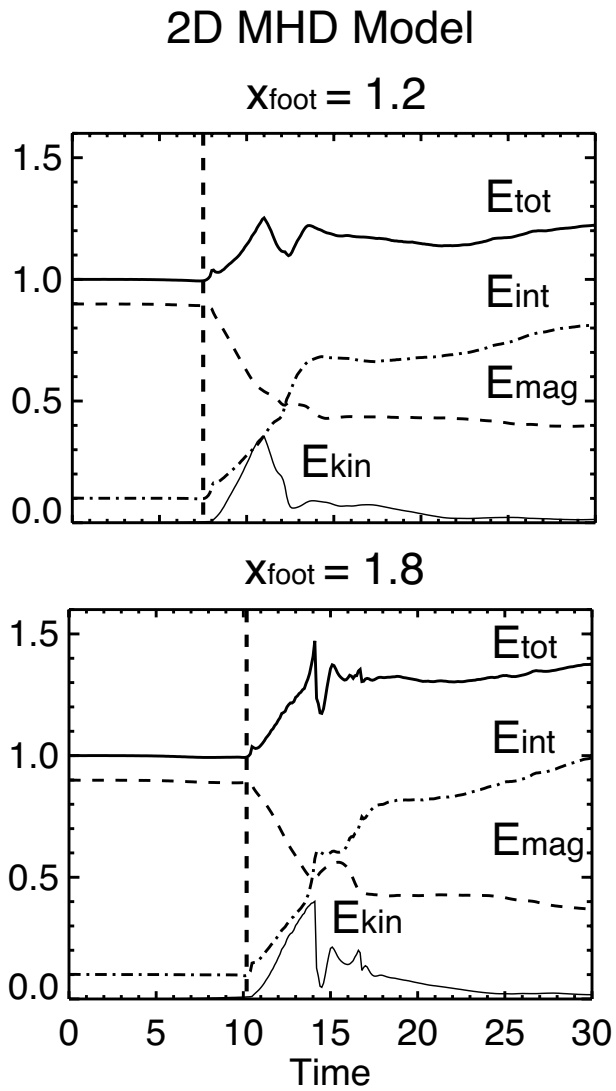


Figure 3.10: Time evolution of the total (thick solid), magnetic (dashed), internal (dash-dot), and kinetic (thin solid) energies along the specified field lines in the 2D MHD model. The vertical dashed lines denote the times when each field line reconnects.

considered. We regard our model as a pseudo-2D MHD model. Note that the meaning of "pseudo-2D" of our model is different from that of Hori et al. [1997] hydrodynamic model which consists of isolated and fixed semi-circular loops with different lengths and constant cross-section.

3.4.2 Assumptions and Basic Equations

We take a cartesian coordinate system in which all the variables are functions of x . The reconnection outflow is in the y -direction. z is the ignorable coordinate (uniform in the z -direction).

We mimic a reconnected magnetic field line by assuming a magnetic field with a sharp bend (see Figure 3.11). The magnetic field line shrinks with time and drives the flow perpendicular to the field which represents the reconnection outflow.

A schematic picture of our model is as follows. Figure 3.12 displays a comparison of our pseudo-2D MHD model with the 2D MHD model. h_{rx} is the height of the reconnection point, and x_{max} is the location of the foot-point of the field line. They are linked by the relation of $x_{max} = h_{rx} \tan \theta$. The reconnection angle θ and the initial plasma beta β are treated as free parameters. If a guide-field (the z -component of the magnetic field) is included, the guide-field angle $\phi = \tan^{-1}(B_z/B_x)$ will be an additional parameter.

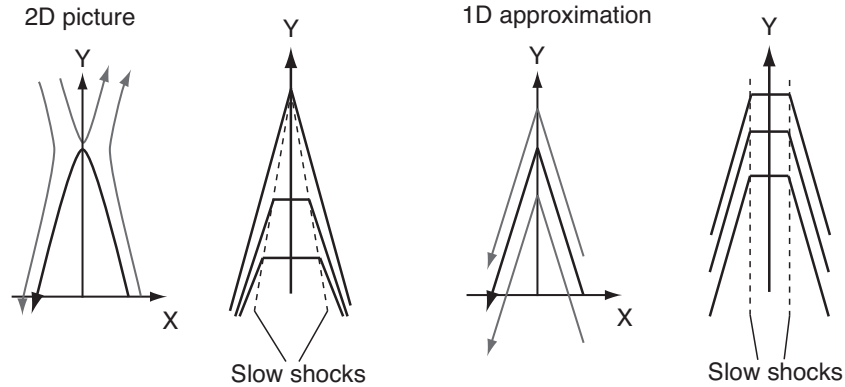


Figure 3.11: Schematic diagram of the reconnected magnetic field in 2D (Left) and the magnetic field mimicking the reconnected field in the 1D-approximation model (pseudo-2D MHD model, Right). The bottom panels show the difference in the reconnected magnetic field configurations between two models.

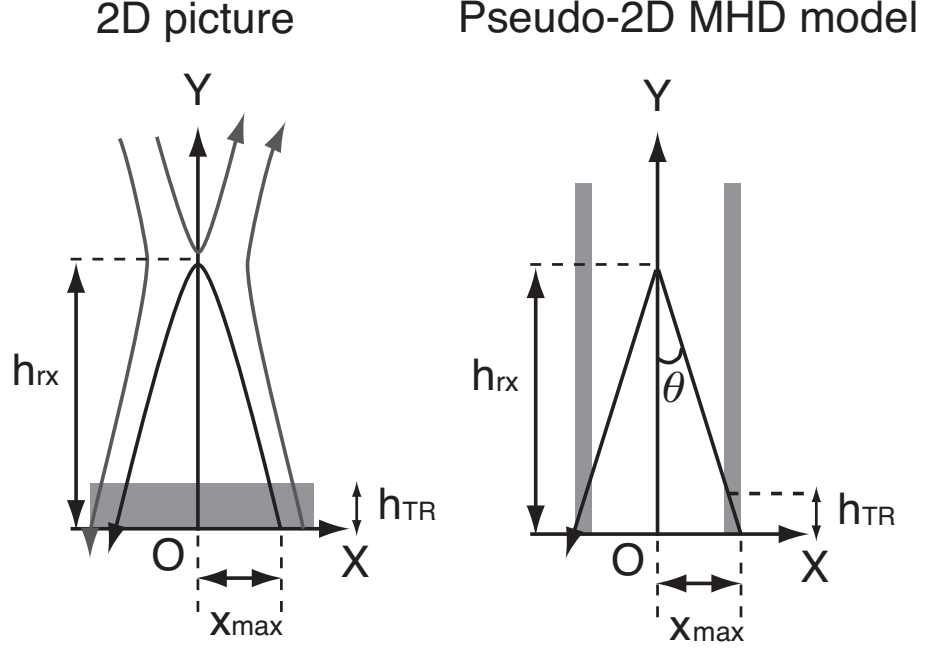


Figure 3.12: Schematic diagram of the set up of our pseudo-2D flare model (Right) based on a 2D picture (Left). h_{rx} and h_{TR} are the height of the reconnection point and height of the transition region, respectively. $\tan^{-1}(x_{max}/h_{rx}) = \theta$ is the reconnection angle. The grey shaded regions indicate the dense cool material representing the chromosphere. Note that in the pseudo-2D MHD model, all the physical quantities are function of x .

The shrinking motion of the reconnected field line will stop when it collides with the magnetic loops piling up below. To model this process, the final configuration of the field line is given in the model and the outflow is decelerated when the field line approaches the final state. The termination process is modeled by adding a damping term to the equation of motion perpendicular to the moving field line. We let the damping term work only when the reconnected field line comes close to the final configuration.

According to Figure 3.10, the total energy of a field line is conserved within several 10 %. On the basis of this result, we hypothesize that the total energy in a reconnected flux tube is conserved. The cross-sectional area in our model is assumed to be uniform and constant in time.

The basic equations are as follows:

$$\frac{\partial \rho}{\partial t} + \frac{\partial}{\partial x}(\rho v_x) = 0, \quad (3.19)$$

$$\frac{\partial B_y}{\partial t} - \frac{\partial}{\partial x}(v_y B_x - v_x B_y) = 0, \quad (3.20)$$

$$\frac{\partial B_z}{\partial t} - \frac{\partial}{\partial x}(v_z B_x - v_x B_z) = 0, \quad (3.21)$$

$$\frac{\partial e}{\partial t} + \frac{\partial}{\partial x} \left[(e + p + \frac{|\mathbf{B}|^2}{8\pi})v_x - \frac{1}{4\pi}B_x(\mathbf{v} \cdot \mathbf{B}) + \kappa_0 T^{5/2} \frac{B_x^2}{|\mathbf{B}|^2} \frac{\partial T}{\partial x} \right] = 0, \quad (3.22)$$

$$\frac{\partial(\rho v_x)}{\partial t} + \frac{\partial}{\partial x} \left[\rho v_x^2 + p + \frac{|\mathbf{B}|^2}{8\pi} - \frac{B_x^2}{4\pi} \right] = -\nu_b(\Delta d(x, t))\rho v_{\perp x}, \quad (3.23)$$

$$\frac{\partial(\rho v_y)}{\partial t} + \frac{\partial}{\partial x} \left[\rho v_x v_y - \frac{B_x B_y}{4\pi} \right] = -\nu_b(\Delta d(x, t))\rho v_{\perp y}, \quad (3.24)$$

$$\frac{\partial(\rho v_z)}{\partial t} + \frac{\partial}{\partial x} \left[\rho v_x v_z - \frac{B_x B_z}{4\pi} \right] = 0, \quad (3.25)$$

$$e = \frac{p}{\gamma - 1} + \frac{1}{2}\rho|\mathbf{v}|^2 + \frac{|\mathbf{B}|^2}{8\pi}, \quad (3.26)$$

$$p = \frac{k_B}{m}\rho T, \quad (3.27)$$

where $\mathbf{v} = (v_x, v_y, v_z)$, $\mathbf{B} = (B_x, B_y, B_z)$, $v_{\perp x} = (\mathbf{v} - \mathbf{v}_{\parallel})_x$, $v_{\perp y} = (\mathbf{v} - \mathbf{v}_{\parallel})_y$, and $\mathbf{v}_{\parallel} = \mathbf{B}(\mathbf{v} \cdot \mathbf{B})/|\mathbf{B}|^2$. All the physical quantities are only dependent of x and t . Note that we include a damping term in the momentum equations that slows down only the x and y -components of the velocity perpendicular to the magnetic field. The detailed description of the damping term is given below. Note that the total energy is conserved along a field line, and that the kinetic energy reduced by the damping term is converted into the thermal energy. The normalization units are the same as those in the 2D MHD model (See Table 3.1). Note that this model can treat slow-mode, fast-mode and Alfvén waves.

Considering the symmetry, we only solve the domain within $0 \leq x \leq x_{max}$. At the boundary of $x = 0$ the mirror symmetric boundary conditions are imposed. The boundary of $x = x_{max}$ is free.

The initial conditions are as follows. The free parameters that determine the initial magnetic field are the plasma beta $\beta = 8\pi p/|\mathbf{B}|^2$, and the angles θ and ϕ (see Figure 3.12). The guide field effect is detailed in Appendix A.3. The initial magnetic field

is given by

$$B_0 = \sqrt{\frac{8\pi p_0}{\beta}}, \quad (3.28)$$

$$B_x(x) = -B_0 \sin \theta \cos \phi, \quad (3.29)$$

$$B_y(x) = B_0 \cos \theta \cos \phi, \quad (3.30)$$

$$B_z(x) = B_0 \sin \theta \sin \phi. \quad (3.31)$$

The gas pressure is assumed to be uniform (p_0). The domain is divided into the two layers, namely chromosphere and corona:

$$\rho(x) = \rho_{cor} + (\rho_{chr} - \rho_{cor}) \frac{1}{2} \left[1 + \tanh \left(\frac{x - x_{TR}}{w_{TR}} \right) \right], \quad (3.32)$$

where x_{TR} is the location so that $y_{line}(x_{TR}, t = 0) = h_{TR}$. Where $y_{line}(x, t)$ is a function that describes the configuration of the field line.

The initial and final magnetic field configurations are described as follows. See also Figure 3.13. The reconnection point (the location of the sharp bend) is assumed to be at $(x, y) = (0, h_{rx})$. The initial condition of a magnetic field is written as

$$y_{line}(x, t = 0) = -\frac{1}{\tan \theta} (x - x_{max}), \quad (3.33)$$

for $x \geq 0$. The final state of the magnetic field is approximated by a quadratic function of

$$y_{line,fin}(x) = -\frac{x_{max}}{2 \tan \theta} \left[\left(\frac{x}{x_{max}} \right)^2 - 1 \right], \quad (3.34)$$

which has the same slope of the tangent line with the equation (3.33) at $x = x_{max}$.

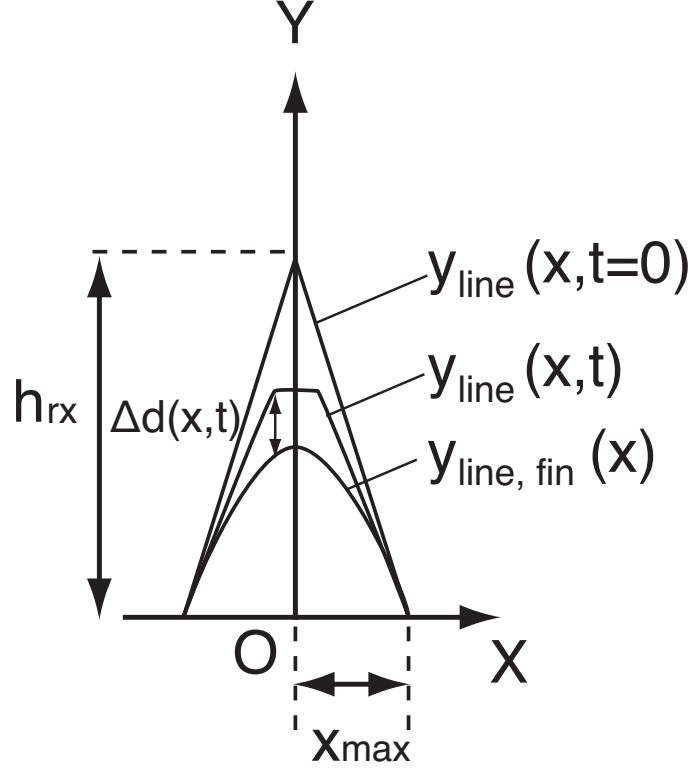


Figure 3.13: The magnetic configurations of a specific field line in the initial state ($y_{line}(x, t = 0)$), at $t = t$ ($y_{line}(x, t = t)$), and in the final state ($y_{line,fin}(x)$), respectively. $\Delta d(x, t) = y_{line}(x, t) - y_{line,fin}(x)$ is also described.

We virtually consider the travel distance of the reconnected field line in the y -direction. When the field line approaches the final state, the damping term is applied only to the x - and y -components of the velocity perpendicular to the field line. We define the distance in the y -direction between the field line at (x, t) and the field line in the final state as

$$\Delta d(x, t) = y_{line}(x, t) - y_{line,fin}(x). \quad (3.35)$$

The damping term only works when the field line approaches to the final state:

$$\nu_d(\Delta d(x, t)) = \frac{1}{t_{damp}} \frac{1}{2} \left[1 - \tanh \left(\frac{\Delta d(x, t)}{w_d} \right) \right], \quad (3.36)$$

where $t_{damp} = w_d/v_{A,y}$, $V_{A,y} = B_y/\sqrt{4\pi\rho_{cor}}$ is the outflow speed in the y -direction, and w_d is a free parameter that denotes a typical braking distance. To prevent the field line

from shrinking further even after the travel time $t_{travel} = (h_{rx} - y_{line,fin}(x=0))/V_{A,y}$, we increase the damping coefficient ν_d by a factor of 100 after the time $t = 1.2t_{travel}$. Note that the term arising from the damping terms is not included in the energy equation under the assumption that the total energy along a field line is conserved. The kinetic energy decreased by the damping term is converted only into the thermal energy.

The reconnection angle θ and plasma beta β are important parameters to determine the total released magnetic energy and energy conversion rate (say, reconnection rate). To choose a physically acceptable parameter set, we utilize the analytical approach by [Falle et al. \[1998\]](#). A detailed description is presented in [Appendix A.3](#).

The height of the reconnection point h_{rx} is assumed to be $20 = y_{max,2D}$, and the reconnection angle θ is $\pi/12$. The domain size is therefore $x_{max} = h_{rx} \tan \theta = 20 \tan(\pi/12)$. The width of the transition region and the typical damping distance are respectively $w_{TR} = w_{TR,2D} = 0.2$ and $w_d = 2$.

The numerical scheme of the pseudo-2D MHD model is based on the [Vögler et al. \[2005\]](#): the fourth-order space-centered difference for spatial derivative and an explicit four-step Runge-Kutta time integration. We explicitly solve the heat conduction term. Using the current computational resources, it is not difficult to explicitly solve the heat conduction in our 1D calculations. The domain is resolved by 640 grids.

3.5 Numerical Results of Pseudo-2D MHD Model

3.5.1 Dynamics and Energetics

Figure [3.14](#) demonstrates the time evolution of the magnetic field structure. The field line retracts and sweeps up the plasma like a slingshot. The reconnection outflow is decelerated when the field line approaches the assumed final configuration. In the following, we performed the same analysis as for the 2D MHD model.

One-dimensional plots shown in [Figure 3.15](#) demonstrate the formation of a pair of two slow shocks attached to the reconnection outflow, that is, the Petschek-type slow shocks. As well as the 2D MHD model ([Figure 3.3](#)), the Petschek-type shocks are isothermal shocks due to the heat conduction.

[Figure 3.16](#) compares the field-aligned motions in the pseudo-2D MHD model and 2D MHD model. As well as in the 2D MHD model, the heat generated at the Petschek slow shocks is transferred to the chromosphere by the heat conduction, forming the chromospheric evaporation. The humps and high-density regions at the top are found

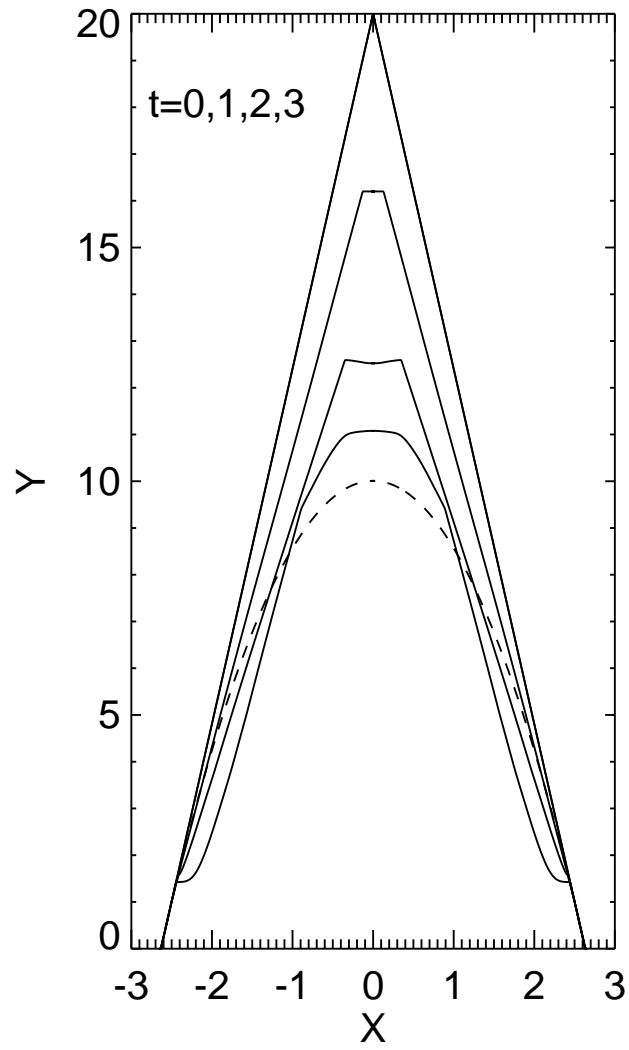


Figure 3.14: Downward moving magnetic field line in the pseudo-2D MHD model. The dashed line denotes the assumed final configuration $y_{line,fin}$.

One-dimensional plots of the reconnection outflow
(Pseudo-2D MHD Model)

Time = 0.7

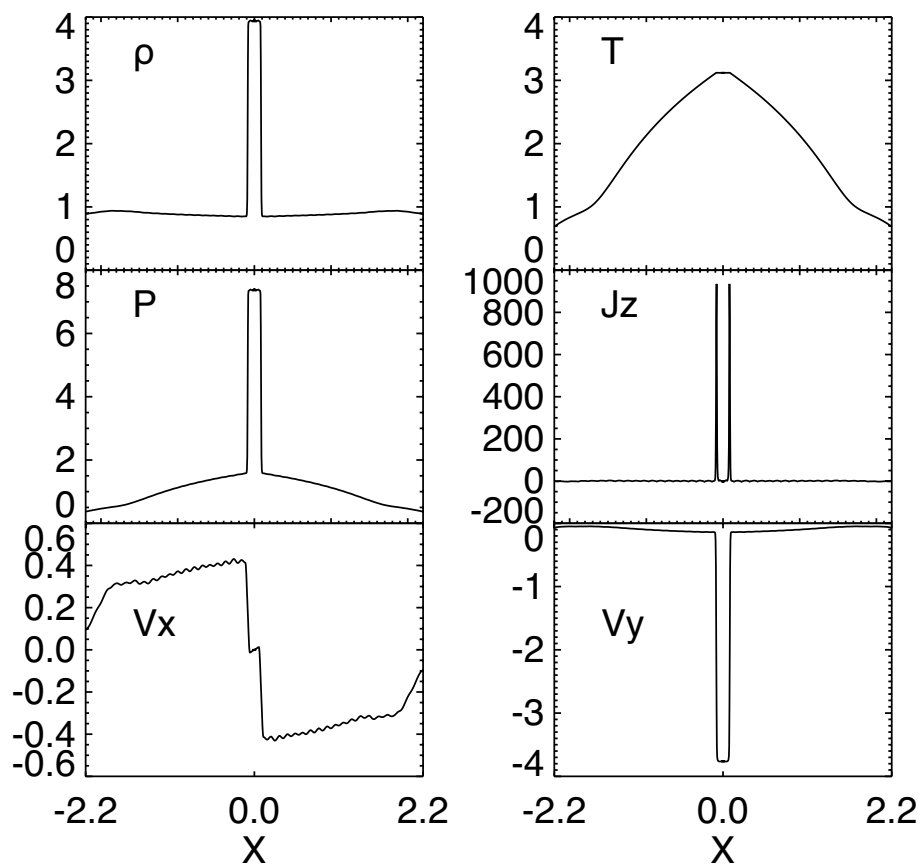


Figure 3.15: One-dimensional plots parallel to the x -axis at $t = 0.7$ (across the reconnection outflow region). The density, temperature, pressure, J_z , v_x and v_y are displayed.

to be formed in the same way as in the 2D MHD model: the downflow-evaporation collision and shock-shock interaction, respectively. The damping of the slow shocks are also observed.

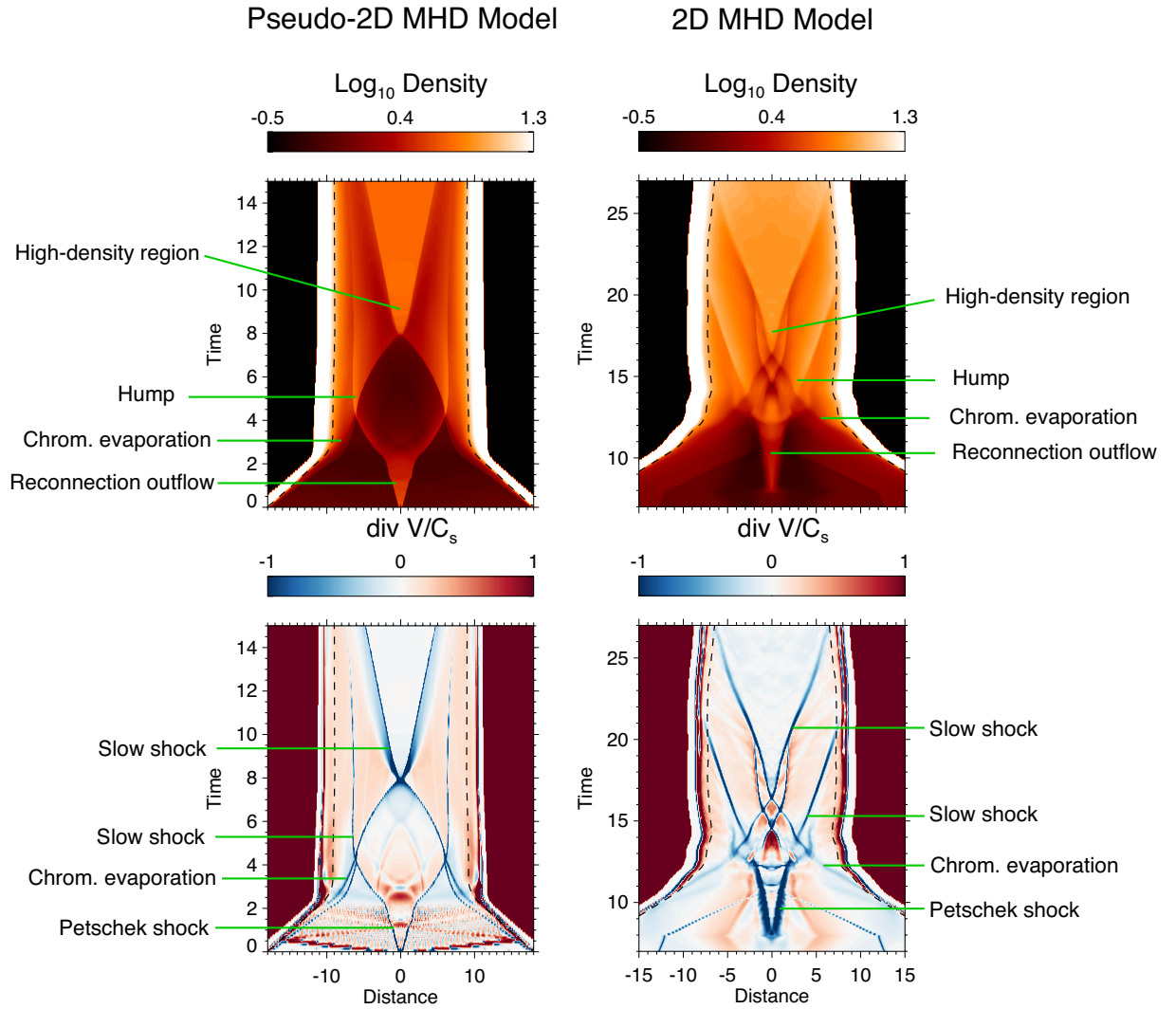


Figure 3.16: Comparison between the pseudo-2D MHD model (Left) and the 2D MHD model (Right). Time-distance diagrams of the density and $\nabla \cdot \mathbf{v}/C_s$ are shown. The physical quantities of the 2D MHD model are measured along the field line which is originated from $(x, y) = (1.2, 0)$. The distance is measured along the field line, and its origin is the apex ($x = 0$). The data of the domain of $x < 0$ is also shown just for visual inspection. Note that most of the regions where $\nabla \cdot \mathbf{v}/C_s$ takes large negative values are slow or fast shocks.

The energy evolution is examined in the pseudo-2D MHD model. When we integrate the energies, we drop off the term $1/B$ in the integrand because in the pseudo-2D MHD model the variation of the cross-sectional area is not considered. Figure 3.17 is the same as Figure 3.10 but for the pseudo-2D MHD model. It is shown that $-dE_{mag} \sim 0.6$, $dE_{int} \sim 0.55$, and $E_{kin,max} \sim 0.25$, which is similar to the results of the 2D MHD model.

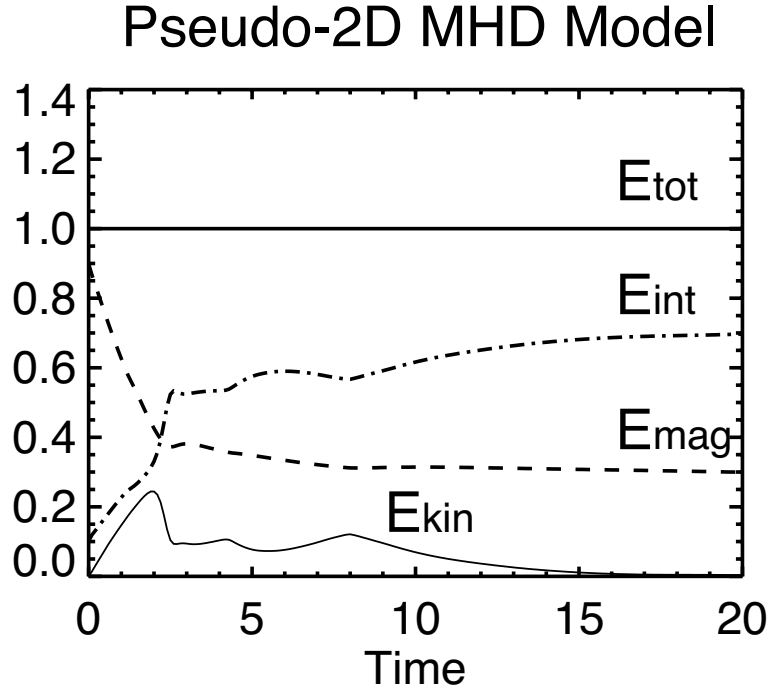


Figure 3.17: Time evolution of the total (thick solid), magnetic (dashed), internal (dash-dot), and kinetic (thin solid) energies along a field line in the pseudo-2D MHD model.

3.5.2 Dependence on Parameters

Previously a formula that determines the flare loop temperature was derived under the assumption that the energy input to a loop balances with the conduction cooling rate [Fisher and Hawley, 1990]. The formula is given by

$$T \sim \left(\frac{QL_{loop}^2}{2\kappa_0} \right)^{2/7}, \quad (3.37)$$

where Q is the volumetric heating rate and L_{loop} is the half length of the magnetic field line of a flare loop. The heating rate by magnetic reconnection is determined by the Poynting flux: $Q = B^2/(4\pi) \times V_A/L_{loop}$. Using this, the temperature can be written as

$$T \propto \beta^{-3/7} h_{rx}^{2/7} \kappa_0^{-2/7}, \quad (3.38)$$

by assuming that $L_{loop} \sim h_{rx}$. This scaling law was derived by [Yokoyama and Shibata \[1998, 2001\]](#). We checked whether the scaling law based on a magnetic reconnection model holds in our pseudo-2D MHD model.

Figure 3.18 shows the numerically-obtained β - T , h_{rx} - T and κ_0 - T relations. T_{jet} denotes the temperature in the reconnection outflow. T^* denotes the maximum temperature after the pair of the two slow shocks generated by the chromospheric evaporation flows collides at the apex. As shown in Figure 3.18, it is found that the temperature in the loop obeys the scaling law well.

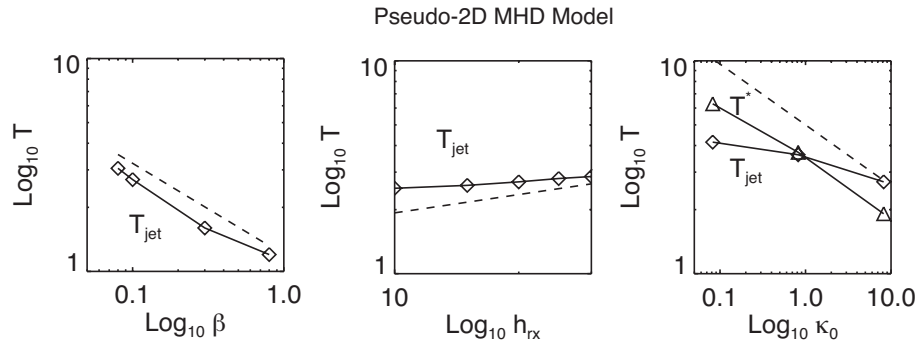


Figure 3.18: Temperature as a function of the initial β (Left), the height of the reconnection point h_{rx} (Middle), and the heat conductivity κ_0 (Right), respectively. The data points are taken from the pseudo-2D MHD simulations. T_{jet} denotes the temperature in the reconnection outflow. T^* denotes the maximum temperature after the pair of the two slow shocks generated by the chromospheric evaporation flows collides at the apex. The dashed lines show the analytical scaling laws.

3.6 Summary and Discussion

In this chapter, we investigated the flow structure, shock formation and thermal evolution in the flare loops using MHD simulations. On the basis of the 2D simulation result, we have developed a new flare loop model (the pseudo-2D MHD model). We compare the flow structure, shock formation and energetics of a specific field line in

the 2D calculation with those in the pseudo-2D MHD model, and then we find that they give similar results. Here we summarize the results and compare our results with previous studies.

Performing a 2D MHD simulation, we found new shock structures. The termination shock consists of two oblique fast-mode shocks and sometimes a horizontal fast-mode shock (Figure 3.4). A hump is formed as a result of the collision of the downflow and the chromospheric evaporation flow. After the collision, the fronts of the evaporation flow and downflow become slow shocks, and then the hump appears as a dense region behind the two slow shocks (Figure 3.5). The upward slow shock finally interact with the slow shock coming from the other side at the top, forming the high-density region. Note that the high-density region is separated from the blob in Yokoyama and Shibata [2001] and is formed below it (Figure 3.6).

We found that the strength of the termination shock in the 2D MHD model shows a quasi-periodic oscillation, which is a multi-dimensional feature. In addition, the shock reflection and Mach reflection are sometimes observed in a concave magnetic structure, which could be important for understanding the heating in the loop-top. These complicated structures at the top will be detailed in our future papers.

We observe no prominent shocks nor waves propagating back and forth from end to end. In addition, no prominent standing slow-mode waves are observed within the calculated time range. By performing 2D MHD simulations without the heat conduction, we confirmed that without the heat conduction the slow shocks formed at the fronts of the downflows from the top propagate back and forth from end to end. Thus the propagation of the slow shocks in the flare loops is found to be significantly affected by the heat conduction and evaporation flows. The slow shocks are damped by the heat conduction. The propagation speed of the slow shocks is reduced by the evaporation flow (Doppler effect), which makes the shock propagation time longer. Therefore it is essential to consider the flows resulting from reconnection (particularly downflows from the top) for understanding the behavior of magneto-acoustic waves in the flare loops.

In fully 3D situations, reconnection can be intermittent in space and time, which could affect the shock structures found in this study. 3D component reconnection, where reconnecting magnetic field lines are not perfectly anti-parallel, can result in the reconnection outflow jet with a speed insufficient for the formation of the fast shock above the loop top. However, in the case that the reconnection outflow speed exceeds the fast mode phase speed in the outflow region, we expect the formation of the termination shock found as in our 2D MHD model. We also expect that the slow shocks presented in the 2D MHD model will be formed in 3D, since the field-aligned

plasma flows which are essential to form slow shocks are well treated in our MHD flare modeling scheme.

From the 2D simulation, we found that the field-aligned plasma motions (particularly evaporation flows and slow shocks) and heat conduction mainly determine the dynamics in the flare loops. Considering this, we construct the pseudo-2D MHD model which is basically a 1D MHD model. The pseudo-2D MHD model is compared with the 2D MHD model, and we found that the dynamics (particularly flow structure and shock formation) and the energetics are similar between the two models. The scaling law for the temperature based on a reconnection model is also examined, and it is found that the scaling law holds in the pseudo-2D MHD model. These facts indicate that our pseudo-2D MHD model captures important features of a reconnection model of solar flares.

1D hydrodynamic models, like [Mariska et al. \[1989\]](#) and [Hori et al. \[1997, 1998\]](#), have been used for the flare loop modeling. The models are useful to study the thermal evolution and flows in the flare loops, but the energy input (in many cases the heat input) must be done by hand. Our model includes many features of the multi-dimensional MHD processes related to magnetic reconnection, like the heating by the Petschek slow shocks and conversion of the kinetic energy of the reconnection outflow to the heat. Another important point is that our model can treat MHD waves and shocks generated in the flare loops, which could be important to understand the flow structure in the loops.

We note that all the previous 1D hydrodynamic models lack the strong downflows from the top (for example, see Figure 5 in [Hori et al. \[1997\]](#)). We showed that the downflows play important roles in forming the humps and slow shocks (Figures 3.5 and 3.6). Our pseudo-2D MHD model naturally produces the downflows from the top, allowing us to study the dynamic evolution of the thermal structure.

A theoretical model in which field lines shorten after localized 3D reconnection based on the thin flux tube approximation was proposed by [Longcope et al. \[2009\]](#). The model assumes that the plasma has always low- β . Our 2D MHD simulation demonstrates that, because of the shock heating and compression, the plasma β becomes larger than unity not only in the reconnection outflow but also in a large part of the flare loops (see Figure 3.7). In such regions, we need to consider the effects of the gas pressure to understand the flow and shock structures. Our pseudo-2D MHD model can treat the high- β plasma. [Longcope et al. \[2009\]](#) model could be valid in the situation in which the shock heating does not break the low- β assumption (e.g. in the situation in which the guide-field is much stronger than the reconnection field). Regarding this issue, see

also Appendix A.3.

The high- β condition could lead to disordering of the magnetic field when turbulence is important so that the geometrical assumptions made for our pseudo-2D MHD model are not met. We found no evidence that turbulence is important in the current sheet in our 2D MHD model. Our model will be useful to model the reconnected field lines in such a situation in which turbulence is not important.

As a result of the approximations made for the pseudo-2D MHD model, some multi-dimensional processes such as termination shock formation and turbulence cannot be modeled. However, the pseudo-2D MHD model are able to treat plasma flows and waves/shocks (slow-mode waves/shocks and Alfvén waves) along the magnetic field, which could be useful to understand the plasma motions in the flare loops.

Our pseudo-2D MHD model requires much smaller computational cost than other multi-dimensional MHD models. This model will allow us to study the evolution of the flare loops in a wide parameter space without expensive computational cost. Also, it will be much easier to include detailed physics like the non-equilibrium ionization effect [e.g. Imada et al., 2011]. Flares similar to solar flares have been observed from many stars and other astrophysical objects [e.g. Güdel, 2004; Koyama et al., 1996; Tsuboi et al., 1998], and solar flare models have been applied to those astrophysical flares [e.g. Hayashi et al., 1996; Machida and Matsumoto, 2003; Masada et al., 2010; Shibata and Yokoyama, 2002]. Our pseudo-2D MHD model will provide a powerful method to explore these flares with different plasma parameters. These will be our future work.

Chapter 4

Above-the-loop-top Oscillation and Quasi-periodic Coronal Wave Generation in Solar Flares

4.1 Background

In this chapter, the oscillations excited in flaring regions will be investigated in detail using 2D MHD simulations.

Observations have revealed that various magnetohydrodynamic (MHD) waves are commonly associated with solar flares. Because coronal waves have potential to tell us about the local plasma condition which is difficult to directly observe, various techniques of MHD coronal seismology have been developed [Aschwanden and Schrijver, 2011; De Moortel and Pascoe, 2012; Van Doorselaere et al., 2008].

Various kinds of oscillations excited in solar flare regions have been investigated from emissions and imaging observations [Liu and Ofman, 2014; Nakariakov and Melnikov, 2009; Wang et al., 2003]. Quasi-periodic pulsations (QPP) in the flare emissions with periods ranging from fractions of seconds to several minutes are commonly observed in a wide range of wavelengths [Nakajima et al., 1983; Nakariakov and Melnikov, 2009]. Recent observations by the Atmospheric Imaging Assembly (AIA; Lemen et al. [2012]) on the *Solar Dynamics Observatory* (SDO; Pesnell et al. [2012]) have found that fast mode MHD waves are quasi-periodically emitted from some flaring sites (quasi-periodic propagating fast mode magnetoacoustic waves; QPF) [Liu et al., 2011]. The high sensitive monitoring observations by AIA enable us to study the wave properties in some events in detail [Liu et al., 2012; Yuan et al., 2013], although the statistical

characteristics remains still unclear. The observed period ranges from a few 10 sec to a few 100 sec.

QPP are also found in stellar flare emissions [Balona et al., 2015; Mathioudakis et al., 2003]. The solar coronal seismology has been applied to stellar flares to estimate the physical parameters of unresolved stellar coronae [Mitra-Kraev et al., 2005; Nakariakov et al., 2004]. The coronal seismology has potential to provide a powerful tool to investigate the stellar magnetic activity which is difficult to explore from direct imaging observations. Thus, advancing our understanding of oscillations in flares will have a great impact on both the solar and stellar physics.

Both of QPP and QPF imply a cyclic disturbance originating from the flaring sites. In addition, it has been pointed out that there will be a relationship between the generation of QPF and the time variability of the flare energy release (so QPP) [Liu et al., 2011, 2012; Shen and Liu, 2012; Yuan et al., 2013]. However, the physical mechanisms of QPP and QPF remain puzzling.

Models have been developed to investigate the dynamical properties of QPF. Ofman et al. [2011] utilized a three-dimensional (3D) active region model in which periodic velocity perturbations at the photospheric level are introduced, and obtained QPF whose property is similar to that of observed QPF. Pascoe et al. [2013] and Nisticò et al. [2014] studied impulsively generated fast mode waves in a magnetic funnel geometry, and found that their dispersive nature can lead to the formation of a quasi-periodic wave train. Yang et al. [2015] showed that isotropic QPF-like waves generated by multiple plasmoid ejections (see also Yokoyama [1998]).

In Chapter 3, we succeeded to perform a magnetohydrodynamics (MHD) simulation of a flare with a high spatial resolution. By performing a set of simulations, we discovered the local oscillation above the loops filled with evaporated plasma (above-the-loop-top region) and the generation of quasi-periodic coronal waves (QPF) from such oscillating region. Our model includes essential physics for solar flares, such as magnetic reconnection, heat conduction, and chromospheric evaporation, in contrast to all the previous models for coronal waves. The new model unveiled that flare loops and the above-the-loop-top region are full of shocks and waves, which is different from the previous expectations based on a standard flare model and is not found in previous simulations by Yokoyama and Shibata [1998]; Yokoyama et al. [2001a]. With the high spatial resolution, we for the first time revealed that QPF can be spontaneously excited by the above-the-loop-top oscillation. Here, we will report the new picture about the generation of QPF associated with solar flares, and will briefly discuss a possible relationship between QPF and QPP.

4.2 Numerical Model

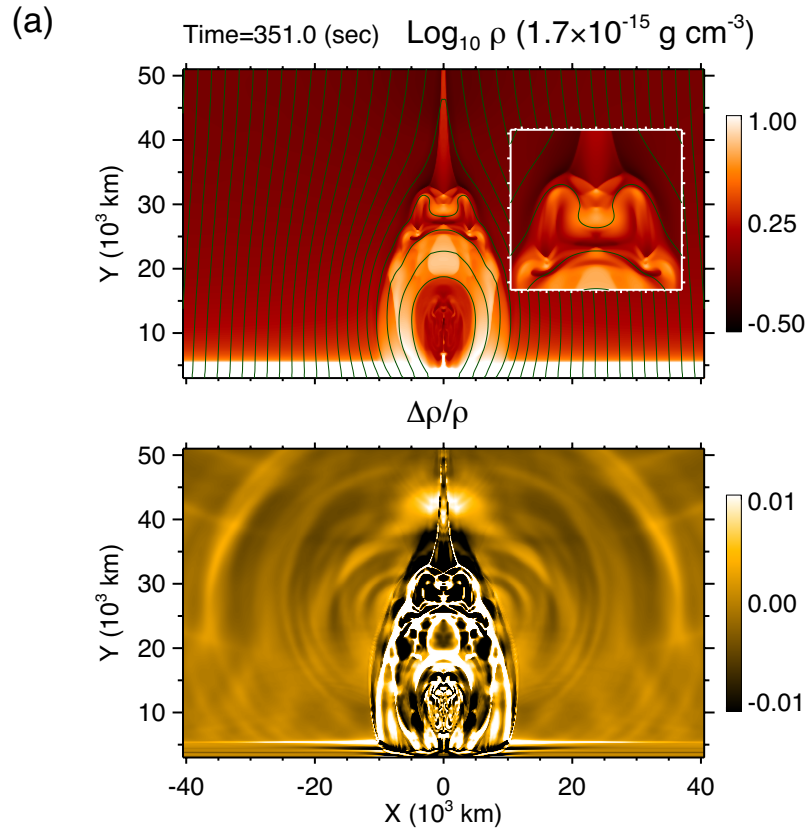
Our model is identical to our previous flare model in Chapter 3 except for the horizontal domain size. The calculated domain is $0 \leq x \leq x_{\max}$ and $0 \leq y \leq y_{\max}$, where $x_{\max} = 9 \times 10^4$ km and $y_{\max} = 6 \times 10^4$ km, respectively. This domain is resolved with a uniform 1200×800 grid. The center of the initial current sheet is located at the left boundary, where a reflecting boundary condition is applied. Our model includes essential physics for solar flares, such as magnetic reconnection, heat conduction, and chromospheric evaporation. The model atmosphere consists of a cool dense layer (chromosphere) and a hot tenuous layer (corona). The initial magnetic field is assumed to be a force-free field. The initial gas pressure is assumed to be uniform. The initial plasma β , defined as the ratio of the gas pressure to the magnetic pressure, is a free parameter. We examined the cases of $\beta = 0.06, 0.08, 0.1, \text{ and } 0.2$. To allow the magnetic field to reconnect, we impose a localized resistivity. The localized resistivity is fixed in time and space to realize a fast and quasi-steady magnetic reconnection with a single X-point [e.g. Ugai, 1992], which means that we neglect the oscillations caused by plasmoids and focus on the oscillations excited by a quasi-steady reconnection outflow. The thermal conductivity is set to the value three times smaller than the Spitzer value. The numerical scheme is based on a Harten-Lax-van Leer (HLL) scheme developed by Miyoshi and Kusano [2005], HLLD, which is a shock-capturing scheme.

4.3 Numerical Results

4.3.1 Evolution of Flare Loops and Emission of Coronal Waves

In this Chapter, the case with $\beta = 0.08$ is mainly mentioned as a typical example of our simulations. Figure 4.1(a) shows snapshots of the simulated flare. The domain where $x < 0$ is also shown only for visual inspection. The global evolution of the flare is essentially the same as that of our previous simulation: The reconnected magnetic field drives the Alfvénic outflow, and the plasma in the reconnection outflow is heated at the slow mode MHD shocks (slow shocks) emanating from the localized reconnection region [Petschek, 1964]. The reconnected fields pile up and form a loop system, which can be then filled with the hot dense plasma coming from the chromosphere (chromospheric evaporation). The loops filled with evaporated plasma will correspond to the soft X-ray flare loops. In this Chapter, the region above the loops filled with evaporated plasma is called “above-the-loop-top region” (an enlarged image of this is shown in Figure 4.1(a)).

The normalized running difference image of the density, $\Delta\rho/\rho$, clearly shows that



(b) **Observation**

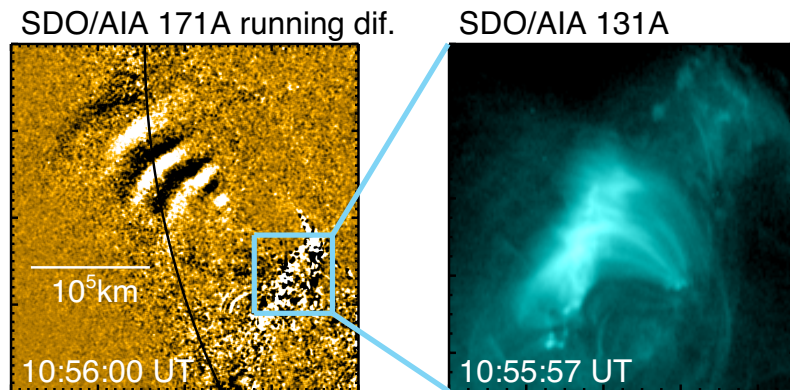


Figure 4.1: Quasi-periodic propagating fast mode magnetoacoustic waves (QPF) in our simulation ($\beta = 0.08$). Top: Density map at time=349.2 sec from the start. The solid lines denote magnetic field lines. An enlarged image of the above-the-loop-top region is also displayed. Middle: The normalized running difference of the density $\Delta\rho/\rho$, defined as $(\rho(t) - \rho(t - \Delta t))/\rho(t)$, where $\Delta t = 1.8$ sec. Bottom: Observational example of QPF accompanied with a GOES C2.8 flare which occurred on 30 May 2011.

isotropic waves are recurrently emitted from the above-the-loop-top region (detailed analysis will be given later). The propagation speed is identical to the fast mode MHD waves (fast waves) speed, indicating that they are fast waves. Figure 4.1(b) displays an observational example of QPF events accompanied with a GOES C2.8 flare which occurred on 30 May 2011 [this event was studied in detail by Yuan et al., 2013]. The images were taken by Atmospheric Imaging Assembly (AIA) [Lemen et al., 2012] on board Solar Dynamics Observatory (SDO) [Pesnell et al., 2012]. The flare region showed a clear cusp-shape loops (the 131 Å channel contains the Fe XXI line, formed at 11 MK, which is dominant in flaring regions, while it also contains lower temperature lines such as Fe VIII line, formed at 0.4 MK). Fast waves are quasi-periodically emitted from the flaring site during its rising phase, with a period of a few 10 to 100 s. These observational characteristics are similar to the simulation, although the observed anisotropic propagation of fast waves are not found in the simulations (this is probably because the coronal field structure is too simplified in our model).

4.3.2 Multiple Termination Shocks and New Picture of Flare Loops

Since shocks in the above-the-loop-top region play an important role in the generation of coronal fast waves, we will first mention the shock structure in detail. Fast mode MHD shocks (fast shocks) are formed well above the loops filled with the evaporated plasma as a consequence of the termination of the reconnection outflow (see the top row of Figure 4.2). In a standard flare model, a standing, horizontal fast shock is expected to be formed at the termination site, and often referred to as a “termination shock” [e.g. Priest and Forbes, 2002]. However, the simulation shows that a V-shaped pattern is formed by two oblique fast shocks, and later two oblique and a single horizontal fast shocks, which is very different from the standard picture. The two fast shocks sometimes reflect in above-the-loop-top region. The “multiple termination shocks” are also reported in Chapter 3.

The two oblique shocks are formed in the following manner. The kinetic energy of the reconnection outflow is thermalized in the above-the-loop-top region. In addition, the magnetic fields are piled up there. For these reasons, the total pressure p_{tot} (gas pressure plus magnetic pressure) in the above-the-loop-top region is larger than the total pressure in the outflow (see the bottom row of Figure 4.2). As the outflow enters the above-the-loop-top region, ambient total pressure compresses the outflow. The external compression is caused by the two oblique fast shocks inclined at an angle to the flow. This situation is very similar to the situation often referred to as “overexpansion” in

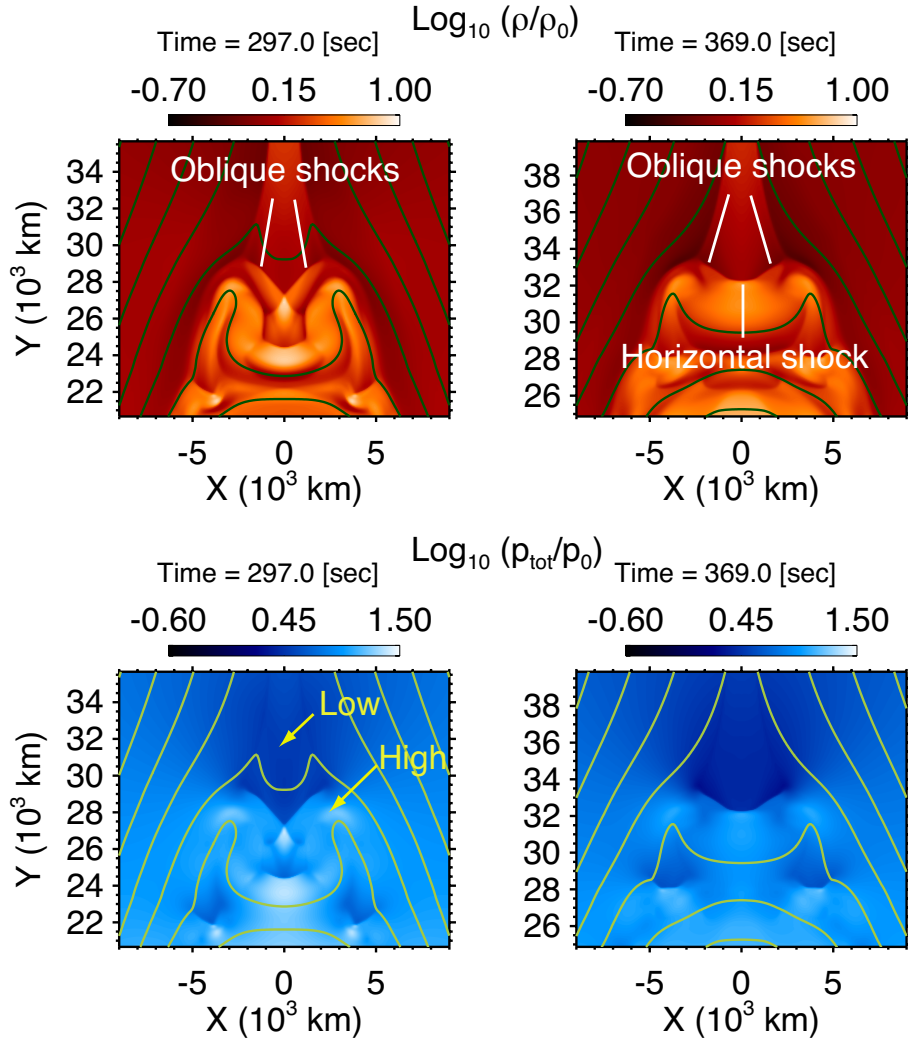


Figure 4.2: Snapshots of the above-the-loop-top region. Top row: Density distribution. Oblique and horizontal fast shocks are indicated. Bottom row: Total pressure (gas pressure plus magnetic pressure) distribution. Note that the total pressure in the reconnection outflow is smaller than that of the above-the-loop-top region. Solid lines denote magnetic field lines.

the fluid dynamics [Wilson and Falle, 1985], except for the existence of magnetic field.

Heat conduction has an effect to make plasma soft: heat conduction can reduce the pressure enhanced by compression, by transporting the heat elsewhere. For this reason, the push by ambient total pressure becomes weaker in the case with heat conduction than in the case without it, leading to the formation of more vertical oblique shocks. We consider that this makes the appearance of the horizontal fast shock difficult in the cases with heat conduction. We confirmed that without heat conduction, a horizontal fast shock appears at almost the same time when two oblique fast shocks are formed. The effects of heat conduction on the fast-mode Mach number of the reconnection outflow jet will be briefly discussed in Appendix A.4.

We tracked a specific field line to see the history of the passage through the multiple termination shocks. The left panels of Figure 4.3 display snapshots of the temperature and density at a time when the shock reflection occurs. The right panels show the time-sequenced images obtained along the tracked field line. The slow and fast shocks which the field line passed are also indicated. One will find that the field line in $x > 0$ always crosses more than two shocks during the period between ~ 302 s and 315 s. It is also clear that the distance between the slow shock (attached to the reconnection outflow) and the topmost oblique fast shock becomes smaller as time progresses (indicated by arrows in the density map). Finally, we note that the temperature ahead the topmost oblique fast shocks is enhanced. Since magnetic fields cross the shocks vertically, the heat released at the multiple termination shocks is transported along field lines to the upstream of the shocks by heat conduction. The importance of these findings will be discussed in Section 4.4.

We summarize a global picture of simulated flare loops in Figure 4.4. This figure is based on the results of Chapter 3, and will correspond to an update of the picture based on the standard flare model and Yokoyama and Shibata [1998]. A noticeable point is that shocks are formed at different places and affect the density structure. Important features in this study are found in the above-the-loop-top region: oblique fast shocks (multiple termination shocks), backflow of the reconnection outflow, and “magnetic tuning fork”, where the magnetic tuning fork denotes a pair of the sharply bent magnetic field structures in the above-the-loop-top region and will be mentioned in detail later.

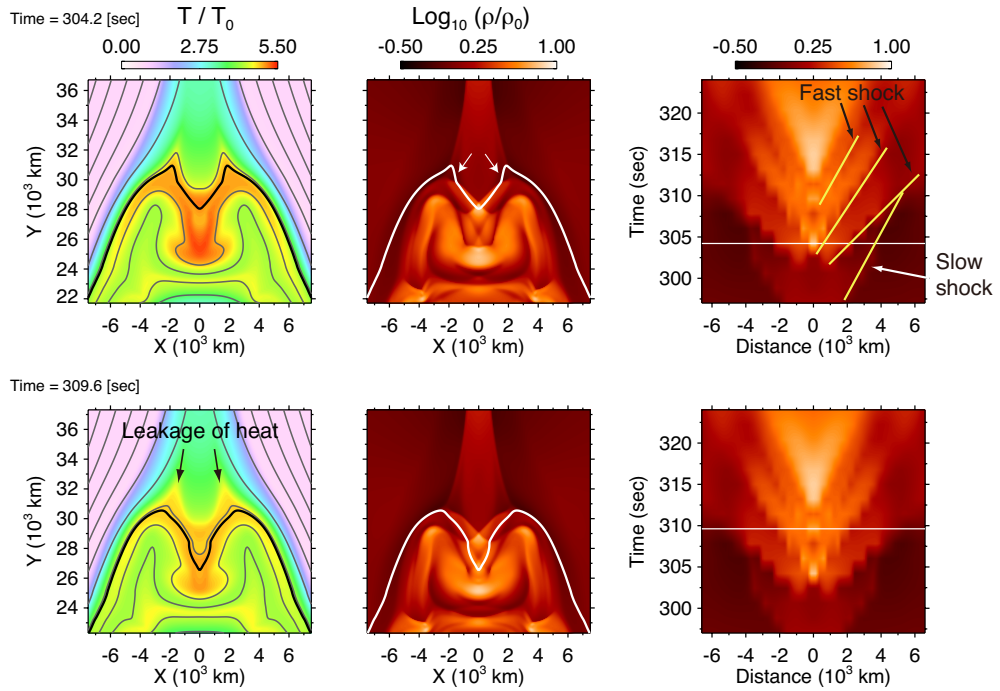


Figure 4.3: Passage of a specific field line through the multiple termination shocks. Left panels: Snapshots of the temperature and density distributions of the above-the-loop-top region. Black field line in the temperature map and white field line in the density map denote the same field line. Right panels: Time-sequenced images obtained along the tracked field line (density). The white solid lines denote the timings of the snapshots in the left panels. The shocks which the field line crosses in the region $x > 0$ are denoted by the yellow solid lines. The segments between a slow shock and a fast shock are indicated by arrows in the density map.

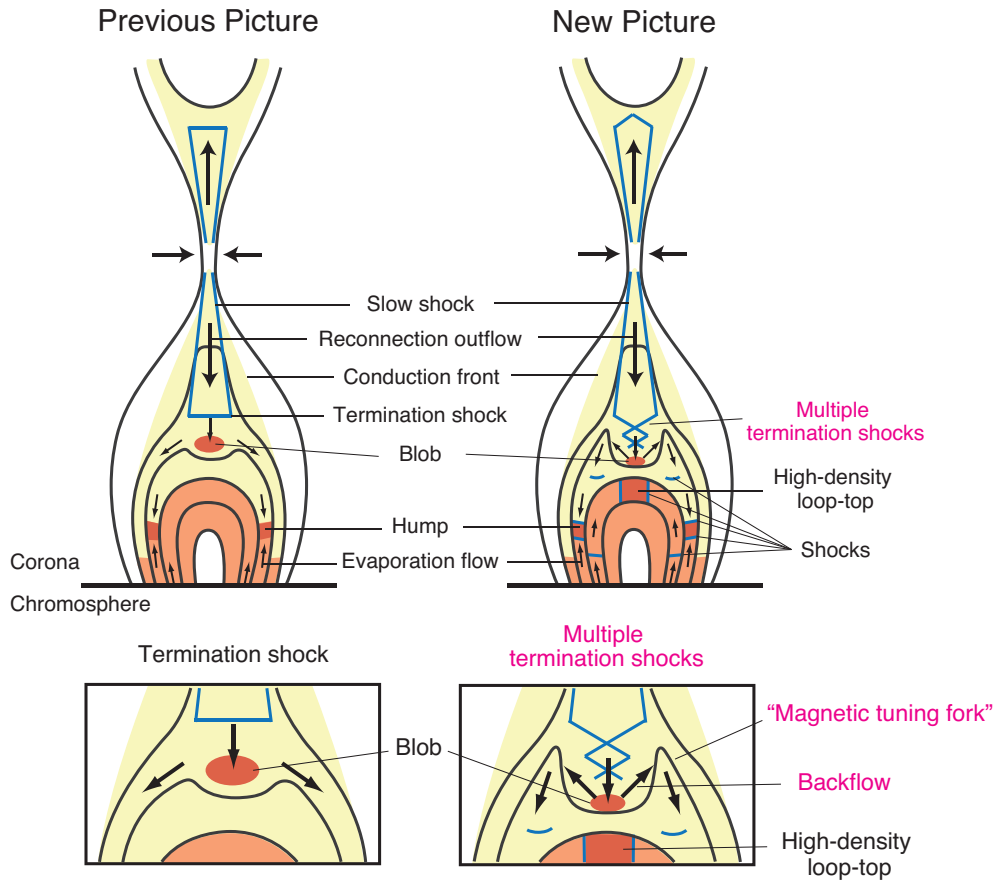


Figure 4.4: Comparison of a previous picture of flare loops based on a standard flare model and [Yokoyama and Shibata \[1998\]](#) model (Left) with a new picture based on our simulations (Right). Black solid lines denote magnetic field lines. Pale orange regions denote evaporated plasma. Orange regions indicate dense regions. Pale yellow regions denote regions inside the conduction fronts. Blue solid lines indicate shocks. Flows are denoted by arrows. A detailed description of the new picture is given in [Takasao et al. \[2015\]](#). Enlarged images of the above-the-loop-top regions are displayed at the bottom.

4.3.3 Above-the-loop-top Oscillation

Looking at the temporal evolution, we found that the distance of the two arms of the magnetic fork changes quasi-periodically. The oscillation is displayed in Figure 4.5. The left panels show snapshots of the plasma β distribution of the above-the-loop-top region. The right panels show time-sequenced images of plasma β and normalized running difference of the total pressure $\Delta p_{tot}/p_{tot}$ obtained along the slit shown in the left panels. The slit is positioned so that its y -coordinates is 68 km below the interaction point of the two oblique fast shocks. It is shown that the two arms of the magnetic tuning fork, seen as the two narrow high- β regions at the left and right edges, are oscillating with a period of ~ 40 sec (top and bottom rows show the timings when the two arms are closed and open, respectively). This oscillation is hereafter called the “above-the-loop-top oscillation”.

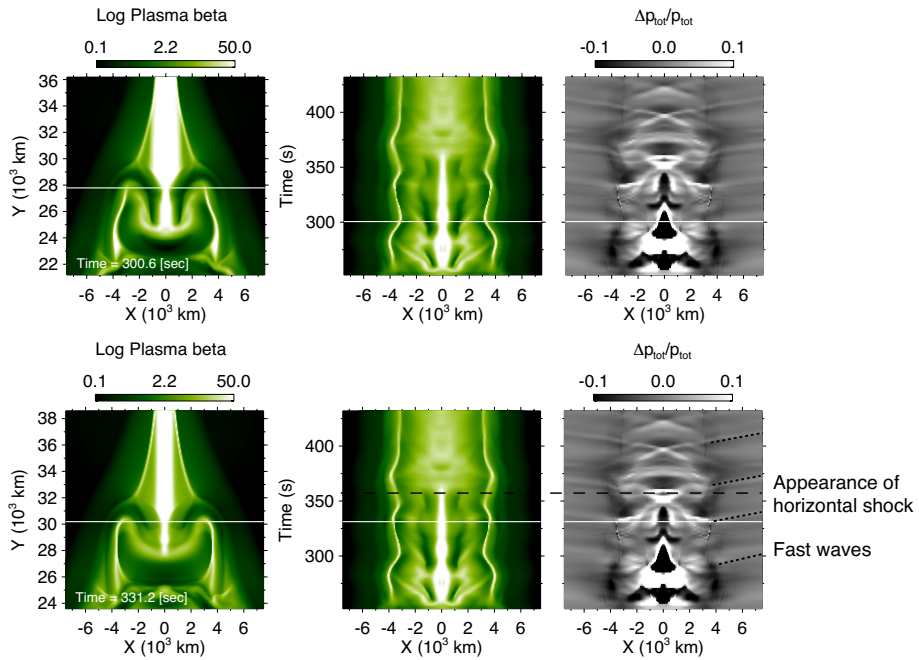


Figure 4.5: Above-the-loop-top oscillation (the initial β is 0.08). Left: Snapshots of the distribution of $\log_{10} \beta$ of the above-the-loop-top region. Right: Time-sequenced images of $\log_{10} \beta$ and $\Delta p_{tot}/p_{tot}$ obtained along the slit shown in the left panels. The slit used is positioned so that its y -coordinates is 68 km below the interaction point of the two oblique shocks. The horizontal lines in the time-sequenced images denote the timings of the snapshots in the left panels.

Figure 4.5 also shows that outward-propagating fast waves are quasi-periodically excited when the outward motion of the arms of the magnetic tuning fork terminates (see the time-sequence images of $\Delta p_{tot}/p_{tot}$). These fast waves are what we have already seen in Figure 4.1. A notable point is that the wave source is localized in the above-the-loop-top region, and very small compared to the system size (less than 10% of the system size in this simulation).

A snapshot of the simulation and a schematic illustration of the above-the-loop-top oscillation are shown in Figure 4.6. When the reconnection outflow impacts on the strong magnetic field region, the flow pattern changes, resulting in backflow (Figure 4.6(a)). See also Figure 4.4). The backflow (more exactly, the gradient of the dynamic pressure by backflow) pushes the arms of the magnetic tuning fork outward, and compresses the magnetic field of the arms. This leads to the generation of outward-propagating fast waves (Figure 4.6(b)). See also the time-sequenced images in Figure 4.5). Once the magnetic field there becomes strong enough to overcome the backflow, the arms start to move inward, generating inward-propagating fast waves. Although the inward-propagating waves decelerate the backflow, the speed of the backflow quickly recovers, because the speed of the reconnection outflow is almost constant with time. Thus, the same process repeats and the oscillation is maintained. We note that the generation process of fast waves by the oscillating magnetic tuning fork is similar to the generation process of sound waves by an oscillating tuning fork. The “magnetic tuning fork” is named so after its similarity to an oscillating tuning fork.

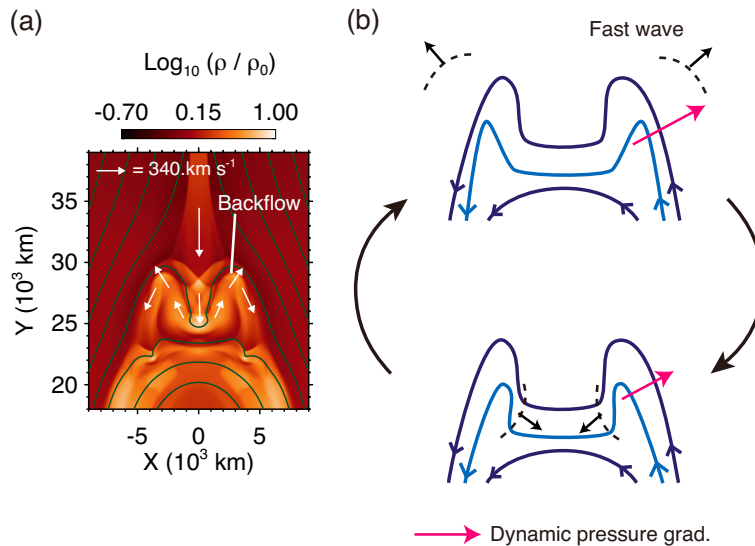


Figure 4.6: (a) Backflow of the reconnection outflow in the above-the-loop-top region. (b) Schematic illustration of the above-the-loop-top oscillation.

The oscillation stops when a horizontal fast shock appears in between the two oblique fast shocks (see Figure 4.2). The timing of the appearance is also indicated in Figure 4.5. The horizontal shock more significantly decelerates the reconnection outflow than oblique shocks. Therefore, the backflow of the reconnection outflow, which is essential to maintain the oscillation, becomes slow after the formation of the horizontal shock, leading to the disappearance of the oscillation.

The above-the-loop-top oscillations causes the oscillation of the oblique fast shocks. The temporal evolution of the ratio of the pressures ahead (p_a) and behind (p_b) one of the oblique shocks is shown in the left panel of Figure 4.7 (solid) as an indicator of the shock strength. It can be seen that the shock strength is oscillating with a period of ~ 40 s, identical to the period of the above-the-loop-top oscillation. The maximum of the horizontal component of the backflow is also shown (dashed). The quasi-periodic deceleration of the backflow is caused by the inward-propagating fast waves which are excited by the inward motion of the arms of the magnetic tuning fork (see Figure 4.6(b)). The right panel displays the wavelet analysis of the coronal fast waves. The normalized running difference of the density $\Delta\rho/\rho$ at the position $(x, y) = (1.5 \times 10^4 \text{ km}, 3.9 \times 10^4 \text{ km})$ (outside the flare loop) is used. A strong power is found at a period of ~ 40 s, very similar to the period of the above-the-loop-top oscillation. This indicates that QPF are generated by the above-the-loop-top oscillation. We also

note that the shock reflection occurs when the inward-propagating fast waves compress the U-shaped magnetic fields between the arms of the magnetic tuning fork.

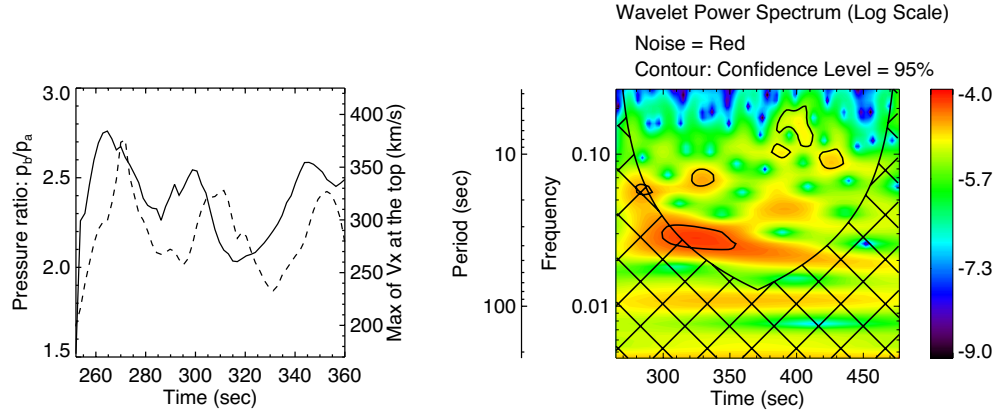


Figure 4.7: Relation between the above-the-loop-top oscillation and coronal waves (a) Temporal evolution of the ratio of the pressures ahead (p_a) and behind (p_b) a topmost oblique shock (solid) and the maximum of the horizontal component of the backflow (dashed). (b) Wavelet analysis of the coronal fast waves. The running difference of the density at the position $(x, y) = (1.5 \times 10^4 \text{ km}, 3.9 \times 10^4 \text{ km})$ is used.

4.3.4 Dependence on Magnetic Field Strength

The dependence of the oscillation period on the initial plasma β (equivalently, magnetic field strength) is investigated. From the left panel of Figure 4.8(a), it is found that the period is proportional to the plasma β . The right panel shows the dependence of the backflow speed. As an indicator of the backflow speed, we used the time-averaged maximum of the horizontal component of the backflow velocity in the above-the-loop-top region. The time-averaging is performed during 72 s after the formation of the oblique fast shocks. The figure indicates that it scales as $0.45V_{A,0}$, where $V_{A,0}$ is the initial Alfvén speed in the corona. This means that the backflow speed is of the order of the Alfvén speed. This Alfvénic backflow drives the above-the-loop-top oscillation. The reason why the backflow behind the multiple termination shocks is Alfvénic is that the deceleration by oblique shocks is inefficient.

Figure 4.8(b) compares the case with $\beta=0.06$ (Left, strong magnetic field) and the case with $\beta=0.2$ (Right, weak magnetic field), indicating that the vertical size of the above-the-loop-top region is smaller when the magnetic field is stronger. The size is smaller in the case with a stronger coronal field, because the coronal magnetic field

confines the backflow.

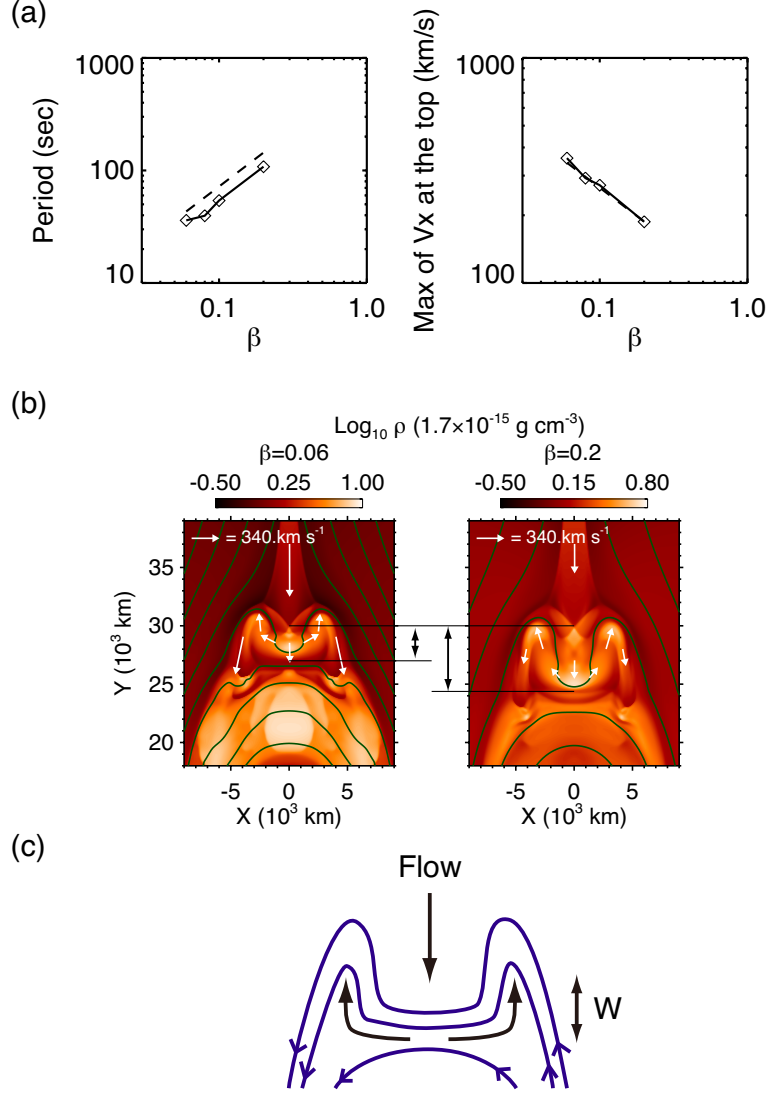


Figure 4.8: Plasma β dependence of the oscillatory property. (a) Plasma β dependence of the period (Left) and the maximum of the horizontal component of the backflow (Right). The period is estimated from the time interval between the initial and second peaks seen in the pressure ratio p_b/p_a . In the left panel, the dashed line indicates the slope $\propto \beta$. In the right panel, the dashed line denotes $0.45V_{A0}$. (b) Comparison of the cases with $\beta = 0.06$ (Left) and $\beta = 0.2$ (Right). The vertical sizes of the above-the-loop-top region are compared. (c) Schematic illustration of the plasma flow in the termination region. w denotes the vertical size of the magnetic tuning fork.

What determines the oscillation period? Because the oscillation is driven by the backflow, the period of the oscillation P will be proportional to w/v_{bf} , where w is the length scale of the above-the-loop-top region and v_{bf} is the backflow speed. As shown in Figure 4.8(a), $v_{\text{bf}} \sim V_{A,0} \propto B$. The vertical size of the above-the-loop-top region is determined so that the magnetic fields accumulated and compressed by backflow at the top of the arms of the magnetic tuning fork are strong enough to confine the backflow. Considering this, the vertical size and the magnetic field strength B are related through the conservation of magnetic flux, $Bw = \text{const.}$, where we take w as the vertical size of the above-the-loop-top region (Figure 4.8(c)) This gives $w \propto B^{-1}$. Finally, we obtain the following scaling relation:

$$P \sim \frac{w}{v_{\text{bf}}} \propto B^{-2} \propto \beta, \quad (4.1)$$

which is consistent with the numerical results. This explains why the oscillation period is shorter in the case with a stronger coronal field.

4.4 Discussion

We carried out MHD simulations of a solar flare in which essential physics for solar flares such as magnetic reconnection, heat conduction, and chromospheric evaporation are included. Our model unveiled that flare loops and the above-the-loop-top region are full of shocks and waves. From our simulations, we discovered the local oscillation of above-the-loop-top region (above-the-loop-top oscillation) and the generation of quasi-periodic propagating fast mode magnetoacoustic waves (QPF) from such oscillating region. It was found that the above-the-loop-top oscillation is controlled by the backflow of the reconnection outflow in the above-the-loop-top region. This means that the wave source is localized and very small compared to the flare loop size (less than 10% of the flare loop size). It was revealed that the termination shock structure has a significant impact on the maintenance and stop of the oscillation. The generation process of QPF is found to be similar to the sound wave generation by an oscillating tuning fork.

Many previous models for QPF do not clearly specify the physical origins of excitors of coronal waves, and have been used for the investigation of the propagation and dispersive nature of waves of interest [e.g. [Ofman et al., 2011](#); [Pascoe et al., 2013](#)]. Using MHD simulations, we revealed that the reconnection outflow (more exactly, the backflow of the outflow) can act as an exciter of coronal waves. We also showed that waves can be spontaneously generated even with a quasi-steady reconnection outflow.

It may be possible that a time-dependent and oscillatory reconnection process also leads to the generation of QPF [Kliem et al., 2000; McLaughlin et al., 2009; Murray et al., 2009]. It is claimed on the basis of 2D MHD simulations that the quasi-periodic ejection of plasmoids could also lead to QPF [Yang et al., 2015; Yokoyama, 1998]. However, the behavior of reconnection in 3D remains poorly understood. The initial magnetic field configuration may also affect the oscillation processes. We will investigate the influence of the 3D reconnection in a more realistic magnetic configuration in our future studies.

Previous studies of flare loop oscillations mainly focus on the standing (M)HD waves in loops [see a review by Nakariakov and Melnikov, 2009]. In this study, however, we discovered a cyclic process which is controlled by the flow confined on the above-the-loop-top region, not by any standing waves. This finding has a significant impact on the interpretation of oscillations. For instance, if we consider that oscillation is caused by a standing acoustic wave [Nakariakov et al., 2004], the period can be interpreted as

$$P \propto \frac{L}{C_s} \propto LT^{-1/2} \propto B^{-3/7} L^{6/7} \propto B^{-0.43}, \quad (4.2)$$

where $C_s \propto T^{1/2}$ is the sound speed, and we used the scaling law of the flare temperature ($T \propto B^{6/7} L^{2/7}$) by Yokoyama and Shibata [1998]. Here we only focus on the dependence on the magnetic field strength for clarity. However, in the case of the above-the-loop-top oscillation, the period can be written as

$$P \propto \frac{w}{v_{\text{bf}}} \propto \beta \propto B^{-2}, \quad (4.3)$$

which gives a different scaling. Hence, it is crucial to correctly identify the oscillation mechanism before one derives the physical parameters from observations. The development of methods to distinguish various kinds of oscillations including the above-the-loop-top oscillation is required. This will greatly advance the solar and stellar coronal seismology.

Shibata and Yokoyama [2002] developed a theory to estimate the physical parameters of solar and stellar flares from the observable parameters (the emission measure and the temperature), on the basis of the results of MHD simulations of a solar flare by Yokoyama et al. [2001a]. Their theory is based on a reconnection model for flares, and is derived under the assumption that the pressure in the flare loops is balanced with the magnetic pressure outside. We derived a scaling relation of the oscillation period on the basis of similar MHD simulations. Our scaling relation and their theory are both based on the reconnection physics, but describe different aspects of flares.

Therefore, a combination of both our scaling relation and their theory will provide a powerful reconnection-based method to diagnose the solar and stellar coronae.

We found that the termination shocks are also quasi-periodically oscillating because of the above-the-loop-top oscillation (Figure 4.7). It has been argued that termination shocks could be a promising site for particle acceleration [Chen et al., 2015; Nishizuka and Shibata, 2013; Tsuneta and Naito, 1998], and could be related to the above-the-loop-top hard X-ray source [Krucker et al., 2010; Masuda et al., 1994; Oka et al., 2015]. If this is true, the quasi-periodic oscillation of the multiple termination shocks found in this study could lead to QPP in the nonthermal emissions through the quasi-periodic variation of the efficiency of particle acceleration. QPP in the nonthermal emissions have been commonly observed during flares [Aschwanden, 2002; Nakariakov and Melnikov, 2009], but the origin has been puzzling. Our study could provide a possible solution for this. In addition, the simulations showed that the oscillation of the multiple termination shocks and QPF can have a common origin. On the basis of this, we suggest a new picture in which QPF and QPP in the nonthermal emissions have a common origin. Thermal emissions may also respond to the variation of the efficiency of acceleration through thermalization of nonthermal particles, showing QPP.

We showed that a field line can simultaneously cross multiple shocks when it passes through the multiple termination shocks (Figure 4.3). This indicates that one can expect more chances for particle acceleration at the shocks than the case with a single horizontal termination shock which is commonly assumed in the standard flare model. The segment between a slow shock and a topmost fast shock (indicated in the density map of Figure 4.3) could be a good site for the Fermi acceleration, because these shocks are approaching each other. It is also found that the temperature in the upstream of the topmost oblique fast shocks (including the segments between a slow shock and a fast shock) is enhanced by heat conduction (indicated in the temperature map of Figure 4.3). For an efficient particle acceleration, the preheating of plasma before the acceleration at termination shocks may be necessary. Tsuneta and Naito [1998] considered that the heating by the slow shocks attached to the reconnection outflow will provide a method for preheating. We consider that the leakage of the heat released at the multiple termination shocks will also contribute to the preheating.

Chapter 5

Concluding Remarks

Here I will overview future prospects of the main topics dealt with in this thesis.

The list below summarizes several keywords regarding remaining, important problems of the formation of flare-productive active regions:

- Influence of convection
- Process toward the onset of a flare
- Origin of satellite spots
- Effects of partial ionization

In Chapter 2, it is shown that the photospheric magnetic structure as a result of the emergence of a highly-twisted flux tube is qualitatively consistent with observations. However, the flux emergence process can be affected by convection [Cheung and Isobe, 2014]. Hence, 3D MHD simulations including convections are necessary for better understanding the formation process.

Active regions live typically for a month or so. During their lifetime, the magnetic structure will greatly change due to magnetic reconnection and convective motions. To understand the process towards the onset of flares in evolving active regions, longer-term calculations in a large domain size will be required.

Satellite spots are often found around sunspots and known to play an important role in inducing flares [Shimojo et al., 1998; Takasaki et al., 2004]. They are small, but can destabilize the system and cause large flares [Chen and Shibata, 2000]. In spite of their importance, their origin remains unclear. For understanding fundamental processes towards the onset of a flare, this should be investigated.

It has been argued that the emergence of magnetic flux will be significantly affected by the effects of partial ionization which will be important in the lower chromosphere

[Arber et al., 2007; Leake and Arber, 2006]. Leake and Linton [2013] claimed that the effects of partial ionization will lead to a reduction of up to $\sim 90\%$ in the amount of sub-surface plasma brought up into the corona. This result could affect the submergence process found in Chapter 2. Therefore, further investigation using a model that includes the effects of partial ionization will be necessary.

For the energy release of solar flares, important keywords will be as follows:

- Observations of shocks and the above-the-loop-top regions
- 3D plasmoid-dominated reconnection
- Oscillations excited in flare loops
- Particle acceleration

We clarified that shocks significantly affect the thermal structure of flare loops through compression and acceleration of plasma. In spite of a long history of the solar flare observation, the thermal structure of flare loops has not been fully understood. One of the reason for this will be attributed to the difficulty of observations of shocks. Recent observations of solar flares have begun to find signatures of shocks in flare regions [Chen et al., 2015; Guidoni et al., 2015; Hara et al., 2011]. Future high-spatial and temporal resolution observations will reveal more shocks in and above flare loops, and relationship between shocks and distinct structures seen in flare regions.

Our findings of the above-the-loop-top oscillation emphasize the importance of high-spatial and temporal observations of the above-the-loop-top regions. Simultaneous detection of the variation of the flow speed in the above-the-loop-top region and coronal waves emitted from the flaring site will significantly help us understand the origin of the oscillations. Also, observations of (multiple) termination shocks will make our view of the shock structure more concrete. Since our study showed that the shock structure affects the oscillatory behavior (for instance, the above-the-loop-top oscillation will stop when a horizontal fast shock appears), observations of shocks will also contribute to the development of models for oscillations in flare regions.

Recent numerical simulations of 3D reconnection show that a current sheet becomes turbulent via the formation of multiple plasmoids (or flux ropes) [e.g. Nishida et al., 2013]. It has begun to be pointed out that the physics to determine the reconnection rate differs between 2D and 3D reconnection, but our knowledge on the physics of 3D reconnection is poor. The fundamental processes of 3D plasmoid-dominated reconnection should be investigated for understanding of the energy release during flares.

The excitation processes of various kinds of oscillations found in flare regions remain unclear. Previous studies of flare loop oscillations mainly focus on the standing (M)HD waves in loops. However, our study revealed that the above-the-loop-top region can be locally oscillated by the flow. The recently found turbulent, highly dynamic nature of 3D magnetic reconnection may also lead to oscillations of flare loops, although it is not clear if such turbulent process can actually result in a quasi-periodic oscillation. 3D MHD simulations of a flare including the effects of heat conduction in a more realistic magnetic configuration and atmospheric structure will be required to advance our knowledge. This will also lead to a great advance of the development of solar and stellar coronal seismologies.

Particle acceleration is ubiquitous in solar flares, but detailed processes remain puzzling. It has been claimed that termination shocks could be a promising site for particle acceleration [Chen et al., 2015; Nishizuka and Shibata, 2013; Tsuneta and Naito, 1998]. Recent observations have begun to find evidence of particle acceleration associated with plasmoid motions (Takasao et al. 2016, submitted). Since particle acceleration is also ubiquitous in astrophysics, revealing the acceleration processes in solar flares has a great impact. New theoretical models will have to consider the dynamic nature of magnetic reconnection and shocks found in this thesis.

Appendix A

Some notes of Solar Flare Simulations

A.1 Spitzer Conductivity

Imagine that two plasmas with different temperatures contact with each other at a surface with an area of S . The temperature difference will be smoothed out owing to the heat conduction by electrons (note that the contribution of protons is negligible due to their large mass). Heat conduction plays an essential role in determining the temperature of flares, so I will summarize the basic physics about this. The energy transfer rate by thermal electrons $\Delta E/\tau_{ei}$ can be given as

$$\frac{\Delta E}{\tau_{ei}} = \frac{n_e k_B \Delta T S l_{\text{mfp}}}{\tau_{ei}} \quad (\text{A.1})$$

where ΔT is the temperature difference, τ_{ei} is the typical timescale of electron-ion collision and l_{mfp} is the mean free path of electrons. Then, the heat conduction flux F_c

will be

$$F_c = \frac{\Delta E}{\tau_{ei} S} = \frac{n_e k_B \Delta T l_{\text{mfp}}}{\tau_{ei}} \quad (\text{A.2})$$

$$= \frac{n_e k_B l_{\text{mfp}}^2}{\tau_{ei}} \frac{\Delta T}{l_{\text{mfp}}} \quad (\text{A.3})$$

$$\simeq \frac{n_e k_B l_{\text{mfp}}^2}{\tau_{ei}} |\nabla T| \quad (\text{A.4})$$

$$\equiv \kappa_{sp} |\nabla T| \quad (\text{A.5})$$

where we call $\kappa_{sp} = n_e k_B l_{\text{mfp}}^2 / \tau_{ei}$ the Spitzer conductivity. Using the relations $\tau_{ei} = l_{\text{mfp}} / v_{\text{th},e}$ and $\sigma l_{\text{mfp}} n_i = \sigma l_{\text{mfp}} n_e = 1$ (where $v_{\text{th},e}$ is the thermal velocity of electrons, $n_i = n_e$ is the number density of ions and σ is a collision cross-section),

$$\kappa_{sp} = n_e k_B \frac{v_{\text{th},e}}{l_{\text{mfp}}} l_{\text{mfp}}^2 = n_e k_B v_{\text{th},e} l_{\text{mfp}} = \frac{k_B v_{\text{th},e}}{\sigma} \quad (\text{A.6})$$

The cross-section of the Coulomb collision $\sigma = \pi b^2$ can be roughly estimated by assuming that the potential energy is similar to the kinetic energy:

$$\frac{e^2}{b} \sim \frac{m_e v_{\text{th},e}^2}{2} \quad (\text{A.7})$$

$$b \sim \frac{2e^2}{m_e v_{\text{th},e}^2} \quad (\text{A.8})$$

Therefore we obtain

$$\sigma = \frac{4\pi e^4}{m_e^2 v_{\text{th},e}^4} \quad (\text{A.9})$$

If we carefully consider the long range nature of the Coulomb potential, the cross-section σ estimated above will be multiplied by a factor of $\ln \Lambda_C = 15-20$, called the Coulomb logarithm. Thus, we get the following form:

$$\kappa_{sp} = k_B v_{\text{th},e} \frac{m_e^2 v_{\text{th},e}^4}{4\pi e^4 \ln \Lambda_C} = \frac{2^{1/2} k_B^{2/7}}{\pi e^4 m_e^{1/2}} \frac{1}{\ln \Lambda_C} T^{5/2} \simeq 1.84 \times 10^{-6} \left(\frac{\ln \Lambda_C}{10} \right)^{-1} T^{5/2} \text{ incgs} \quad (\text{A.10})$$

where we used $v_{\text{th},e} = (2k_B T/m_e)^{1/2}$. It is shown that the temperature dependence of the conductivity is very strong, and therefore heat conduction becomes important during flares. Practically, it is known that the Spitzer conductivity is approximately 10 times smaller than the estimated value.

It is straightforward to apply this procedure to the case of heat conduction for neutral gas. Since the Coulomb force for neutral atoms becomes only important when they are very close to each other, we can treat them as a hard sphere with a radius of the Bohr radius $a_0 \sim 10^{-10}$ m = 10^{-8} cm. Hence the cross section for neutrals is replaced by $\sigma = \pi a_0^2$. The heat conductivity for neutral gas will be

$$\kappa_{sp,n} = \frac{k_B v_{\text{th},n}}{\pi a_0^2} = \frac{2^{1/2} k_B^{3/2}}{\pi a_0^2 m_n^{1/2}} T^{1/2} \quad (\text{A.11})$$

Note that the temperature dependence of the conductivity for neutrals is much weaker than that for plasma.

The idea shown here can be also used to estimate the viscosity. Just consider the momentum transfer instead of the heat transfer (i.e. $\Delta m/\tau = \rho \Delta v S l_{\text{mfp}}/\tau$), then one will find that the dependence of the viscosity on the temperature is exactly the same as that of the conductivity.

Note that the Spitzer conductivity is based on the assumption that the mean free path is shorter than the temperature scale length. When the mean free path becomes similar to or greater than the temperature scale length, the heat conduction flux will significantly deviate from the form of the Spitzer conductivity. This situation is often termed as “saturation” [e.g. Cowie and McKee, 1977]. The maximum heat conduction flux carried by electrons is the enthalpy flux $\sim n_e k_B T v_{\text{char}}$, where v_{char} is a characteristic velocity of electrons and it might be of the order of $v_{\text{th},e}$ [e.g. Parker, 1963]. Note that v_{char} depends on the distribution function of electrons [Manheimer and Klein, 1975]. If we take $v_{\text{char}} = v_{\text{th},e}$, then the maximum heat flux will be proportional to

$$n_e k_B T v_{\text{th},e} \sim \sqrt{\frac{m_i}{m_e}} \rho C_{s,i}^3 \quad (\text{A.12})$$

where we used $n_e k_B T = p \sim \rho C_{s,i}$ and $C_{s,i} = (k_B T/m_i)^{1/2}$ (the sound speed of ions). Conventionally, the following form is often taken as the saturated flux [e.g. Cowie and

McKee, 1977]:

$$F_{c,\text{sat}} = 5\phi_s\rho C_{s,i}^3 \quad (\text{A.13})$$

where ϕ_s is a constant that is of the order of unity. Following Cowie and McKee [1977], $\phi_s = 1.1$ for a fully ionized gas with cosmic abundances, and for $T_e \neq T_i$, ϕ_s must include the factor $[2T_e/(T_e + T_i)]^{3/2}$. I note that Longcope and Bradshaw [2010] claims using their two-fluid (electrons and ions) model that electrons are heated indirectly and thus carry a heat flux always well below the free-streaming limit.

A.2 Numerical Method of Heat Conduction in 2D MHD Model

We modify the time step splitting method to calculate the heat conduction flux by Yokoyama and Shibata [2001]. Using the MHD energy flux F_{mhd} and heat conduction energy flux F_c , we can write the energy equation as follows:

$$\frac{\partial E}{\partial t} + \nabla \cdot \mathbf{F}_{mhd} + \nabla \cdot \mathbf{F}_c = 0, \quad (\text{A.14})$$

where E is the total energy. The discretized form is

$$\frac{1}{\Delta t}(E^{n+1} - E^n) + (\nabla \cdot \mathbf{F}_{mhd})^{n+1/2} + (\nabla \cdot \mathbf{F}_c)^{n+1/2} = 0. \quad (\text{A.15})$$

First, we calculate the MHD part

$$\frac{1}{\Delta t}(E^* - E^n) = -(\nabla \cdot \mathbf{F}_{mhd})^{n+1/2}, \quad (\text{A.16})$$

where the superscript $*$ denotes the results of the MHD step. Then we calculate the heat conduction step

$$\frac{1}{\Delta t}(E^{n+1} - E^*) = -(\nabla \cdot \mathbf{F}_c)^{n+1/2}. \quad (\text{A.17})$$

The procedure mentioned above is the same as [Yokoyama and Shibata \[2001\]](#). The difference appears in the expression of the heat flux formula. The heat flux formulae in [Yokoyama and Shibata \[2001\]](#) are

$$\mathbf{F}_c \approx -\kappa_0(T^*)^{5/2} \frac{\mathbf{B}^*}{B^*} \left(\frac{\mathbf{B}^*}{B^*} \cdot \nabla T \right), \quad (\text{A.18})$$

$$F_{c,x} \approx -A_{xx}^* \frac{\partial T}{\partial x} - A_{xy}^* \frac{\partial T}{\partial y}, \quad (\text{A.19})$$

$$F_{c,y} \approx -A_{yy}^* \frac{\partial T}{\partial y} - A_{yx}^* \frac{\partial T}{\partial x}, \quad (\text{A.20})$$

$$A_{ab}^* = \kappa_0(T^*)^{5/2} \frac{B_a^* B_b^*}{(B^*)^2}, \quad (\text{A.21})$$

where the subscripts a and b denote x and y . The time and space discretization are, for example,

$$F_{c,x} \approx -A_{xx}^* \left(\frac{\partial T}{\partial x} \right)^{n+1} - A_{xy}^* \left(\frac{\partial T}{\partial y} \right)^* . \quad (\text{A.22})$$

We modify this to

$$F_{c,x} \approx -A_{xx}^* \left(\frac{\partial T}{\partial x} \right)^{n+1} - A_{xy}^* \left(\frac{\partial T}{\partial y} \right)^{n+1}. \quad (\text{A.23})$$

The difference of two formulae appears in the operator matrix of the implicit scheme used. The number of the non-zero components in one row is 5 in Equation (A.22), and 9 in Equation (A.23). Geometrically, in Equation (A.23) we use all the neighboring 8 grids around each point at $(n + 1)$ step to calculate the heat flux (Figure A.1). This method gives more accurate results than the previous method, particularly in the grid points where a magnetic field is largely bend and oblique to coordinate.

A.3 Analytical Approach to the Riemann Problem: Possible Solutions

We shall describe the exact solutions of the symmetric MHD Riemann problems that can appear in our pseudo-2D MHD model. In a symmetric MHD Riemann problem,

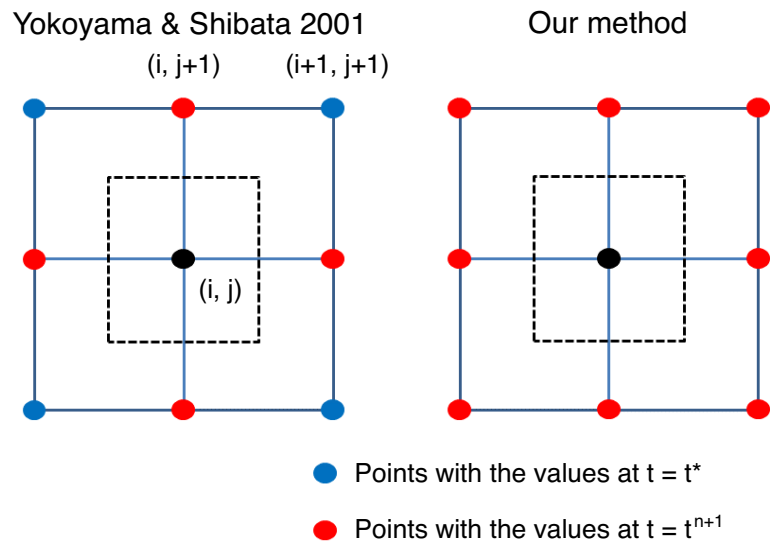


Figure A.1: The grid points used to calculate the heat flux for the grid (i, j) in [Yokoyama and Shibata \[2001\]](#) (Left) and our method (Right). The red and blue grids have the physical quantities at the time $t = t^{n+1}$ and those at $t = t^*$, respectively.

the initial states in the left and right hand side are assumed to be as follows.

$$\rho_L = \rho_R, \tag{A.24}$$

$$p_L = p_R, \tag{A.25}$$

$$B_{x;L} = B_{x;R}, \tag{A.26}$$

$$B_{y;L} = -B_{y;R}, \tag{A.27}$$

$$B_{z;L} = B_{z;R}, \tag{A.28}$$

$$\mathbf{v}_R = \mathbf{v}_L = 0, \tag{A.29}$$

where the subscripts L and R represent the left hand side and the right hand side, respectively.

Let us consider the situation without the guide field component ($B_{z;L} = B_{z;R} = 0$). Since the magnetic field vectors in the initial states are in the x - y plane, the rotational discontinuities will not appear in the solutions. Due to the initial discontinuity, one contact discontinuity, two slow shocks, and two fast rarefaction waves are generated.

From the jump condition across the contact discontinuity, the tangential magnetic field, B_y , should be equal to zero in the region between two slow shocks. Therefore, it is necessary to have either the switch-off slow shock (SS) or the switch-off fast rarefaction wave (FRW). In the former case (see the left panels of Figure A.2), the exact solution consists of the switch-off SS and FRW. On the other hand, in the latter case (the middle panels of Figure A.2), the exact solution consists of the pure hydro shock (HS) and switch-off FRW.

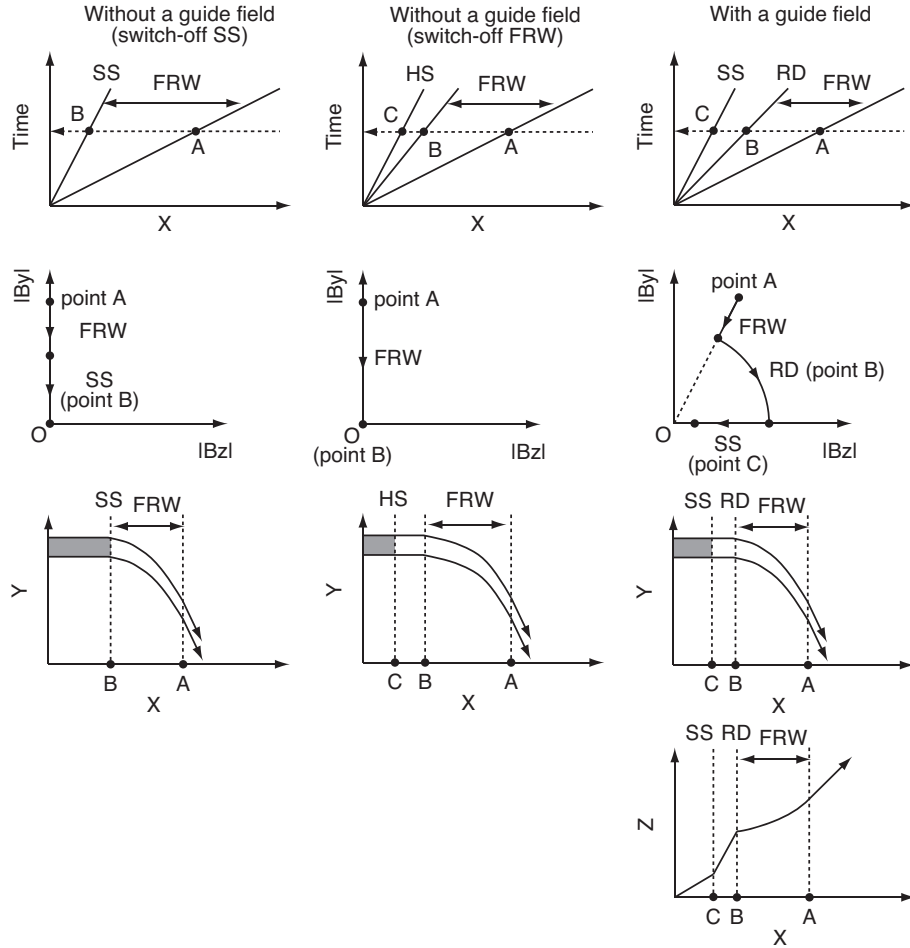


Figure A.2: Three possible solutions of the Riemann problem. Left column: Case without a guide field, where B_y is switched off by the slow shock (SS). Middle column: Case without a guide field, where B_y is switched off by the fast mode rarefaction wave (FRW). Right column: Case with a guide field, where the magnetic field is rotated by the rotational discontinuity (RD) and the magnetic energy is released at the slow shock (SS). First row: $x - t$ diagrams that show the Riemann fans. Second row: $|B_z| - |B_y|$ diagrams that show the transitions through the regions in the Riemann fans (the paths are indicated by the dashed lines in the first row). The third and fourth rows: $x - y$ diagrams that show the magnetic field configurations on the plane. Only for the case with a guide field, $x - z$ diagram is also depicted. The grey regions indicate the high-entropy regions due to the shock dissipation.

There are two parameters in the symmetric MHD Riemann problems: plasma beta β and the reconnection angle θ . A sophisticated procedure to derive the exact solutions of more general MHD Riemann problems was developed by [Falle et al. \[1998\]](#). We utilize the procedure to derive the exact solutions of our problems. The result is summarized in the phase diagram of [Figure A.3](#), where β and θ are the key parameters. Here the heat conduction is neglected. The θ - β space is divided into two regions: switch-off slow shock regime and pure hydro shock regime. The parameter set of the example introduced in this paper is within the switch-off slow shock region. If we include the heat conduction effect, the pure hydro shock region will become slightly wider.

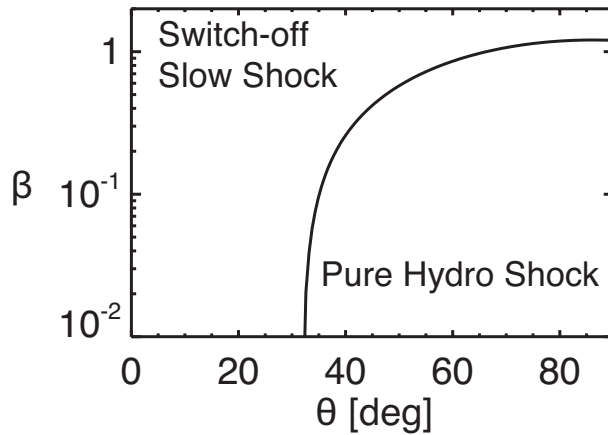


Figure A.3: A phase diagram of the possible solutions of the symmetric Riemann problem in the situation without a guide-field. θ is the reconnection angle and β is the plasma beta. "Switch-off slow shock" regime and "pure hydro shock" regime corresponds to the left and middle panels in [Figure A.2](#), respectively.

[Figure A.4](#) displays the normalized reconnection rate in the θ - β diagram, where the normalized reconnection rate is defined by $v_y B_x / (V_A B_{x0})$. Where v_y is the outflow speed, $V_A = \sqrt{B_x^2 + B_y^2} / \sqrt{\rho}$, and $B_x = B_{x0}$. The maximum reconnection rate observed in solar flares and simulations is of the order of 0.1. To take the reconnection rate similar to 0.1 in our model, we need to choose a reasonable parameter set from this diagram.

If a guide field exists, the rotational discontinuities (RD) will appear in addition to SS and FRW. In this case it is necessary to have either the switch-off SS, switch-off FRW, or RD because of the boundary condition at the contact discontinuity ($B_y = 0$). Among them, only the solution with RD (the right panels of [Figure A.2](#)) meets the requirement that the continuity condition of V_z at the contact discontinuity should be

satisfied [Petschek and Thorne, 1967]. Longcope [2014] claimed that pure hydro shocks can be formed in a reconnected flux tube even when a guide field exists. However, considering the analysis here, pure hydro shocks will not appear when a guide field exists.

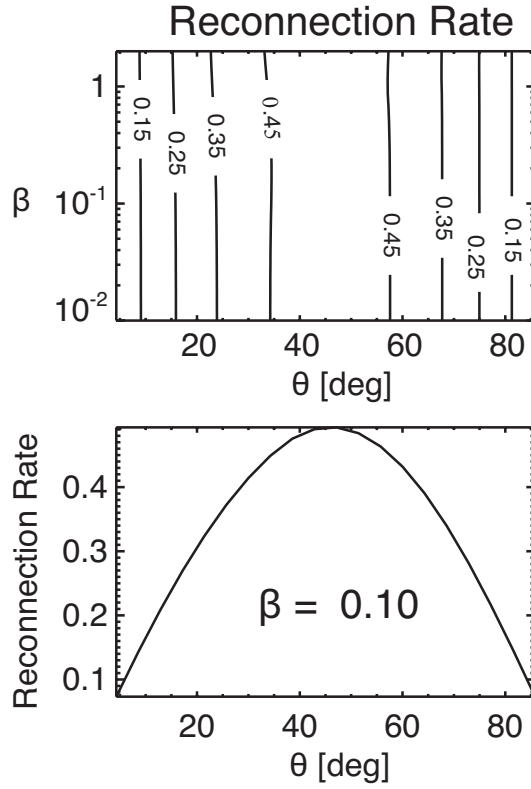


Figure A.4: Top: The normalized reconnection rate in the θ - β plane. Bottom: The normalized reconnection rate for $\beta = 0.1$ as a function of θ .

A.4 Scaling of Fast-mode Mach Number of Reconnection Outflow Jet

The scaling of the fast-mode Mach number of the reconnection outflow jet (M_{FM}) will be briefly discussed. M_{FM} can be written as

$$M_{\text{FM}} = \frac{v_{\text{outflow}}}{c_{f,\text{out}}} \simeq \frac{v_{A,\text{in}}}{c_{s,\text{out}}} \propto \beta^{-1/2} \left(\frac{T_{\text{out}}}{T_{\text{in}}} \right)^{-1/2} \quad (\text{A.30})$$

where v_{outflow} indicates the outflow speed, the quantities in the inflow and outflow regions are denoted with the subscripts “in” and “out,” respectively. Here we assume that the reconnection outflow is high- β and the fast mode wave speed $c_{f,\text{out}}$ and sound speed $c_{s,\text{out}}$ are similar. If we neglect the effect of heat conduction, the temperature increase at the slow shock ΔT can be estimated as

$$\frac{\Delta T}{T_{\text{in}}} \simeq \beta^{-1} \gg 1 \quad (\text{A.31})$$

for low- β plasma, so $T_{\text{out}}/T_{\text{in}} \simeq \beta^{-1}$. However, with the effect of heat conduction,

$$T_{\text{out}} \propto \beta^{-3/7} n_{\text{in}}^{2/7} L^{2/7} \quad (\text{A.32})$$

[see [Shibata and Yokoyama, 2002](#); [Yokoyama et al., 2001a](#)]. The difference in scaling of the temperature leads to the different scalings of the fast-mode Mach number of the outflow jet:

$$M_{\text{FM}} \propto \begin{cases} \text{const.} & (\text{without heat conduction}) \\ \beta^{-2/7} n_{\text{in}}^{-1/7} L^{-1/7} \propto B^{4/7} n_{\text{in}}^{-3/7} L^{-1/7} & (\text{with heat conduction}) \end{cases} \quad (\text{A.33})$$

This means that heat conduction has a significant effect in increase of the fast-mode Mach number. This effect is also pointed out by [Seaton and Forbes \[2009\]](#).

The dependence of M_{FM} on the plasma β is analytically investigated by [Seaton and Forbes \[2009\]](#). They define the normalized thermal conduction coefficient λ^* as the ratio of the energy loss due to heat conduction (F_{cond}) to the energy input by Poynting flux carried at the Alfvén speed V_A into the current sheet ($F_{\text{P,Alfvén}}$): $\lambda^* \equiv F_{\text{cond}}/F_{\text{P,Alfvén}}$. [Yokoyama and Shibata \[1998\]](#); [Yokoyama et al. \[2001a\]](#) found that the assumption that

the heating by Poynting flux carried at the reconnection inflow speed v_{inflow} balances with the conduction cooling provides a good approximation. Considering this, we obtained the following restriction on λ^* :

$$\lambda^* = \frac{F_{\text{cond}}}{F_{\text{P,Alfven}}} = \frac{F_{\text{cond}}}{F_{\text{P,inflow}}} \frac{F_{\text{P,inflow}}}{F_{\text{P,Alfven}}} \simeq O(1) \frac{v_{\text{inflow}}}{V_A} \simeq 0.001 - 0.1, \quad (\text{A.34})$$

where we assume that the nondimensional reconnection rate v_{inflow}/V_A is in the range of approximately 0.001–0.1, considering observations of solar flares [Narukage and Shibata, 2006; Takasao et al., 2012]. Figure A.5 displays the dependence of M_{FM} on the plasma β from Seaton and Forbes [2009]. The data points denoted by triangles and diamonds are for the cases with $\lambda^*=0.003$ and 0.03, respectively, so $0.001 < \lambda^* < 0.1$. The dashed line indicates the slope of the scaling relation (A.33), proportional to $\beta^{-2/7}$. The figure shows that the scaling relation is consistent with their analytical results. Therefore, the simple argument here can explain the dependence of M_{FM} .

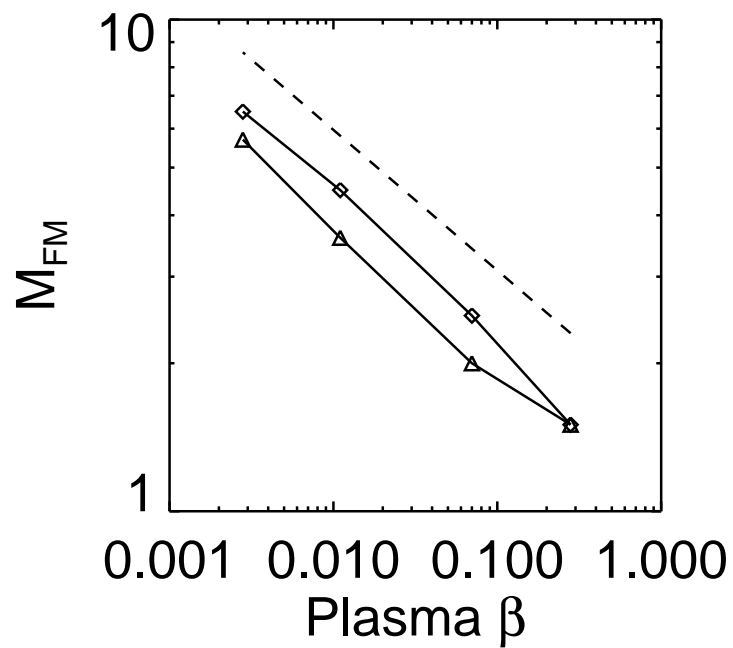


Figure A.5: Dependence of the fast-mode Mach number of the reconnection outflow (M_{FM}) on the plasma β . The data points indicated by diamonds and triangles are from [Seaton and Forbes \[2009\]](#). Diamonds and triangles denote the data points for the normalized conduction coefficient $\lambda^* = 0.03$ and 0.003 , respectively (see the text for the definition of λ^*). The dashed line indicates the slope $\propto \beta^{-2/7}$.

References

- D. J. Acheson. Instability by magnetic buoyancy. *Sol. Phys.*, 62:23–50, May 1979. doi: 10.1007/BF00150129.
- S.-I. Akasofu. An essay on sunspots and solar flares. *Planet. Space Sci.*, 32:1469–1471, November 1984. doi: 10.1016/0032-0633(84)90090-4.
- H. Alfvén and P. Carlqvist. Currents in the Solar Atmosphere and a Theory of Solar Flares. *Sol. Phys.*, 1:220–228, March 1967. doi: 10.1007/BF00150857.
- S. K. Antiochos. The Magnetic Topology of Solar Eruptions. *ApJ*, 502:L181–L184, August 1998. doi: 10.1086/311507.
- S. K. Antiochos, C. R. DeVore, and J. A. Klimchuk. A Model for Solar Coronal Mass Ejections. *ApJ*, 510:485–493, January 1999. doi: 10.1086/306563.
- T. D. Arber, M. Haynes, and J. E. Leake. Emergence of a Flux Tube through a Partially Ionized Solar Atmosphere. *ApJ*, 666:541–546, September 2007. doi: 10.1086/520046.
- V. Archontis, F. Moreno-Insertis, K. Galsgaard, A. Hood, and E. O’Shea. Emergence of magnetic flux from the convection zone into the corona. *A&A*, 426:1047–1063, November 2004. doi: 10.1051/0004-6361:20035934.
- M. J. Aschwanden. Particle acceleration and kinematics in solar flares - A Synthesis of Recent Observations and Theoretical Concepts (Invited Review). *Space Sci. Rev.*, 101:1–227, January 2002. doi: 10.1023/A:1019712124366.
- M. J. Aschwanden and C. J. Schrijver. Coronal Loop Oscillations Observed with Atmospheric Imaging Assembly–Kink Mode with Cross-sectional and Density Oscillations. *ApJ*, 736:102, August 2011. doi: 10.1088/0004-637X/736/2/102.

-
- L. A. Balona, A.-M. Broomhall, A. Kosovichev, V. M. Nakariakov, C. E. Pugh, and T. Van Doorselaere. Oscillations in stellar superflares. *MNRAS*, 450:956–966, June 2015. doi: 10.1093/mnras/stv661.
- M. Bárta, J. Büchner, M. Karlický, and J. Skála. Spontaneous Current-layer Fragmentation and Cascading Reconnection in Solar Flares. I. Model and Analysis. *ApJ*, 737:24, August 2011. doi: 10.1088/0004-637X/737/1/24.
- A. Bhattacharjee, Y.-M. Huang, H. Yang, and B. Rogers. Fast reconnection in high-Lundquist-number plasmas due to the plasmoid Instability. *Physics of Plasmas*, 16(11):112102, November 2009. doi: 10.1063/1.3264103.
- A. Bruzek. On Arch-Filament Systems in Spotgroups. *Sol. Phys.*, 2:451–461, December 1967. doi: 10.1007/BF00146493.
- R. C. Canfield, H. S. Hudson, and D. E. McKenzie. Sigmoidal morphology and eruptive solar activity. *Geophys. Res. Lett.*, 26:627–630, 1999. doi: 10.1029/1999GL900105.
- P. J. Cargill and E. R. Priest. Slow-shock heating and the Kopp-Pneuman model for ‘post’-flare loops. *Sol. Phys.*, 76:357–375, March 1982. doi: 10.1007/BF00170991.
- H. Carmichael. A Process for Flares. *NASA Special Publication*, 50:451, 1964.
- R. C. Carrington. Description of a Singular Appearance seen in the Sun on September 1, 1859. *MNRAS*, 20:13–15, November 1859.
- S. Chandrasekhar. *An introduction to the study of stellar structure*. 1967.
- P. Charbonneau. Solar Dynamo Theory. *ARA&A*, 52:251–290, August 2014. doi: 10.1146/annurev-astro-081913-040012.
- B. Chen, T. S. Bastian, C. Shen, D. E. Gary, S. Krucker, and L. Glesener. Particle acceleration by a solar flare termination shock. *Science*, 350:1238–1242, December 2015. doi: 10.1126/science.aac8467.
- P. F. Chen and K. Shibata. An Emerging Flux Trigger Mechanism for Coronal Mass Ejections. *ApJ*, 545:524–531, December 2000. doi: 10.1086/317803.
- P. F. Chen, C. Fang, Y. H. Tang, and M. D. Ding. Simulation of Magnetic Reconnection with Heat Conduction. *ApJ*, 513:516–523, March 1999. doi: 10.1086/306823.

REFERENCES

- M. C. M. Cheung and M. L. DeRosa. A Method for Data-driven Simulations of Evolving Solar Active Regions. *ApJ*, 757:147, October 2012. doi: 10.1088/0004-637X/757/2/147.
- M. C. M. Cheung and H. Isobe. Flux Emergence (Theory). *Living Reviews in Solar Physics*, 11:3, July 2014. doi: 10.12942/lrsp-2014-3.
- M. C. M. Cheung, M. Rempel, A. M. Title, and M. Schüssler. Simulation of the Formation of a Solar Active Region. *ApJ*, 720:233–244, September 2010. doi: 10.1088/0004-637X/720/1/233.
- D.-Y. Chou and H. Wang. The separation velocity of emerging magnetic flux. *Sol. Phys.*, 110:81–99, March 1987. doi: 10.1007/BF00148204.
- L. L. Cowie and C. F. McKee. The evaporation of spherical clouds in a hot gas. I - Classical and saturated mass loss rates. *ApJ*, 211:135–146, January 1977. doi: 10.1086/154911.
- T. G. Cowling. *Solar Electrodynamics*, page 532. 1953.
- J. L. Culhane, L. K. Harra, A. M. James, K. Al-Janabi, L. J. Bradley, R. A. Chaudry, K. Rees, J. A. Tandy, P. Thomas, M. C. R. Whillock, B. Winter, G. A. Doschek, C. M. Korendyke, C. M. Brown, S. Myers, J. Mariska, J. Seely, J. Lang, B. J. Kent, B. M. Shaughnessy, P. R. Young, G. M. Simnett, C. M. Castelli, S. Mahmoud, H. Mapson-Menard, B. J. Probyn, R. J. Thomas, J. Davila, K. Dere, D. Windt, J. Shea, R. Hagood, R. Moye, H. Hara, T. Watanabe, K. Matsuzaki, T. Kosugi, V. Hansteen, and Ø. Wikstol. The EUV Imaging Spectrometer for Hinode. *Sol. Phys.*, 243:19–61, June 2007. doi: 10.1007/s01007-007-0293-1.
- I. De Moortel and D. J. Pascoe. The Effects of Line-of-sight Integration on Multistrand Coronal Loop Oscillations. *ApJ*, 746:31, February 2012. doi: 10.1088/0004-637X/746/1/31.
- A. Dedner, F. Kemm, D. Kröner, C.-D. Munz, T. Schnitzer, and M. Wesenberg. Hyperbolic Divergence Cleaning for the MHD Equations. *Journal of Computational Physics*, 175:645–673, January 2002. doi: 10.1006/jcph.2001.6961.
- J.-P. Delaboudinière, G. E. Artzner, J. Brunaud, A. H. Gabriel, J. F. Hochedez, F. Millier, X. Y. Song, B. Au, K. P. Dere, R. A. Howard, R. Kreplin, D. J. Michels, J. D. Moses, J. M. Defise, C. Jamar, P. Rochus, J. P. Chauvineau, J. P. Marioge,

-
- R. C. Catura, J. R. Lemen, L. Shing, R. A. Stern, J. B. Gurman, W. M. Neupert, A. Maucherat, F. Clette, P. Cugnon, and E. L. van Dessel. EIT: Extreme-Ultraviolet Imaging Telescope for the SOHO Mission. *Sol. Phys.*, 162:291–312, December 1995. doi: 10.1007/BF00733432.
- J. F. Drake, M. Swisdak, H. Che, and M. A. Shay. Electron acceleration from contracting magnetic islands during reconnection. *Nature*, 443:553–556, October 2006. doi: 10.1038/nature05116.
- J. W. Dungey. The Neutral Point Discharge Theory of Solar Flares. a Reply to Cowling’s Criticism. In B. Lehnert, editor, *Electromagnetic Phenomena in Cosmical Physics*, volume 6 of *IAU Symposium*, page 135, 1958.
- S. A. E. G. Falle, S. S. Komissarov, and P. Joarder. A multidimensional upwind scheme for magnetohydrodynamics. *MNRAS*, 297:265–277, June 1998. doi: 10.1046/j.1365-8711.1998.01506.x.
- Y. Fan. The Emergence of a Twisted Ω -Tube into the Solar Atmosphere. *ApJ*, 554:L111–L114, June 2001. doi: 10.1086/320935.
- Y. Fan. Magnetic Fields in the Solar Convection Zone. *Living Reviews in Solar Physics*, 6:4, December 2009. doi: 10.12942/lrsp-2009-4.
- Y. Fan, E. G. Zweibel, M. G. Linton, and G. H. Fisher. The Rise of Kink-Unstable Magnetic Flux Tubes in the Solar Convection Zone. *ApJ*, 505:L59–L63, September 1998. doi: 10.1086/311597.
- Y. Fan, E. G. Zweibel, M. G. Linton, and G. H. Fisher. The Rise of Kink-unstable Magnetic Flux Tubes and the Origin of δ -Configuration Sunspots. *ApJ*, 521:460–477, August 1999. doi: 10.1086/307533.
- F. Fang and Y. Fan. δ -Sunspot Formation in Simulation of Active-region-scale Flux Emergence. *ApJ*, 806:79, June 2015. doi: 10.1088/0004-637X/806/1/79.
- F. Fang, W. Manchester, IV, W. P. Abbett, and B. van der Holst. Buildup of Magnetic Shear and Free Energy during Flux Emergence and Cancellation. *ApJ*, 754:15, July 2012. doi: 10.1088/0004-637X/754/1/15.
- G. H. Fisher and S. L. Hawley. An equation for the evolution of solar and stellar flare loops. *ApJ*, 357:243–258, July 1990. doi: 10.1086/168911.

- G. H. Fisher, R. C. Canfield, and A. N. McClymont. Flare loop radiative hydrodynamics. V - Response to thick-target heating. VI - Chromospheric evaporation due to heating by nonthermal electrons. VII - Dynamics of the thick-target heated chromosphere. *ApJ*, 289:414–441, February 1985. doi: 10.1086/162901.
- G. H. Fisher, Y. Fan, and R. F. Howard. Comparisons between theory and observation of active region tilts. *ApJ*, 438:463–471, January 1995. doi: 10.1086/175090.
- T. G. Forbes. Fast-shock formation in line-tied magnetic reconnection models of solar flares. *ApJ*, 305:553–563, June 1986. doi: 10.1086/164268.
- T. G. Forbes and L. W. Acton. Reconnection and Field Line Shrinkage in Solar Flares. *ApJ*, 459:330, March 1996. doi: 10.1086/176896.
- T. G. Forbes and J. M. Malherbe. A shock condensation mechanism for loop prominences. *ApJ*, 302:L67–L70, March 1986. doi: 10.1086/184639.
- T. G. Forbes and E. R. Priest. A numerical experiment relevant to line-tied reconnection in two-ribbon flares. *Sol. Phys.*, 84:169–188, April 1983. doi: 10.1007/BF00157455.
- T. G. Forbes and E. R. Priest. Numerical simulation of reconnection in an emerging magnetic flux region. *Sol. Phys.*, 94:315–340, September 1984. doi: 10.1007/BF00151321.
- T. G. Forbes, J. M. Malherbe, and E. R. Priest. The formation flare loops by magnetic reconnection and chromospheric ablation. *Sol. Phys.*, 120:285–307, September 1989. doi: 10.1007/BF00159881.
- R. G. Giovanelli. A Theory of Chromospheric Flares. *Nature*, 158:81–82, July 1946. doi: 10.1038/158081a0.
- M. Güdel. X-ray astronomy of stellar coronae. *A&A Rev.*, 12:71–237, September 2004. doi: 10.1007/s00159-004-0023-2.
- S. E. Guidoni, D. E. McKenzie, D. W. Longcope, J. E. Plowman, and K. Yoshimura. Temperature and Electron Density Diagnostics of a Candle-flame-shaped Flare. *ApJ*, 800:54, February 2015. doi: 10.1088/0004-637X/800/1/54.
- M. Hagino and T. Sakurai. Latitude Variation of Helicity in Solar Active Regions. *PASJ*, 56:831–843, October 2004. doi: 10.1093/pasj/56.5.831.

REFERENCES

- G. E. Hale. On the Probable Existence of a Magnetic Field in Sun-Spots. *ApJ*, 28:315, November 1908. doi: 10.1086/141602.
- G. E. Hale and S. B. Nicholson. The Law of Sun-Spot Polarity. *ApJ*, 62:270, November 1925. doi: 10.1086/142933.
- G. E. Hale, F. Ellerman, S. B. Nicholson, and A. H. Joy. The Magnetic Polarity of Sun-Spots. *ApJ*, 49:153, April 1919. doi: 10.1086/142452.
- H. Hara, T. Watanabe, L. K. Harra, J. L. Culhane, and P. R. Young. Plasma Motions and Heating by Magnetic Reconnection in a 2007 May 19 Flare. *ApJ*, 741:107, November 2011. doi: 10.1088/0004-637X/741/2/107.
- M. R. Hayashi, K. Shibata, and R. Matsumoto. X-Ray Flares and Mass Outflows Driven by Magnetic Interaction between a Protostar and Its Surrounding Disk. *ApJ*, 468:L37, September 1996. doi: 10.1086/310222.
- T. Hirayama. Theoretical Model of Flares and Prominences. I: Evaporating Flare Model. *Sol. Phys.*, 34:323–338, February 1974. doi: 10.1007/BF00153671.
- S. Hirose, Y. Uchida, S. Uemura, T. Yamaguchi, and S. B. Cable. A Quadruple Magnetic Source Model for Arcade Flares and X-Ray Arcade Formations outside Active Regions. II. Dark Filament Eruption and the Associated Arcade Flare. *ApJ*, 551:586–596, April 2001. doi: 10.1086/320084.
- R. Hodgson. On a curious Appearance seen in the Sun. *MNRAS*, 20:15–16, November 1859.
- Z. A. Holder, R. C. Canfield, R. A. McMullen, D. Nandy, R. F. Howard, and A. A. Pevtsov. On the Tilt and Twist of Solar Active Regions. *ApJ*, 611:1149–1155, August 2004. doi: 10.1086/422247.
- K. Hori, T. Yokoyama, T. Kosugi, and K. Shibata. Pseudo-Two-dimensional Hydrodynamic Modeling of Solar Flare Loops. *ApJ*, 489:426–441, November 1997.
- K. Hori, T. Yokoyama, T. Kosugi, and K. Shibata. Single and Multiple Solar Flare Loops: Hydrodynamics and Ca XIX Resonance Line Emission. *ApJ*, 500:492–506, June 1998. doi: 10.1086/305725.
- F. Hoyle. *Some recent researches in solar physics*. 1949.

- S. Imada, I. Murakami, T. Watanabe, H. Hara, and T. Shimizu. Magnetic Reconnection in Non-equilibrium Ionization Plasma. *ApJ*, 742:70, December 2011. doi: 10.1088/0004-637X/742/2/70.
- S. Imada, K. Aoki, H. Hara, T. Watanabe, L. K. Harra, and T. Shimizu. Evidence for Hot Fast Flow above a Solar Flare Arcade. *ApJ*, 776:L11, October 2013. doi: 10.1088/2041-8205/776/1/L11.
- A. R. Inglis, V. M. Nakariakov, and V. F. Melnikov. Multi-wavelength spatially resolved analysis of quasi-periodic pulsations in a solar flare. *A&A*, 487:1147–1153, September 2008. doi: 10.1051/0004-6361:20079323.
- D. E. Innes, D. E. McKenzie, and T. Wang. SUMER spectral observations of post-flare supra-arcade inflows. *Sol. Phys.*, 217:247–265, November 2003.
- T. T. Ishii, H. Kurokawa, and T. T. Takeuchi. Emergence of a Twisted Magnetic Flux Bundle as a Source of Strong Flare Activity. *ApJ*, 499:898–904, May 1998.
- H. Isobe, H. Takasaki, and K. Shibata. Measurement of the Energy Release Rate and the Reconnection Rate in Solar Flares. *ApJ*, 632:1184–1195, October 2005. doi: 10.1086/444490.
- H. Isobe, T. Miyagoshi, K. Shibata, and T. Yokoyama. Three-Dimensional Simulation of Solar Emerging Flux Using the Earth Simulator I. Magnetic Rayleigh-Taylor Instability at the Top of the Emerging Flux as the Origin of Filamentary Structure. *PASJ*, 58:423–438, April 2006.
- M. Kaisig, T. Tajima, K. Shibata, S. Nozawa, and R. Matsumoto. Nonlinear excitation of magnetic undular instability by convective motion. *ApJ*, 358:698–709, August 1990. doi: 10.1086/169024.
- S. R. Kane. Impulsive /flash/ phase of solar flares - Hard X-ray, microwave, EUV and optical observations. In G. A. Newkirk, editor, *Coronal Disturbances*, volume 57 of *IAU Symposium*, pages 105–141, 1974.
- I. Kawaguchi and R. Kitai. The velocity field associated with the birth of sunspots. *Sol. Phys.*, 46:125–135, January 1976. doi: 10.1007/BF00157559.
- H. Kigure, K. Takahashi, K. Shibata, T. Yokoyama, and S. Nozawa. Generation of Alfvén Waves by Magnetic Reconnection. *PASJ*, 62:993–, August 2010.

REFERENCES

- B. Kliem, M. Karlický, and A. O. Benz. Solar flare radio pulsations as a signature of dynamic magnetic reconnection. *A&A*, 360:715–728, August 2000.
- R. A. Kopp and G. W. Pneuman. Magnetic reconnection in the corona and the loop prominence phenomenon. *Sol. Phys.*, 50:85–98, October 1976. doi: 10.1007/BF00206193.
- K. Koyama, K. Hamaguchi, S. Ueno, N. Kobayashi, and E. D. Feigelson. Discovery of Hard X-Rays from a Cluster of Protostars. *PASJ*, 48:L87–L92, October 1996. doi: 10.1093/pasj/48.5.L87.
- S. Krucker, H. S. Hudson, L. Glesener, S. M. White, S. Masuda, J.-P. Wuelser, and R. P. Lin. Measurements of the Coronal Acceleration Region of a Solar Flare. *ApJ*, 714:1108–1119, May 2010. doi: 10.1088/0004-637X/714/2/1108.
- M. Kruskal and M. Schwarzschild. Some Instabilities of a Completely Ionized Plasma. *Proceedings of the Royal Society of London Series A*, 223:348–360, May 1954. doi: 10.1098/rspa.1954.0120.
- M. D. Kruskal, J. L. Johnson, M. B. Gottlieb, and L. M. Goldman. Hydromagnetic Instability in a Stellarator. *Physics of Fluids*, 1:421–429, September 1958. doi: 10.1063/1.1724359.
- P. Kumar and K.-S. Cho. Simultaneous EUV and radio observations of bidirectional plasmoids ejection during magnetic reconnection. *A&A*, 557:A115, September 2013. doi: 10.1051/0004-6361/201220999.
- H. Kurokawa. High-resolution observations of H-alpha flare regions. *Space Sci. Rev.*, 51:49–84, October 1989. doi: 10.1007/BF00226268.
- H. Kurokawa, T. Wang, and T. T. Ishii. Emergence and Drastic Breakdown of a Twisted Flux Rope to Trigger Strong Solar Flares in NOAA Active Region 9026. *ApJ*, 572:598–608, June 2002. doi: 10.1086/340305.
- J. E. Leake and T. D. Arber. The emergence of magnetic flux through a partially ionised solar atmosphere. *A&A*, 450:805–818, May 2006. doi: 10.1051/0004-6361:20054099.
- J. E. Leake and M. G. Linton. Effect of Ion-Neutral Collisions in Simulations of Emerging Active Regions. *ApJ*, 764:54, February 2013. doi: 10.1088/0004-637X/764/1/54.
- K. D. Leka, R. C. Canfield, A. N. McClymont, and L. van Driel-Gesztelyi. Evidence for Current-carrying Emerging Flux. *ApJ*, 462:547, May 1996. doi: 10.1086/177171.

REFERENCES

- J. R. Lemen, A. M. Title, D. J. Akin, P. F. Boerner, C. Chou, J. F. Drake, D. W. Duncan, C. G. Edwards, F. M. Friedlaender, G. F. Heyman, N. E. Hurlburt, N. L. Katz, G. D. Kushner, M. Levay, R. W. Lindgren, D. P. Mathur, E. L. McFeaters, S. Mitchell, R. A. Rehse, C. J. Schrijver, L. A. Springer, R. A. Stern, T. D. Tarbell, J.-P. Wuelser, C. J. Wolfson, C. Yanari, J. A. Bookbinder, P. N. Cheimets, D. Caldwell, E. E. Deluca, R. Gates, L. Golub, S. Park, W. A. Podgorski, R. I. Bush, P. H. Scherrer, M. A. Gummin, P. Smith, G. Auken, P. Jerram, P. Pool, R. Souffi, D. L. Windt, S. Beardsley, M. Clapp, J. Lang, and N. Waltham. The Atmospheric Imaging Assembly (AIA) on the Solar Dynamics Observatory (SDO). *Sol. Phys.*, 275:17–40, January 2012. doi: 10.1007/s11207-011-9776-8.
- J. Lin, Y.-K. Ko, L. Sui, J. C. Raymond, G. A. Stenborg, Y. Jiang, S. Zhao, and S. Mancuso. Direct Observations of the Magnetic Reconnection Site of an Eruption on 2003 November 18. *ApJ*, 622:1251–1264, April 2005. doi: 10.1086/428110.
- M. G. Linton, D. W. Longcope, and G. H. Fisher. The Helical Kink Instability of Isolated, Twisted Magnetic Flux Tubes. *ApJ*, 469:954, October 1996. doi: 10.1086/177842.
- M. G. Linton, G. H. Fisher, R. B. Dahlburg, and Y. Fan. Relationship of the Multimode Kink Instability to δ -Spot Formation. *ApJ*, 522:1190–1205, September 1999. doi: 10.1086/307678.
- W. Liu and L. Ofman. Advances in Observing Various Coronal EUV Waves in the SDO Era and Their Seismological Applications (Invited Review). *Sol. Phys.*, 289: 3233–3277, September 2014. doi: 10.1007/s11207-014-0528-4.
- W. Liu, A. M. Title, J. Zhao, L. Ofman, C. J. Schrijver, M. J. Aschwanden, B. De Pontieu, and T. D. Tarbell. Direct Imaging of Quasi-periodic Fast Propagating Waves of $\sim 2000 \text{ km s}^{-1}$ in the Low Solar Corona by the Solar Dynamics Observatory Atmospheric Imaging Assembly. *ApJ*, 736:L13, July 2011. doi: 10.1088/2041-8205/736/1/L13.
- W. Liu, L. Ofman, N. V. Nitta, M. J. Aschwanden, C. J. Schrijver, A. M. Title, and T. D. Tarbell. Quasi-periodic Fast-mode Wave Trains within a Global EUV Wave and Sequential Transverse Oscillations Detected by SDO/AIA. *ApJ*, 753:52, July 2012. doi: 10.1088/0004-637X/753/1/52.
- W. Liu, Q. Chen, and V. Petrosian. Plasmoid Ejections and Loop Contractions in an Eruptive M7.7 Solar Flare: Evidence of Particle Acceleration and Heating in Mag-

- netic Reconnection Outflows. *ApJ*, 767:168, April 2013. doi: 10.1088/0004-637X/767/2/168.
- D. W. Longcope. A Simple Model of Chromospheric Evaporation and Condensation Driven Conductively in a Solar Flare. *ApJ*, 795:10, November 2014. doi: 10.1088/0004-637X/795/1/10.
- D. W. Longcope and S. J. Bradshaw. Slow Shocks and Conduction Fronts from Petschek Reconnection of Skewed Magnetic Fields: Two-fluid Effects. *ApJ*, 718:1491–1508, August 2010. doi: 10.1088/0004-637X/718/2/1491.
- D. W. Longcope, G. H. Fisher, and A. A. Pevtsov. Flux-Tube Twist Resulting from Helical Turbulence: The Σ -Effect. *ApJ*, 507:417–432, November 1998. doi: 10.1086/306312.
- D. W. Longcope, S. E. Guidoni, and M. G. Linton. Gas-dynamic Shock Heating of Post-flare Loops Due to Retraction Following Localized, Impulsive Reconnection. *ApJ*, 690:L18–L22, January 2009. doi: 10.1088/0004-637X/690/1/L18.
- M. C. López Fuentes, P. Démoulin, C. H. Mandrini, A. A. Pevtsov, and L. van Driel-Gesztelyi. Magnetic twist and writhe of active regions. On the origin of deformed flux tubes. *A&A*, 397:305–318, January 2003. doi: 10.1051/0004-6361:20021487.
- N. F. Loureiro, A. A. Schekochihin, and S. C. Cowley. Instability of current sheets and formation of plasmoid chains. *Physics of Plasmas*, 14(10):100703, October 2007. doi: 10.1063/1.2783986.
- S. Lundquist. On the Stability of Magneto-Hydrostatic Fields. *Physical Review*, 83:307–311, July 1951. doi: 10.1103/PhysRev.83.307.
- M. Machida and R. Matsumoto. Global Three-dimensional Magnetohydrodynamic Simulations of Black Hole Accretion Disks: X-Ray Flares in the Plunging Region. *ApJ*, 585:429–442, March 2003. doi: 10.1086/346070.
- D. H. Mackay, L. M. Green, and A. van Ballegoijen. Modeling the Dispersal of an Active Region: Quantifying Energy Input into the Corona. *ApJ*, 729:97, March 2011. doi: 10.1088/0004-637X/729/2/97.
- T. Magara and D. W. Longcope. Sigmoid Structure of an Emerging Flux Tube. *ApJ*, 559:L55–L59, September 2001. doi: 10.1086/323635.

REFERENCES

- T. Magara and D. W. Longcope. Injection of Magnetic Energy and Magnetic Helicity into the Solar Atmosphere by an Emerging Magnetic Flux Tube. *ApJ*, 586:630–649, March 2003. doi: 10.1086/367611.
- W. Manchester, IV. The Role of Nonlinear Alfvén Waves in Shear Formation during Solar Magnetic Flux Emergence. *ApJ*, 547:503–519, January 2001. doi: 10.1086/318342.
- W. Manchester, IV, T. Gombosi, D. DeZeeuw, and Y. Fan. Eruption of a Buoyantly Emerging Magnetic Flux Rope. *ApJ*, 610:588–596, July 2004. doi: 10.1086/421516.
- W. M. Manheimer and H. H. Klein. Model for the production and transport of energetic particles in a laser produced plasma. *Physics of Fluids*, 18:1299–1307, October 1975. doi: 10.1063/1.861004.
- J. T. Mariska, A. G. Emslie, and P. Li. Numerical simulations of impulsively heated solar flares. *ApJ*, 341:1067–1074, June 1989. doi: 10.1086/167564.
- Y. Masada, S. Nagataki, K. Shibata, and T. Terasawa. Solar-Type Magnetic Reconnection Model for Magnetar Giant Flares. *PASJ*, 62:1093–, August 2010. doi: 10.1093/pasj/62.4.1093.
- S. Masuda, T. Kosugi, H. Hara, S. Tsuneta, and Y. Ogawara. A loop-top hard X-ray source in a compact solar flare as evidence for magnetic reconnection. *Nature*, 371:495–497, October 1994. doi: 10.1038/371495a0.
- S. Masuda, T. Kosugi, H. Hara, T. Sakao, K. Shibata, and S. Tsuneta. Hard X-Ray Sources and the Primary Energy-Release Site in Solar Flares. *PASJ*, 47:677–689, October 1995.
- M. Mathioudakis, J. H. Seiradakis, D. R. Williams, S. Avgoloupis, D. S. Bloomfield, and R. T. J. McAteer. White-light oscillations during a flare on II Peg. *A&A*, 403:1101–1104, June 2003. doi: 10.1051/0004-6361:20030394.
- R. Matsumoto and K. Shibata. Three-dimensional MHD simulation of the Parker instability in galactic gas disks and the solar atmosphere. *PASJ*, 44:167–175, June 1992.
- R. Matsumoto, T. Tajima, K. Shibata, and M. Kaisig. Three-dimensional magneto-hydrodynamics of the emerging magnetic flux in the solar atmosphere. *ApJ*, 414:357–371, September 1993. doi: 10.1086/173082.

-
- R. Matsumoto, T. Tajima, W. Chou, A. Okubo, and K. Shibata. Formation of a Kinked Alignment of Solar Active Regions. *ApJ*, 493:L43–L46, January 1998. doi: 10.1086/311116.
- E. W. Maunder. The sun and sun-spots, 1820-1920. *MNRAS*, 82:534–543, June 1922.
- D. E. McKenzie. Turbulent Dynamics in Solar Flare Sheet Structures Measured with Local Correlation Tracking. *ApJ*, 766:39, March 2013. doi: 10.1088/0004-637X/766/1/39.
- J. A. McLaughlin, I. De Moortel, A. W. Hood, and C. S. Brady. Nonlinear fast magnetoacoustic wave propagation in the neighbourhood of a 2D magnetic X-point: oscillatory reconnection. *A&A*, 493:227–240, January 2009. doi: 10.1051/0004-6361:200810465.
- U. Mitra-Kraev, L. K. Harra, D. R. Williams, and E. Kraev. The first observed stellar X-ray flare oscillation: Constraints on the flare loop length and the magnetic field. *A&A*, 436:1041–1047, June 2005. doi: 10.1051/0004-6361:20052834.
- T. Miyagoshi and T. Yokoyama. Magnetohydrodynamic Simulation of Solar Coronal Chromospheric Evaporation Jets Caused by Magnetic Reconnection Associated with Magnetic Flux Emergence. *ApJ*, 614:1042–1053, October 2004. doi: 10.1086/423731.
- T. Miyoshi and K. Kusano. A multi-state HLL approximate Riemann solver for ideal magnetohydrodynamics. *Journal of Computational Physics*, 208:315–344, September 2005. doi: 10.1016/j.jcp.2005.02.017.
- H. K. Moffatt and R. L. Ricca. Helicity and the Calugareanu Invariant. *Proceedings of the Royal Society of London Series A*, 439:411–429, November 1992. doi: 10.1098/rspa.1992.0159.
- R. L. Moore, A. C. Sterling, H. S. Hudson, and J. R. Lemen. Onset of the Magnetic Explosion in Solar Flares and Coronal Mass Ejections. *ApJ*, 552:833–848, May 2001. doi: 10.1086/320559.
- M. J. Murray, L. van Driel-Gesztelyi, and D. Baker. Simulations of emerging flux in a coronal hole: oscillatory reconnection. *A&A*, 494:329–337, January 2009. doi: 10.1051/0004-6361:200810406.
- F. Nagai. A model of hot loops associated with solar flares. I - Gasdynamics in the loops. *Sol. Phys.*, 68:351–379, December 1980. doi: 10.1007/BF00156874.

-
- Y. Nakagawa and R. S. Steinolfson. Dynamical response of the solar corona. I - Basic formulations. II - Numerical simulations near the sun. *ApJ*, 207:296–307, July 1976. doi: 10.1086/154493.
- H. Nakajima, T. Kosugi, K. Kai, and S. Enome. Successive electron and ion accelerations in impulsive solar flares on 7 and 21 June 1980. *Nature*, 305:292–294, September 1983. doi: 10.1038/305292a0.
- V. M. Nakariakov and V. F. Melnikov. Quasi-Periodic Pulsations in Solar Flares. *Space Sci. Rev.*, 149:119–151, December 2009. doi: 10.1007/s11214-009-9536-3.
- V. M. Nakariakov, D. Tsiklauri, A. Kelly, T. D. Arber, and M. J. Aschwanden. Acoustic oscillations in solar and stellar flaring loops. *A&A*, 414:L25–L28, January 2004. doi: 10.1051/0004-6361:20031738.
- D. Nandy. Magnetic helicity and flux tube dynamics in the solar convection zone: Comparisons between observation and theory. *Journal of Geophysical Research (Space Physics)*, 111:A12S01, December 2006. doi: 10.1029/2006JA011882.
- N. Narukage and K. Shibata. Statistical Analysis of Reconnection Inflows in Solar Flares Observed with SOHO EIT. *ApJ*, 637:1122–1134, February 2006. doi: 10.1086/498492.
- N. J. Nelson, B. P. Brown, A. Sacha Brun, M. S. Miesch, and J. Toomre. Buoyant Magnetic Loops Generated by Global Convective Dynamo Action. *Sol. Phys.*, 289: 441–458, February 2014. doi: 10.1007/s11207-012-0221-4.
- W. A. Newcomb. Convective Instability Induced by Gravity in a Plasma with a Frozen-In Magnetic Field. *Physics of Fluids*, 4:391–396, April 1961. doi: 10.1063/1.1706342.
- K. Nishida, N. Nishizuka, and K. Shibata. The Role of a Flux Rope Ejection in a Three-dimensional Magnetohydrodynamic Simulation of a Solar Flare. *ApJ*, 775: L39, October 2013. doi: 10.1088/2041-8205/775/2/L39.
- N. Nishizuka and K. Shibata. Fermi Acceleration in Plasmoids Interacting with Fast Shocks of Reconnection via Fractal Reconnection. *Physical Review Letters*, 110(5): 051101, February 2013. doi: 10.1103/PhysRevLett.110.051101.
- N. Nishizuka, M. Karlický, M. Janvier, and M. Bárta. Particle Acceleration in Plasmoid Ejections Derived from Radio Drifting Pulsating Structures. *ApJ*, 799:126, February 2015. doi: 10.1088/0004-637X/799/2/126.

REFERENCES

- G. Nisticò, D. J. Pascoe, and V. M. Nakariakov. Observation of a high-quality quasi-periodic rapidly propagating wave train using SDO/AIA. *A&A*, 569:A12, September 2014. doi: 10.1051/0004-6361/201423763.
- S. Nozawa, K. Shibata, R. Matsumoto, A. C. Sterling, T. Tajima, Y. Uchida, A. Ferrari, and R. Rosner. Emergence of magnetic flux from the convection zone into the solar atmosphere. I - Linear and nonlinear adiabatic evolution of the convective-Parker instability. *ApJS*, 78:267–282, January 1992. doi: 10.1086/191627.
- L. Ofman and T. Wang. Hot Coronal Loop Oscillations Observed by SUMER: Slow Magnetosonic Wave Damping by Thermal Conduction. *ApJ*, 580:L85–L88, November 2002. doi: 10.1086/345548.
- L. Ofman, W. Liu, A. Title, and M. Aschwanden. Modeling Super-fast Magnetosonic Waves Observed by SDO in Active Region Funnels. *ApJ*, 740:L33, October 2011. doi: 10.1088/2041-8205/740/2/L33.
- M. Ohyama and K. Shibata. Preflare Heating and Mass Motion in a Solar Flare Associated with Hot Plasma Ejection: 1993 November 11 C9.7 Flare. *PASJ*, 49:249–261, April 1997. doi: 10.1093/pasj/49.2.249.
- M. Oka, S. Krucker, H. S. Hudson, and P. Saint-Hilaire. Electron Energy Partition in the Above-the-looptop Solar Hard X-Ray Sources. *ApJ*, 799:129, February 2015. doi: 10.1088/0004-637X/799/2/129.
- K. Otsuji, T. Sakurai, and K. Kuzanyan. A statistical analysis of current helicity and twist in solar active regions over the phases of the solar cycle using the spectropolarimeter data of Hinode. *PASJ*, 67:6, February 2015. doi: 10.1093/pasj/psu130.
- E. N. Parker. The Formation of Sunspots from the Solar Toroidal Field. *ApJ*, 121:491, March 1955. doi: 10.1086/146010.
- E. N. Parker. Sweet’s Mechanism for Merging Magnetic Fields in Conducting Fluids. *J. Geophys. Res.*, 62:509–520, December 1957. doi: 10.1029/JZ062i004p00509.
- E. N. Parker. *Interplanetary dynamical processes*. 1963.
- E. N. Parker. The Dynamical State of the Interstellar Gas and Field. *ApJ*, 145:811, September 1966. doi: 10.1086/148828.

REFERENCES

- E. N. Parker. The Dynamical Properties of Twisted Ropes of Magnetic Field and the Vigor of New Active Regions on the Sun. *ApJ*, 191:245–254, July 1974. doi: 10.1086/152961.
- E. N. Parker. The generation of magnetic fields in astrophysical bodies. X - Magnetic buoyancy and the solar dynamo. *ApJ*, 198:205–209, May 1975. doi: 10.1086/153593.
- E. N. Parker. *Cosmical magnetic fields: Their origin and their activity*. 1979.
- D. J. Pascoe, V. M. Nakariakov, and E. G. Kupriyanova. Fast magnetoacoustic wave trains in magnetic funnels of the solar corona. *A&A*, 560:A97, December 2013. doi: 10.1051/0004-6361/201322678.
- G. Peres and F. Reale. Detectability of chromospheric evaporation fronts in solar flares. *A&A*, 275:L13, August 1993.
- G. Peres, F. Reale, S. Serio, and R. Pallavicini. Hydrodynamic flare modeling - Comparison of numerical calculations with SMM observations of the 1980 November 12 17:00 UT flare. *ApJ*, 312:895–908, January 1987. doi: 10.1086/164936.
- W. D. Pesnell, B. J. Thompson, and P. C. Chamberlin. The Solar Dynamics Observatory (SDO). *Sol. Phys.*, 275:3–15, January 2012. doi: 10.1007/s11207-011-9841-3.
- G. J. D. Petrie. The Abrupt Changes in the Photospheric Magnetic and Lorentz Force Vectors during Six Major Neutral-line Flares. *ApJ*, 759:50, November 2012. doi: 10.1088/0004-637X/759/1/50.
- H. E. Petschek. Magnetic Field Annihilation. *NASA Special Publication*, 50:425, 1964.
- H. E. Petschek and R. M. Thorne. The Existence of Intermediate Waves in Neutral Sheets. *ApJ*, 147:1157, March 1967. doi: 10.1086/149105.
- A. A. Pevtsov, R. C. Canfield, and T. R. Metcalf. Latitudinal variation of helicity of photospheric magnetic fields. *ApJ*, 440:L109–L112, February 1995. doi: 10.1086/187773.
- A. A. Pevtsov, R. C. Canfield, and S. M. Latushko. Hemispheric Helicity Trend for Solar Cycle 23. *ApJ*, 549:L261–L263, March 2001. doi: 10.1086/319179.
- E. R. Priest. *Solar magneto-hydrodynamics*. 1982.
- E. R. Priest and T. G. Forbes. The magnetic nature of solar flares. *A&A Rev.*, 10: 313–377, 2002. doi: 10.1007/s001590100013.

- K. K. Reeves and H. P. Warren. Modeling the Cooling of Postflare Loops. *ApJ*, 578: 590–597, October 2002. doi: 10.1086/342310.
- M. Rempel and M. C. M. Cheung. Numerical Simulations of Active Region Scale Flux Emergence: From Spot Formation to Decay. *ApJ*, 785:90, April 2014. doi: 10.1088/0004-637X/785/2/90.
- M. Rempel, M. Schüssler, and M. Knölker. Radiative Magnetohydrodynamic Simulation of Sunspot Structure. *ApJ*, 691:640–649, January 2009. doi: 10.1088/0004-637X/691/1/640.
- D. M. Rust and A. Kumar. Evidence for Helically Kinked Magnetic Flux Ropes in Solar Eruptions. *ApJ*, 464:L199, June 1996. doi: 10.1086/310118.
- I. Sammis, F. Tang, and H. Zirin. The Dependence of Large Flare Occurrence on the Magnetic Structure of Sunspots. *ApJ*, 540:583–587, September 2000. doi: 10.1086/309303.
- J. Schou, P. H. Scherrer, R. I. Bush, R. Wachter, S. Couvidat, M. C. Rabello-Soares, R. S. Bogart, J. T. Hoeksema, Y. Liu, T. L. Duvall, D. J. Akin, B. A. Allard, J. W. Miles, R. Rairden, R. A. Shine, T. D. Tarbell, A. M. Title, C. J. Wolfson, D. F. Elmore, A. A. Norton, and S. Tomczyk. Design and Ground Calibration of the Helioseismic and Magnetic Imager (HMI) Instrument on the Solar Dynamics Observatory (SDO). *Sol. Phys.*, 275:229–259, January 2012. doi: 10.1007/s11207-011-9842-2.
- D. B. Seaton and T. G. Forbes. An Analytical Model for Reconnection Outflow Jets Including Thermal Conduction. *ApJ*, 701:348–359, August 2009. doi: 10.1088/0004-637X/701/1/348.
- Y. Shen and Y. Liu. Observational Study of the Quasi-periodic Fast-propagating Magnetosonic Waves and the Associated Flare on 2011 May 30. *ApJ*, 753:53, July 2012. doi: 10.1088/0004-637X/753/1/53.
- K. Shibata. Evidence of Magnetic Reconnection in Solar Flares and a Unified Model of Flares. *Ap&SS*, 264:129–144, 1999.
- K. Shibata and T. Magara. Solar Flares: Magnetohydrodynamic Processes. *Living Reviews in Solar Physics*, 8:6, December 2011.
- K. Shibata and S. Tanuma. Plasmoid-induced-reconnection and fractal reconnection. *Earth, Planets, and Space*, 53:473–482, June 2001.

-
- K. Shibata and T. Yokoyama. A Hertzsprung-Russell-like Diagram for Solar/Stellar Flares and Corona: Emission Measure versus Temperature Diagram. *ApJ*, 577:422–432, September 2002. doi: 10.1086/342141.
- K. Shibata, T. Tajima, R. Matsumoto, T. Horiuchi, T. Hanawa, R. Rosner, and Y. Uchida. Nonlinear Parker instability of isolated magnetic flux in a plasma. *ApJ*, 338:471–492, March 1989a. doi: 10.1086/167212.
- K. Shibata, T. Tajima, R. S. Steinolfson, and R. Matsumoto. Two-dimensional magnetohydrodynamic model of emerging magnetic flux in the solar atmosphere. *ApJ*, 345:584–596, October 1989b. doi: 10.1086/167932.
- K. Shibata, S. Masuda, M. Shimojo, H. Hara, T. Yokoyama, S. Tsuneta, T. Kosugi, and Y. Ogawara. Hot-Plasma Ejections Associated with Compact-Loop Solar Flares. *ApJ*, 451:L83, October 1995. doi: 10.1086/309688.
- T. Shimizu, B. W. Lites, and Y. Bamba. High-speed photospheric material flow observed at the polarity inversion line of a δ -type sunspot producing an X5.4 flare on 2012 March 7. *PASJ*, 66:S14, December 2014. doi: 10.1093/pasj/psu089.
- M. Shimojo, K. Shibata, and K. L. Harvey. Magnetic Field Properties of Solar X-Ray Jets. *Sol. Phys.*, 178:379–392, 1998. doi: 10.1023/A:1005091905214.
- M. Shimojo, N. Narukage, R. Kano, T. Sakao, S. Tsuneta, K. Shibasaki, J. W. Cirtain, L. L. Lundquist, K. K. Reeves, and A. Savcheva. Fine Structures of Solar X-Ray Jets Observed with the X-Ray Telescope aboard Hinode. *PASJ*, 59:745, November 2007. doi: 10.1093/pasj/59.sp3.S745.
- D. Shiota, H. Isobe, P. F. Chen, T. T. Yamamoto, T. Sakajiri, and K. Shibata. Self-Consistent Magnetohydrodynamic Modeling of a Coronal Mass Ejection, Coronal Dimming, and a Giant Cusp-shaped Arcade Formation. *ApJ*, 634:663–678, November 2005. doi: 10.1086/496943.
- B. V. Somov and T. Kosugi. Collisionless Reconnection and High-Energy Particle Acceleration in Solar Flares. *ApJ*, 485:859–868, August 1997.
- L. Spitzer. *Physics of Fully Ionized Gases*. 1962.
- H. C. Spruit and A. A. van Ballegoijen. Stability of toroidal flux tubes in stars. *A&A*, 106:58–66, February 1982.

-
- A. C. Sterling, R. L. Moore, D. A. Falconer, and M. Adams. Small-scale filament eruptions as the driver of X-ray jets in solar coronal holes. *Nature*, 523:437–440, July 2015. doi: 10.1038/nature14556.
- P. A. Sturrock. Model of the High-Energy Phase of Solar Flares. *Nature*, 211:695–697, August 1966. doi: 10.1038/211695a0.
- Z. Svestka. *Solar Flares*. 1976.
- P. A. Sweet. The Neutral Point Theory of Solar Flares. In B. Lehnert, editor, *Electromagnetic Phenomena in Cosmical Physics*, volume 6 of *IAU Symposium*, page 123, 1958.
- H. Takasaki, A. Asai, J. Kiyohara, M. Shimojo, T. Terasawa, Y. Takei, and K. Shibata. A Quantitative Study of the Homologous Flares on 2000 November 24. *ApJ*, 613: 592–599, September 2004. doi: 10.1086/422862.
- S. Takasao, A. Asai, H. Isobe, and K. Shibata. Simultaneous Observation of Reconnection Inflow and Outflow Associated with the 2010 August 18 Solar Flare. *ApJ*, 745: L6, January 2012. doi: 10.1088/2041-8205/745/1/L6.
- S. Takasao, H. Isobe, and K. Shibata. Numerical Simulations of Solar Chromospheric Jets Associated with Emerging Flux. *PASJ*, 65:62, June 2013. doi: 10.1093/pasj/65.3.62.
- S. Takasao, T. Matsumoto, N. Nakamura, and K. Shibata. Magnetohydrodynamic Shocks in and above Post-flare Loops: Two-dimensional Simulation and a Simplified Model. *ApJ*, 805:135, June 2015. doi: 10.1088/0004-637X/805/2/135.
- K. Takizawa and R. Kitai. Evolution and Flare Activity of δ -Sunspots in Cycle 23. *Sol. Phys.*, 290:2093–2116, July 2015. doi: 10.1007/s11207-015-0720-1.
- K. Tanaka. Studies on a very flare-active delta group - Peculiar delta SPOT evolution and inferred subsurface magnetic rope structure. *Sol. Phys.*, 136:133–149, November 1991. doi: 10.1007/BF00151700.
- S. Tanuma and K. Shibata. Internal Shocks in the Magnetic Reconnection Jet in Solar Flares: Multiple Fast Shocks Created by the Secondary Tearing Instability. *ApJ*, 628:L77–L80, July 2005. doi: 10.1086/432418.
- L. Tian and Y. Liu. Tilt and α_{best} of major flare-producing active regions. *A&A*, 407:L13–L16, August 2003. doi: 10.1051/0004-6361:20030977.

REFERENCES

- L. Tian, D. Alexander, Y. Liu, and J. Yang. Magnetic Twist and Writhe of δ Active Regions. *Sol. Phys.*, 229:63–77, June 2005. doi: 10.1007/s11207-005-3524-x.
- S. Toriumi, Y. Iida, K. Kusano, Y. Bamba, and S. Imada. Formation of a Flare-Productive Active Region: Observation and Numerical Simulation of NOAA AR 11158. *Sol. Phys.*, 289:3351–3369, September 2014. doi: 10.1007/s11207-014-0502-1.
- Y. Tsuboi, K. Koyama, H. Murakami, M. Hayashi, S. Skinner, and S. Ueno. ASCA Detection of a Superhot 100 Million K X-Ray Flare on the Weak-Lined T Tauri Star V773 Tauri. *ApJ*, 503:894–901, August 1998. doi: 10.1086/306024.
- S. Tsuneta. Structure and Dynamics of Magnetic Reconnection in a Solar Flare. *ApJ*, 456:840, January 1996. doi: 10.1086/176701.
- S. Tsuneta. Moving Plasmoid and Formation of the Neutral Sheet in a Solar Flare. *ApJ*, 483:507, July 1997. doi: 10.1086/304236.
- S. Tsuneta and T. Naito. Fermi Acceleration at the Fast Shock in a Solar Flare and the Impulsive Loop-Top Hard X-Ray Source. *ApJ*, 495:L67–L70, March 1998. doi: 10.1086/311207.
- S. Tsuneta, H. Hara, T. Shimizu, L. W. Acton, K. T. Strong, H. S. Hudson, and Y. Ogawara. Observation of a solar flare at the limb with the YOHKOH Soft X-ray Telescope. *PASJ*, 44:L63–L69, October 1992.
- M. Ugai. Computer studies on development of the fast reconnection mechanism for different resistivity models. *Physics of Fluids B*, 4:2953–2963, September 1992. doi: 10.1063/1.860458.
- T. Van Doorselaere, V. M. Nakariakov, and E. Verwichte. Detection of Waves in the Solar Corona: Kink or Alfvén? *ApJ*, 676:L73–L75, March 2008. doi: 10.1086/587029.
- A. Vögler, S. Shelyag, M. Schüssler, F. Cattaneo, T. Emonet, and T. Linde. Simulations of magneto-convection in the solar photosphere. Equations, methods, and results of the MURaM code. *A&A*, 429:335–351, January 2005. doi: 10.1051/0004-6361:20041507.
- T. J. Wang, S. K. Solanki, W. Curdt, D. E. Innes, I. E. Dammasch, and B. Kliem. Hot coronal loop oscillations observed with SUMER: Examples and statistics. *A&A*, 406:1105–1121, August 2003. doi: 10.1051/0004-6361:20030858.

-
- H. P. Warren. Multithread Hydrodynamic Modeling of a Solar Flare. *ApJ*, 637:522–530, January 2006. doi: 10.1086/497904.
- M. J. Wilson and S. A. E. G. Falle. Steady jets. *MNRAS*, 216:971–985, October 1985. doi: 10.1093/mnras/216.4.971.
- L. Yang, L. Zhang, J. He, H. Peter, C. Tu, L. Wang, S. Zhang, and X. Feng. Numerical Simulation of Fast-mode Magnetosonic Waves Excited by Plasmoid Ejections in the Solar Corona. *ApJ*, 800:111, February 2015. doi: 10.1088/0004-637X/800/2/111.
- A. R. Yeates, D. H. Mackay, and A. A. van Ballegooijen. Modelling the Global Solar Corona: Filament Chirality Observations and Surface Simulations. *Sol. Phys.*, 245: 87–107, September 2007. doi: 10.1007/s11207-007-9013-7.
- T. Yokoyama. Magnetic reconnection model of coronal X-ray jets. In T.-D. Guyenne, editor, *Solar Jets and Coronal Plumes*, volume 421 of *ESA Special Publication*, page 215, 1998.
- T. Yokoyama and K. Shibata. Magnetic Reconnection Coupled with Heat Conduction. *ApJ*, 474:L61–L64, January 1997. doi: 10.1086/310429.
- T. Yokoyama and K. Shibata. A Two-dimensional Magnetohydrodynamic Simulation of Chromospheric Evaporation in a Solar Flare Based on a Magnetic Reconnection Model. *ApJ*, 494:L113–L116, February 1998. doi: 10.1086/311174.
- T. Yokoyama and K. Shibata. Magnetohydrodynamic Simulation of a Solar Flare with Chromospheric Evaporation Effect Based on the Magnetic Reconnection Model. *ApJ*, 549:1160–1174, March 2001. doi: 10.1086/319440.
- T. Yokoyama, K. Akita, T. Morimoto, K. Inoue, and J. Newmark. Clear Evidence of Reconnection Inflow of a Solar Flare. *ApJ*, 546:L69–L72, January 2001a. doi: 10.1086/318053.
- T. Yokoyama, K. Akita, T. Morimoto, K. Inoue, and J. Newmark. Clear Evidence of Reconnection Inflow of a Solar Flare. *ApJ*, 546:L69–L72, January 2001b. doi: 10.1086/318053.
- D. Yuan, Y. Shen, Y. Liu, V. M. Nakariakov, B. Tan, and J. Huang. Distinct propagating fast wave trains associated with flaring energy releases. *A&A*, 554:A144, June 2013. doi: 10.1051/0004-6361/201321435.

REFERENCES

- V. Yurchyshyn, M. Karlický, Q. Hu, and H. Wang. Evidence for Tether-Cutting Reconnection in a Quadrupole Magnetic Configuration in the April 9, 2001, M7.9 Flare. *Sol. Phys.*, 235:147–160, May 2006. doi: 10.1007/s11207-006-0025-5.
- S. Zenitani and T. Miyoshi. Magnetohydrodynamic structure of a plasmoid in fast reconnection in low-beta plasmas. *Physics of Plasmas*, 18(2):022105, February 2011. doi: 10.1063/1.3554655.
- S. Zhongxian and W. Jingxiu. Delta-sunspots and X-class flares. *Sol. Phys.*, 149:105–118, January 1994. doi: 10.1007/BF00645181.
- H. Zirin and M. A. Liggett. Delta spots and great flares. *Sol. Phys.*, 113:267–281, 1987. doi: 10.1007/BF00147707.
- H. Zirin and K. Tanaka. The Flares of August 1972. *Sol. Phys.*, 32:173–207, September 1973. doi: 10.1007/BF00152736.
- C. Zwaan. On the Appearance of Magnetic Flux in the Solar Photosphere. *Sol. Phys.*, 60:213–240, December 1978. doi: 10.1007/BF00156523.
- C. Zwaan. The emergence of magnetic flux. *Sol. Phys.*, 100:397–414, October 1985. doi: 10.1007/BF00158438.